INFORMATION TO USERS

This material was produced from a microfilm copy of the original document. While the most advanced technological means to photograph and reproduce this document have been used, the quality is heavily dependent upon the quality of the original submitted.

The following explanation of techniques is provided to help you understand markings or patterns which may appear on this reproduction.

1. The sign or "target" for pages apparently lacking from the document photographed is "Missing Page(s)". If it was possible to obtain the missing page(s) or section, they are spliced into the film along with adjacent pages. This may have necessitated cutting thru an image and duplicating adjacent pages to insure you complete continuity.

2. When an image on the film is obliterated with a large round black mark, it is an indication that the photographer suspected that the copy may have moved during exposure and thus cause a blurred image. You will find a good image of the page in the adjacent frame.

3. When a map, drawing or chart, etc., was part of the material being photographed the photographer followed a definite method in "sectioning" the material. It is customary to begin photoing at the upper left hand corner of a large sheet and to continue photoing from left to right in equal sections with a small overlap. If necessary, sectioning is continued again — beginning below the first row and continuing on until complete.

4. The majority of users indicate that the textual content is of greatest value, however, a somewhat higher quality reproduction could be made from "photographs" if essential to the understanding of the dissertation. Silver prints of "photographs" may be ordered at additional charge by writing the Order Department, giving the catalog number, title, author and specific pages you wish reproduced.

5. PLEASE NOTE: Some pages may have indistinct print. Filmed as received.

Xerox University Microfilms
300 North Zeeb Road
Ann Arbor, Michigan 48106

73-24,536

CAPUTI, Jr., William James, 1936-
DATA BASED SECOND-ORDER PHASE ERROR ESTIMATION
AND CONTROL IN COHERENT IMAGE FORMING SYSTEMS.

The University of Michigan, Ph.D., 1973
Engineering, electrical

University Microfilms, A XEROX Company, Ann Arbor, Michigan

THIS DISSERTATION HAS BEEN MICROFILMED EXACTLY AS RECEIVED.

DATA BASED SECOND-ORDER PHASE ERROR ESTIMATION AND CONTROL IN COHERENT IMAGE FORMING SYSTEMS

by
William James Caputi, Jr.

A dissertation submitted in partial fulfillment
of the requirements for the degree of
Doctor of Philosophy
(Electrical Engineering)
in The University of Michigan
1972

Doctoral Committee:

Professor Emmett N. Leith, Chairman
Professor Elmer G. Gilbert
Professor Leonard J. Porcello
Professor Thomas B. A. Senior
Mr. Juris Upatnieks

ACKNOWLEDGMENT

The author would like to acknowledge all the individuals who contributed to the work performed on the application of the non-coherent autofocus technique to coherent imagery prior to 1969. Special acknowledgment should go to James Auterman for his time spent in instructing me in the project's prior history and for the equipment he worked on.

I would like to thank all those who aided me in the work I have done on the coherent system. In addition to my committee, I am especially indebted to Dr. Robert Bayma for his advice and assistance in solving practical servo problems, and in the distributed target analysis. Thanks are also due to Norman Massey for his suggestions in the design of the optical system. In addition, the aid of Gary Montry, Roy Moore, James Marks, Charles Liskow and Dr. Edoardo Mosca in various other phases of the work was greatly appreciated.

Finally, I would like to thank most of all, my friends who put their personal convenience aside to help me during the last week of preparation of this dissertation. I will never forget the support and assistance of Carole Newton, who typed and retyped corrections and additions, Wally Kerce who drew up the figures, Ralph Ridenour who printed them and countless others with whom my work interferred, but who willingly stepped aside to help me.

CONTENTS

Acknowledgment ii

List of Figures v

List of Symbols vii

1. Introduction 1
   Requirement for automatic focus; history; summary of approach

2. Operating Principles 5
   2.1. Synthetic-Array Radar
   Description; nature of the errors
   2.2. Coherent Images
   Appearance; definition of problem; piecewise approach; types of images
   2.3. Focal Properties of Various Images
   Point; distributed; point pair; group; discontinuous distributed; noise; moving point; line
   2.4. Focus Procedures
   Manual focusing of coherent image; focal properties of noncoherent image; automatic focus of noncoherent image; problems of using noncoherent autofocus on coherent image
   2.5. Noncoherent Integration
   2.6. Coherent Autofocus System
   Astigmatic relay; image splitter; limiting; differentiation; threshold; peak detector with proximity weighting
   2.7. Cascaded Estimators
   Point image; discontinuous distributed; group

3. Optical System 25
   Synthetic aperture radar processors; tilted plane processor features; autofocus optical system concept; autofocus optical system design; image splitter design

4. Servo System Analysis 32
   Optical system as an adder; autofocus loop; tachometer loop

5. Point-Image Analysis 40
   5.1. Strong Point Image
   Estimator behavior for $x \neq \delta$; complete estimator behavior for television resolution limit; response time for television resolution limit
   5.2. Weak Point Image
   Exact estimator function; response time; simplified response time

6. Parametric Design for Dominant Image 54
Criteria of design; statistics of the focus error; standard focus error tracking (linear); transient recovery (nonlinear)

7. Distributed Images 60
Infinite distributed image statistics; signal/noise after noncoherent integration; finite distributed image; discontinuous distributed image (farmland); farmland signal/noise (bandpass filter); verification for differentiator system; response time

8. Intermediate Image Types 75
Very weak point; pairs; infinite point array; non-Gaussian distributions

9. Summary and Experimental Results 82
Major design equations; experimental system parameters; equipment; results

Appendix — Figures 101

References 132

Bibliography 134

LIST OF FIGURES

1. Phased Array
2. Synthetic-Array Radar
3. Typical SAR Imagery
4. Coherent Imagery Enlargements
5. Coherent Image Types and Spectra
6. Noncoherent Image and Spectra
7. Noncoherent Autofocus Block Diagram
8. Point Image Field and Focus Estimator
9. Coherent Image of Discontinuous Object with Integration
10. Coherent Autofocus Block Diagram
11. Error Estimator Block Diagram
12. Tilted Plane Processor
13. Autofocus Optical System
14. Image Splitter
15. Servo System Block Diagram
16. Focus Coordinate System
17. Servo System Tachometer Loop
18. Estimator Transfer Function
19. Simplified Autofocus Loop
20. Chi-Square Density Functions
21. Finite Distributed Image
22. Farmland Image
23. Farmland Error Function
24. Peak Detector Output — Very Weak Point Image
25. Point Pair
26. Differentiator/Peak Detector Output — Pair
27. Differentiator/RMS Detector Output — Pair
28. Infinite Array of Points
29. Detector Output; Infinite Array
30. Nongaussian Distributed Image

31. Autofocus Equipment
32. Experimental Results
33. Radar Image Width Measurements
34. Point Target and Complex Group Images
35. Point Target and Complex Group Estimator Output
36. Estimator Output vs Focus
37. Land Water Boundary Images
38. Land Water Boundary Estimator Output
39. Artificial Land Water Boundary Images
40. Artificial Land Water Boundary Estimator Output
41. Farmland Boundary Image
42. Farmland Boundary Estimator Output

LIST OF SYMBOLS

$\mathcal{F}$	mechanical friction
$\mathcal{E}$	expectation value
R	autocorrelation function; also R_e: real part
$\mathcal{J}$	mechanical inertia; also $\mathcal{J}_m$: imaginary part
ρ	resolution; also ρ_0: in-focus image resolution
ω	angular frequency
Δ	image-splitter mechanical spacing
λ	optical wavelength; also λ_r: radar wavelength
ϕ	optical signal phase
θ	image-splitter mechanical position
ν	probability of no transition within argument
τ	autofocus loop time constant; also τ_0: amplifier time constant
η	normalized peak detector decay time
ϵ	inner (servo tachometer) loop error signal
ζ	decorrelation time of optical field of view
ξ	servo loop damping constant
σ	standard focus error of data (input)
Γ	gamma function
Ψ	image intensity; also Ψ_0: in-focus image intensity; also $\bar{\Psi}_0$: in-focus image intensity average across each farm
ψ	image amplitude; also ψ_0: in-focus image amplitude
δ	image-splitter image separation in x direction
μ	gain of servo system motor amplifier
A, B, C	dimension on image splitter
D	aperture: of lens or field of view
E	estimator output voltage
F	focal length
G	servo motor constant; also G_v: velocity; also G_L: torque
I	illumination intensity in optical processor
J	Jacobian

K	normalized focus error of output image
L	servo motor torque
M	optical magnification
N	noncoherent integration factor
P	probability-distribution function
Q	normalized energy of point images after television transducer
R	motor resistance
S	lens spacings
T	target field constant
V	peak detector voltages
W	average width of a farm
X, Y, Z	particular values of coordinates x, y, z
a	radar cross section of a particular scatterer
e	motor back electromotive force (EMF)
f	lens f/number
h	radius length between given object and image points
i	motor armature current; also an index
j	$\sqrt{-1}$
k	index
m	mean value of radar backscatter coefficient for farmland
n	number of scatterers in a radar resolution cell
p	probability-density function
r	subscript denotes radar coordinate
s	standard deviation of radar backscatter coefficient from m
t	time
u	standard deviation of a_k
v	velocity of signal history film; also v_r: aircraft velocity
w	point pair spacing ($\div 2$)
x	direction along optical axis; image distance from nominal
x_0	direction along optical axis; lens distance from nominal
x_1	direction along optical axis; object distance from nominal

x', x'_0 and x'_1	nominal image, lense, or object focal positions
y	track coordinate in optical system; also y_r: radar track
z	range coordinate in optical system; also z_r: radar range

1
INTRODUCTION

Many large-aperture electronic or optical systems are required to form images of distributed objects. It is usually desirable in these systems to provide for adjustment of the second-order phase term, that is, for the focus of the system. This adjustment is conventionally performed by an operator, who observes the image and adjusts (usually, subjectively) those elements that control the focus.

In the special, but important, case of a coherent system (that is, a phased-array or synthetic-array radar (SAR) system or a coherent optical system), special procedures must be followed in order to accomplish the focusing operation. The usual procedure is to introduce a point object in place of, or in addition to, the object field to be imaged, thus allowing the steering elements of the phased array to be adjusted for minimum beamwidth (i.e., optimum focus), or to allow the coherent optical system to be collimated. One may then assume that if the point object is properly focused, the coherent image will also be in focus.

As an example, consider the phased array of Fig. 1. Because of drift or construction differences, the elements may have different phase shift (θ), delay (Δ), or gain. Adjustment of the array for beam steering (first-order) and focus (second-order phase error) is performed by introducing a corner reflector in the far field.

In many noncoherent imaging systems, on the other hand, it is highly advantageous to provide adaptive control of the second-order phase term. In these systems, defocus of the image results in a reduction in its spatial bandwidth, and devices have been configured to sense this bandwidth reduction and continually adjust the system focus for maximum spatial frequency content in the image [1]. Thus, noncoherent optical systems have been designed that will produce optimally focused images in spite of a perturbing medium.

The same need, of course, arises in coherent imaging systems, but the need is especially critical in SAR imaging systems, on which the remainder of this discussion is focused. The techniques to be discussed, however, apply directly to the focusing of phased-array, real-aperture radar systems and coherent, optical, holographic imaging systems.

The need for closed-loop control of the second-order, phase-error term in an SAR system, arises because of the many sources that can contribute to this error. The concept of SAR [2] is based upon the assumption that the aircraft flies in a perfectly straight line while the data to be processed are being collected. In addition, it is usually assumed that the path of propagation between the radar and the target field is unperturbed by atmospheric or ionospheric dispersion. Finally, it is assumed that the radar operating parameters (such as the range from the radar to the object or the forward velocity of the aircraft) are fixed. Violations of these assumptions will result in a defocused image.

Historically, systems have been designed to compensate for the first source of errors, i.e., deviations from a straight flight path. These "motion-compensation" systems [3] are usually based on inertial sensors, carried along in the aircraft which sense deviations of the aircraft from straight line flight, and open-loop corrections are applied to the radar system. Some motion-compensation systems, however, have used either Doppler radar navigators to measure the error, or the return signal from the imaging radar averaged over its beamwidth to provide the error signal (the clutter-lock system) [4]. Clutter lock, while it is a closed-loop system, suffers from the failing that antenna pointing errors which do not affect the image can lead to a miscalculation of the true focus error signal. All other sources of defocusing are normally taken up by operator adjustment when the final image is processed.

A considerable amount of effort has been expended over the past ten years to perfect a scheme for automatic focusing of coherent synthetic-aperture imagery (see, for example, Harger, Ref. 5). The initial work was on the direct application of the noncoherent focusing scheme based on the image spectrum. The difficulty that the spectrum of a distributed object does not change when the image goes out of focus was avoided by the assumption that the object field will be predominantly composed of isolated point scatterers. As long as this assumption holds, defocus results in a reduction of the spatial frequency content of the image, and direct application of the noncoherent scheme will result in good closed-loop performance. After several years of effort, the experimental work had shown that the underlying assumption of a point-target field was not good enough. Either constant operator attention was required to keep the system from locking on to a false focus, or decision-making circuitry had to be incorporated into the equipment in order to shut off the closed-loop control whenever the signal level dropped below a point at which one could be reasonably assured that the assumption of point objects was satisfied.

The approach described herein, which represents a significant departure from the initial plan, is to make the sensor respond properly to a wider class of objects. Thus, the focus estimation has been extended to include a second criterion and four new techniques. These are summarized as follows:

(1). Signal Spectrum. The criterion operates well on isolated point objects and is used as a primary criterion when the assumption of a point-object field is valid. This was the single original criterion.

(2) Signal Amplitude. If the field consists of a number of point scatterers in close proximity, defocus of the image will not change the spectrum of the image; however, the peak amplitude of the multiple point scatterers will be reduced. This criteria is new.

(3) Noncoherent Integration. The coherent data bandwidth is divided into subbands. The phase information between them is destroyed, and the bands are summed noncoherently. This technique improves the ability of the autofocus system to operate on multiple point objects and allows it to give a useful focus error signal for distributed objects (such as terrain).

(4) Point Proximity. A weighted average is formed which favors the isolated point object in a field which includes multiple points, distributed objects, and isolated single scatterers.

(5) Thresholding. Thresholding is a final preventative measure which shuts down the system when there are no signals present. This procedure is necessary, because there is no way to focus a random signal (e.g., thermal noise), and it is necessary to prevent a drift of the system focus in the areas where, in fact, there is no image.

(6) Limiting. This measure avoids placing undue emphasis on very strong isolated point objects. Sometimes, the focus of a single-point scatterer may represent a very poor average focus for the entire scene (for example, if the strong object happens to be moving). Limiting avoids domination of the focusing system by very large targets.

This dissertation presents the results of analytical investigations, and describes a constructed experimental system which has allowed verification of the basic concepts involved in closed-loop focus control of coherent synthetic-array imagery.

2
OPERATING PRINCIPLES

2.1. SYNTHETIC-ARRAY RADAR

The principle of operation of the SAR is illustrated in Fig. 2. A vehicle, usually an aircraft, is equipped with a coherent radar system and recorder. The radar (physical) antenna is mounted on the vehicle so that the antenna beam is oriented perpendicular to the line of flight of the vehicle, which in turn is chosen so that the strip of ground to be imaged is illuminated. The coherent radar system is usually of the pulsed Doppler type, and the pulse repetition interval is chosen so that radar transmissions occur from each of the contiguous antenna positions illustrated in Fig. 2. Thus, after a period of time has elapsed, the area to be imaged has been illuminated sequentially by the elements of what we now call a synthetic array. If the return signals are properly processed, therefore, it is possible to obtain angular resolution commensurate with the length of the synthetic array, which may be many hundreds of times larger than the length of the physical antenna carried by the vehicle.

The most popular processing technique bears a close resemblance to optical holography, and is illustrated in the lower half of the figure. The radar signals are recorded on film in the vehicle by imaging a line trace from a cathode-ray tube (CRT) onto a translating strip of film. The CRT trace is synchronized with the radar transmissions so that the position of the spot becomes proportional to range from the radar. This trace is then imaged onto the film so that the lateral direction across the film becomes proportional to the range from the radar, and longitudinal position along the film is proportional to the vehicle position along the ground track relative to the terrain. The coherent received signal is phase-detected and then applied as an intensity modulation to the CRT. Thus, film density becomes proportional to the phase of the radar return signal.

After the film is developed, it is illuminated optically from behind with a plane monochromatic wave. This wave, when it is diffracted by the signals recorded on the film, creates wavefronts which are scaled replicas of the wavefronts that were received by the SAR. Of course, the SAR wavefront was time-sampled, whereas the recreated wavefront is generated all at one time. Hence, the film and the replica wavefront is referred to as the signal history. Since the direction of propagation of the replica history wavefront is opposite to that of the parent radar wavefront, the signal history wavefront will come to a focus, creating in optical processor space, a replica of the terrain illuminated by the radar system.

If we denote the position of an arbitrary point object in radar space by x_r, the radar wavelength by λ_r, and the vehicle velocity by v_r, and the scaled optical wavelength, film speed, and optical image position by λ, v, and x, it is easy to show that

$$x = x_r \times \left(\frac{v}{v_r}\right)^2 \times \frac{\lambda_r}{\lambda} \times \frac{1}{2} \qquad (1)$$

An image film is now placed at the position z in order to record an image of the terrain. If, however, because of a failure in the radar system or in our calculation of expected x, the image film is placed incorrectly, the recorded image will be out of focus, and a loss of detail will occur. Some of the sources of potential image defocus may be identified by means of Eq. (1). First, if the ratio of v to v_r changes because of accident (perhaps the vehicle was caught by a gust of wind) or because forward speed was deliberately changed, x will change correspondingly. In order to avoid the first of these problems, motion-compensation systems are generally used. However, since these are open-loop systems that depend upon inertial references in the aircraft to detect changes in velocity, they are never

perfect. Second, because of atmospheric inhomogeneity, differences in radar propagation might be encountered, leading to changes in λ_r. Since there is no way to measure this phenomenon in flight, the only alternative is to refocus the image by hand while the processing is being performed. Third, there may be a deliberate change in x_r by the radar operator; if so, drastic refocusing of the image is necessary.

The major source of defocusing of the image, however, can be shown to be the result of cross-track velocity errors, that is, the unpredictable motions of the vehicle in a direction perpendicular to its nominal direction of flight. The SAR is extremely sensitive to this particular type of error because unwanted cross-track motions cause warpage in the surface of the synthetic array. As in any antenna system, the surface of the synthetic array should be held within a fraction of a wavelength to a straight line. For most of the SAR's operating at X-band, this means that deviations of the flight path of the vehicle from a straight line must be held to within fractions of an inch over synthetic-array lengths on the order of hundreds or thousands of feet; even the best inertial motion-compensation systems cannot calculate cross-track deviations to this accuracy.

As might be expected, it is found that disturbances in the cross-track direction are fairly random (at least when the vehicle is an aircraft). However, because the mass of the vehicle is high, cross-track deviations become more predominant at low frequencies. Thus, deviations with periods on the order of a cycle across the synthetic aperture will have larger amplitudes than deviation components of several cycles across the aperture. In addition, the motion-compensation systems used to sense these cross-track motions are inertial; hence, they respond more accurately to the high-frequency error components, leaving the low-frequency error components more poorly corrected. Thus, in practice, large amounts of image degradation caused by cross-track unknown velocities may be removed by simply adjusting the focus of the processor.

2.2. COHERENT IMAGES

An image typical of the type obtained from an SAR is shown in Fig. 3. At first glance, this image bears a remarkable resemblance to an aerial photograph or optical image of the terrain; however, upon closer examination, many dissimilarities can be found. Some of these are the result of fundamental causes such as the large difference between radar wavelengths and optical wavelengths and the unique geometry of the radar sensor (its natural coordinates are range and angle in contrast to the camera's angle-angle coordinates). However, perhaps the largest dissimilarity between visual and radar imagery is the fact that radar imagery is coherent or monochromatically illuminated.

This difference is illustrated in Fig. 4, which is an extreme enlargement of a small area of Fig. 3.. The major difference between the appearance of the imagery in Fig. 4 and that of an enlargement of noncoherent imagery is that the intensity of a particular coherent image resolution cell is the result of the vector addition of the signals from each of the many scatterers contained within the resolution cell. In a noncoherent imaging system, the intensity in a particular resolution cell is simply the sum of the power of the return signals from each scatterer. Thus, in the coherent image, many resolution cells are dark as a result of cancellation of return among scatterers. In a noncoherent image, cancellation is not possible.

The distinction becomes even more dramatic when one examines the result of defocusing the image. In the noncoherent case, defocusing results in an image which approaches a uniform gray as defocusing is increased, with a consequent loss in image detail. In the coherent case (illustrated in Fig. 4b), defocusing results in an image of the same contrast; the image structure does not disappear (as in the noncoherent case), but its structure changes, and the new structure has just as much apparent detail as that of the correctly focused image.

The detail, however, is meaningless. A particular example of the replacement of meaningful by meaningless structure is shown in Fig. 4. The spread of the point image in azimuth illustrates the focus quality. Another way of stating the problem is as follows: in a noncoherent case, defocusing results in a loss of detail in the image, accompanied by a decrease in its spectral bandwidth. In the coherent case, defocusing results in a replacement of significant detail by random detail, and the bandwidth of the image does not change significantly.

The foregoing discussion has provided the background with which we may define the problem to be treated in this dissertation:

(1) Given an output image, what criteria can be used to estimate the focus parameter?

(2) Using these criteria, how may we implement a closed-loop focus-control system?

(3) What parameters of the control system determine the performance of the system, and how may loop performance be optimized?

A unified approach to determining the optimum estimator of focus in a coherent system may be extremely difficult, because some of the simplifying assumptions necessary to such an approach may totally invalidate the results. For example, a simplifying assumption commonly made is that the target field consists of uniform, random, Gaussian noise. Under these conditions, analysis becomes manageable. However, it can be demonstrated that a uniform Gaussian target field is devoid of intelligence, and that defocus of the image results in change in neither the statistics nor the intelligence of the image; thus, no estimator can be found. Since this assumption produces a negative result, it will be tempting to consider a different class of assumptions, for example, that the target field consists entirely of isolated point targets. This assumption also leads to a

simplified analytic approach, the identification of an efficient estimator. However, system designs based only on this type of estimator have been shown to fail for a wide variety of image types; specifically, whenever either too few or too many points appear in the image.

The approach that will be taken in this dissertation, therefore, will be to divide the object field into several classes, each representative of a major image type. Both the effect of defocusing on each of the image classes and an efficient estimator for each class will be determined. A combination system will be suggested, which combines the properties of the various estimators. In particular, it will be shown that the various estimators can be combined with only a small loss of efficiency of estimation.

The important image types will be classified according to the following list:

(1) Fixed point — isolated
(2) Moving point
(3) Groups or clusters of points
(4) Lines
(5) Distributed or extended diffuse scatterers
(6) Voids (areas of little or no reflectivity contained within much larger areas of distributed image), or discontinuous distributed images
(7) Thermal noise

2.3. FOCAL PROPERTIES OF VARIOUS IMAGES

In order to gain an intuitive understanding of what criteria might be useful in estimating focus, we will examine each image type individually. In Fig. 5, we illustrate the image and the spectrum of the image* for each of the classes listed above. The image of a point is, of course, well defined and localized in space, and its spectrum (determined by the radar doppler frequency response) is usually a

*Defined here as the one-dimensional Fourier transform of the image intensity (not amplitude).

smooth monotonically decreasing function. The width of both the image and the spectrum is determined by the resolution of the radar system. When the image is defocused, its intensity is decreased, and the width is increased. Consequently, the spectrum of the out-of-focus image is decreased in bandwidth. We might expect, therefore, that either the intensity of the image or the width of the spectrum (or both) might be an efficient estimator of focus.

On the other hand, the image and spectrum of a distributed object shows little indication of whether the image is in focus or not. Both the peak amplitude of the image and the spectral bandwidth remain constant. Of course, the image structure changes as the focus is adjusted but, in the case of an ideal, randomly diffuse object, the structure is entirely accidental and is just as meaningless when the image is focused as when it is out of focus. Let us therefore examine the process more carefully so that we may understand how rapidly the situation deteriorates.

Figure 5c illustrates a pair of points that are clearly separated when the image is in focus, but which overlap when the image is out of focus. As in the case of the single point, we see that the intensity of the image decreases as the image is defocused and as the energy in the two points becomes spread over a wider region of space. The spectrum also changes between the focused and defocused images, but here the change is not as easily categorized as in the case of the single point target. In particular, if one were to try to use the spectral width of the image as an estimator of focus, considerable difficulty might be anticipated, because of the strong high-frequency components in the defocused image.

To generalize a bit further, we consider the group of strong points illustrated in Fig. 5d. Here we have shown a few points randomly spaced in both position and amplitude. When the image is defocused, it becomes very similar to the randomly diffuse object

discussed previously. The spectrum changes very little between the in-focus and out-of-focus images. However, the peak amplitude of the image is distinctly reduced. This phenomenon will be discussed in greater detail in a later section where it will be shown that the effect is a result of the central limit theorem. The result, however, strongly indicates that the more efficient estimator is the peak amplitude or intensity of the image, in this case, rather than the spectrum. If the image is intelligible, the distribution of the image amplitude is non-Gaussian, and the variance-to-mean-square ratio of the image intensity is high. The process of defocusing the image causes the distribution to approach the normal one and the variance-to-mean-square ratio approaches unity.

Figure 5e shows a target type called "discontinuous distributed" which includes such image elements as farm land, land/water boundaries, partially forested and partially open terrain, airport runways, or roadways passing through areas of more or less uniform intensity. We have chosen for illustration in Fig. 5e, the land/water boundary represented by a uniformly distributed image gated by a step. As with the continuous distributed object, image defocus results in only a small change in the spectrum of the image. Likewise, the peak and average values of the image intensity are also not greatly affected by defocusing, and the variance-to-mean-square ratio of the in-focus and out-of-focus images are both approximately unity. In this case, however, there is a distinct change in the appearance of the imagery; therefore, we should expect that an efficient estimator of focus exists, in spite of the fact that the spectral width or amplitude-dependent estimators are almost useless. For example, one potentially useful estimator might be formed by summing (separately) the image intensities in several resolution cells on both sides of a scanning boundary. The difference between these two partial sums is used as a focus estimator. The estimator reaches a maximum when the boundary coincides with the image interface with the image in focus.

Although this estimator will allow us to measure the focus of the image, it is a difficult method to implement. There is, however, another procedure available which is equivalent in concept and considerably simpler to implement, and we will return to this point later.

Another image class of great practical importance is random noise. We must learn to deal with random noise because most synthetic-aperture imaging systems have a finite sensitivity; using such systems to image areas that contain extended open water surfaces or flat, featureless, desert terrain will, in fact, produce only images of the radar noise. Of course, the focal properties of this noise image are identical to the continuous distributed object, and, indeed, the image has no focus. However, if we design an automatic focusing system which does not take into account the possible presence of an unfocusable signal, we may very well find the system pulled irretrievably far away from focus by the randomly fluctuating noise image. Then when an image reappears, it will be so badly out of focus that it too will appear to be continuously distributed, and the system will be unable to obtain a focus relock. The practical solution in this case is the inclusion of a threshold. The threshold operates on the moving lens system and is actuated by the absence of an appropriately large focus estimator, and not by the brightness of the image. Thus, the automatic focusing system is shut down whenever the focus estimate becomes unreliable.

The two remaining object types, the moving point and the line, must be discussed exclusively in the context of SAR systems.

In an SAR system, the component of motion of a point scatterer in the range direction causes an along-track shift in the position of the image of that point, but otherwise will cause no difficulty in estimating the focus of the image. On the other hand, the component of the motion in the direction parallel to the motion of the radar

causes an apparent change in v_r (see Eq. 1). Since v_r is really the relative aircraft-to-target motion, changing v_r causes a change in the focus of the image. Moving objects with substantial along-track velocity components will typically image as if they were badly out of focus, even though the environment is quite accurately in focus. Focusing an image of a moving object defocuses the environment. If the moving object happens also to be the strongest point object in the field of view, the focusing system may be pulled out of focus lock.

The effect of the moving object can be reduced by limiting the peak amplitude of the image to avoid capture of the focusing system by extremely strong scatterers. If the moving object is the only one in the field of view or is important to the image interpreter, there is no harm done by allowing the focusing system to respond slightly to this signal.

The line object is unique in SAR systems because focus is required in one dimension only, the along-track direction. Thus, line objects may be treated as points as long as their orientation is not parallel to the line of flight of the vehicle. Since this occurrence is usually accompanied by the appearance of perpendicular lines also, only slight loss in generality will result from treating the two cases together.

2.4. FOCUS PROCEDURES

Manual focusing of coherent imagery by the human operator is quite unlike the procedure used on noncoherent imagery (e.g., focusing a slide projector or telescope). The usual procedure in focusing coherent imagery is to examine large areas of the image to locate isolated points. This step requires a considerable amount of a priori knowledge about the focus of the image, and an unskilled operator may search in vain over large areas of data film and finally focus only scratches and imperfections in the optical system. Once the operator finds one or a few points, he attempts to adjust the focus to

minimize the width of those points, since his eye is particularly insensitive to intensity. This procedure is equivalent to that described previously; i.e., maximizing the spectral bandwidth of the image of an isolated point. Unfortunately, points tend to occur in clusters or groups, and several attempts are probably required before the operator finds a point and is able to focus it accurately.

Having obtained a preliminary focused image, the operator repeats his search for other points scattered throughout the image. He then estimates the focus of each sample in order to arrive at some kind of average estimate, weighted according to his subjective evaluation of the causes of the differences in focus between the samples. This procedure is an art more than a science; indeed, the number of well trained individuals who can perform this procedure satisfactorily is very low.

Automatic focusing of coherent imagery is based upon the automatic focusing scheme used for noncoherent images. Figure 6 illustrates the major features of a typical noncoherent image and shows what happens to the image and its spectrum when focus is misadjusted. First, we notice that the image is composed of large areas of relatively uniform or slowly varying intensity, but that these areas are separated by sharp discontinuities. Thus, most of the detail of a noncoherent image is carried in the boundaries or interfaces between these large uniform areas. The image highlights may be contained within a few isolated points of maximum intensity, but are more likely to be contained in one or more of the large uniform areas. In general, the result of defocusing the image is to moderate the boundaries; i.e., the transition between large areas of differing intensity becomes less abrupt. If the image is drastically defocused, it will become a uniform gray, and the highlights will disappear. However, for small changes in focus, the peak intensity of the image does not change very much. Hence, image intensity is not a good estimator of image focus.

On the other hand, the high-frequency portion of the image spectrum is caused by the abrupt discontinuities in the image, and as the image is defocused, the high-frequency portions of its spectrum attenuate rapidly. Thus, the width of the spectrum becomes a more efficient estimator of noncoherent image focus than the image intensity.

One implementation for automatic focusing of noncoherent imagery is shown in Fig. 7. The object is located to the left of the camera lens, and an unexposed photographic plate is placed near the focal point of the lens. The camera lens is equipped with a motor-driven mechanical positioning system. Two partially reflecting mirrors are placed in the converging beam of light to allow two secondary images to be formed side by side on the photocathode of a television camera. If the noncoherent image is in focus at the film plane, the positions of the partially reflecting mirrors will be such that the two secondary images will be equally out of focus, with the left-hand, secondary-image focal point behind the photocathode and the right-hand focus an equal distance in front. Thus, a slight misadjustment in the focus in the image at the photographic emulsion will cause one or the other of the secondary images to be in better focus than the other. The focus of the two secondary images are estimated by measuring their high-frequency content with the use of a high-center-frequency bandpass filter. The average difference between the two estimations is found, and this error signal is used to drive the mechanical positioning system.

The shape of the error signal is shown at the bottom of Fig. 7. If the lens position is adjusted so that one of the two secondary images is in focus, the error signal reaches a peak. The polarity is determined by which of the two images is in focus. An approximately linear change in the error signal is obtained in between, and the error signal is zero when the two images are equally out of focus (i.e., when the

two secondary images have equal high-frequency content). Large focus errors cause the error signal to fall off again leading to a loss in loop gain of the automatic focusing system; however, because the error signal will never cross zero at other than the true focus position, the closed loop will eventually find its way back into the high-gain portion of the operating characteristic.

Early efforts to develop an automatic focusing scheme for coherent imagery were based almost entirely on the schemes developed for noncoherent images. The rationale used to justify this approach was that most operators focus a coherent system on the basis of point objects, and, as described previously, the noncoherent focusing scheme of Fig. 7 will work quite well on a field of isolated points. After considerable experimental work, however, difficulties were encountered. First, it was found that even an isolated, point-target field with a sufficient number of points to give an accurate focus estimate in the implementation of Fig. 7 would become a multiple point-target field when the image was sufficiently defocused. This phenomenon is illustrated in Fig. 8. Sufficient defocusing of the point-target field results in an overlap of their defocused images. Since the system is coherent, the area of overlap interferes in a constructive or destructive way and generates false image structure. This causes the error signal of Fig. 7 to fluctuate across the zero error line when the focal estimate is badly in error; zero crossings which correspond to the proper (negative) slope of the error signal become points at which the focusing loop can lock stably.

This problem by itself would not be too severe if the system could be kept from going too far out of focus. However, in the typical image, the absence of points over large areas causes a drift of the automatic focusing system into the false focus region of the error signal. Of course, the system can be shut down when the error signal falls below a certain predetermined level by means of a threshold. However,

if focus changes by a large amount during shut down, operator reset is required.

2.5. NONCOHERENT INTEGRATION

We have previously suggested an estimator, pg. 12, for use on discontinuous distributed images, that relied upon summation of independent samples of image intensity. This process of noncoherent integration is an attempt to make coherent imagery behave more like noncoherent imagery. In Fig. 5e, we have described the appearance of a large extended object of uniform intensity (e.g., a grass field), situated adjacent to an area of zero intensity (e.g., a lake). The equivalent noncoherent image of the same object is shown by the dashed line in Fig. 5e. The difference between these two has been called coherent breakup or image speckle and is the result of the formation of the coherent image by either a monochromatic laser or a monochromatic radar. The sharp peaks and nulls in coherent image is caused by constructive or destructive interference of the return signals from each one of the scatterers (blades of grass). It has been known for some time that a coherent image may be converted into a noncoherent one by a noncoherent integration process (sometimes called "mixed" or "multispectral" integration). To illustrate how this process works, let us imagine that the coherent imaging systems can be increased in resolution by a large order of magnitude (N), producing the image shown in Fig. 9a. Here the basic nature of the speckle or coherent breakup has not been changed, but the granularity (or decorrelation) distance has been decreased by the same factor (N) that the bandwidth and the resolution of the radar system has been increased. Let us assume further that this new fine resolution of the coherent system can be destroyed noncoherently. This destruction could be done perhaps by the use of a low-resolution photographic emulsion to capture the final image or by oscillating the image film through N resolution cells during a time exposure of the image. The result of this operation

would be to reduce the resolution of the image to its original value. In the process, the coherent breakup would be averaged out, resulting in the image shown in Fig. 9b. Thus, the coherent image has been converted to a partially noncoherent one of equal resolution. Defocus of the image now results in a severe narrow banding of the image spectrum, as shown in the remainder of Fig. 9. Thus, the larger N is made, the better the noncoherent automatic focusing scheme of Fig. 7 would work on distributed objects.

Multispectral processing will be examined in greater detail in Section 7. We need only say that whatever excess bandwidth is available in the radar sensor, beyond that required for the resolution desired in the image, can be used to smooth the image speckle. However, in most cases the image will not be sufficiently smoothed that the noncoherent automatic focusing scheme can be successfully applied directly. We will therefore now turn our attention to a combined system which is designed to capitalize on all the significant focal properties of a coherent or partially coherent defocused image.

2.6. COHERENT AUTOFOCUS SYSTEM

The previous discussion has outlined the background that led to the choice of a focus estimation and control system for coherent imagery. This system is shown in Fig. 10. It is designed to take advantage of whatever information is contained in the image to form a reasonable accurate estimation of the focus of the image.

The general concept of the coherent focusing system is similar to the concept of noncoherent system described in Fig. 7; however, the detailed optical system and weighted error estimation procedures are quite different. As described before, a lens in the primary optical system produces a coherent image near its focal point, and an unexposed photographic plate is placed to capture the image.

The automatic focusing system receives its pair of secondary images via a half-silvered mirror and an image splitter. The double secondary image is then relayed through an astigmatic optical system onto the photocathode of the television camera. The focus estimation is then performed electronically on the two images. The two estimators are demultiplexed, averaged, and differenced as before to generate an error signal, and the error signal is used to drive the lens.

The optical system will be described in detail later; however, the function of the system is to allow for a separately adjustable magnification in the two coordinates of the image, i.e., in the range and angle directions, in order to allow some noncoherent integration to be performed on the photocathode of the television camera. The optical imaging system demagnifies the image in the range direction, so that the resolution of the photocathode becomes poorer than the optical resolution of the coherent imaging system. Thus, an order of magnitude of noncoherent integration is obtained in the range direction. Some noncoherent integration is also desirable in the along-track direction; however, we must choose between the advantages of a smooth image and the disadvantages of the loss of ability of the automatic system to come to an exact focus. Thus, in the along-track direction, the optical relay system provides a magnification of the image, and the television resolution element size in the along-track direction becomes approximately equal to the track resolution of the coherent optical system. The provision for separately controllable y and z magnification in the astigmatic optical relay system allows further noncoherent integration to be performed in the y direction, if desired.

Since a relay system is required to adjust the magnification of the image, the image splitter arrangement shown in Fig. 7 has been modified as shown in Fig. 10. The image splitter shown in Fig. 10 is more convenient for several reasons. First, the two secondary

images are balanced in intensity. Second, only one partially silvered mirror need be placed in the primary optical path, leading to better primary image quality. Third, the secondary image splitter is more easily mechanically adjusted to control the relative positions of the two secondary images and their relative focus. Finally, because the secondary image splitter is almost at the image focal plane, very little deterioration of secondary image quality results from this arrangement. Other than these practical differences, however, the image splitter is conceptually identical to the one shown in Fig. 7.

The weighted error estimation, shown in Fig. 11, is the heart of the coherent focusing system. After the astigmatic telescope and the television camera perform the noncoherent integration function, limiting is applied in the television system to avoid capture of the focusing system by a strong, moving point object. The signal is then differentiated. The desired function is the measurement of the high frequency content of the image. In this sense the differentiator and the low-pass filtering in the TV camera provide approximately the same measurement as a high-frequency bandpass filter. The output of the differentiator is provided to both a detector and a disable circuit. Within the disable circuit, the peak and rms values of the signal are measured, and the ratio of these two values is obtained. The ratio of peak to rms signal levels of Gaussian noise is about two, hence when this ratio approaches two, the detector is back-biased, thereby shutting down the automatic focusing system. This procedure prevents the drift of the focusing system in the absence of a strong error signal.

The differentiator, however, does not provide optimum estimation for groups of point targets. Therefore, two functions are provided by the detection circuit. The first is peak detection, which is accomplished quite simply (as shown in the lower half of the figure) by making the detector filter capacitor large and by driving the detector from a low impedance. The ratio of the charge-to-discharge time constants determines how well the circuit will respond to peaks in the signal.

The detector circuit also provides point-target proximity weighting. The most convenient object type to use as a basis for focus estimation is the single isolated point; therefore, it would seem to be desirable that the error estimator should respond more to points that are isolated than to groups of points or to distributed objects. Also, if a single, strong point happens to be located in an environment of a group of smaller points, it would be desirable if the focus were adjusted primarily on the basis of the single large point since a better estimate of focus might be obtained. The detector circuit shown in the figure performs this function, as shown by the waveforms accompanying the circuit. When a strong point is scanned, an input voltage to the detector something like V_{in} might be obtained. Since the driving impedance is very low, the capacitor voltage V_c follows the leading edge until the capacitor is charged to the peak value of V_{in}. Because the capacitor discharge circuit is inductive, the capacitor voltage will remain high for some time after the input voltage has dropped back to zero. If, therefore, the strong point is located in the vicinity of a slightly weaker point, as indicated in the figure, the capacitor voltage will be unaffected by the presence of the second point. The closer the second point is to the first one, the stronger it must be to influence the output of the detector. Hence, the response of the detector to the second point is weighted by its proximity to the first one. Even if the weak point precedes the strong one, the detector output will be dominated by the stronger.

2.7. CASCADED ESTIMATORS

Let us consider whether the inclusion of several estimators should influence the efficiency of estimation for any particular object type. In order to do this, we will consider each type in turn and decide whether the circuitry included to form an estimation of the other types can cause a deterioration of the estimation of focus for the object under consideration. For the remainder of the discussion,

the high-frequency bandpass filter will be treated as a differentiator. (The television camera has an upper frequency cut-off commensurate with its resolution; therefore, the series combination of the TV camera and the differentiator is equivalent to the high-frequency bandpass filter).

Beginning with the isolated point, we see that the use of noncoherent integration does not affect either the appearance of the image or its focal properties because both coherent and noncoherent images of points appear identical. Furthermore, both spectral analysis and peak detection are efficient estimators for isolated points. In particular, differentiation of the image and detection of the peak amplitude of the differentiator output should form an even more efficient estimator than either of the two techniques alone. The same argument is applicable to moving points and lines.

Consider next the discontinuous distributed object. As stated previously, noncoherent integration is required before any reasonable estimation of focus can be performed. The noncoherent integration turns the distributed object field into an area of uniform constant intensity; i.e., it turns the coherent image into a noncoherent one. Sudden discontinuities in the radar backscatter coefficient then results in an intensity step in the image. Differentiation changes the intensity step into a pulse. An estimate of focus may be obtained by peak detection of the output of the differentiator. This can be seen by imagining the image to go somewhat out of focus, which causes the intensity step to become somewhat less abrupt and the differentiator output pulse to become smaller in amplitude and broader. The energy of the differentiator output pulse decreases as rapidly as the amplitude. Peak detection measures the amplitude of the pulse.

The final object type is the group or cluster of points. Since component points in the cluster consist, for the most part, of real objects, noncoherent integration can improve the image, since it tends

to eliminate the artificial coherent breakup (those points that are not real) and makes the image more conducive to spectral estimation.

The effect of differentiation of this image is somewhat more difficult to predict intuitively. If the individual points in the cluster are separated by more than a resolution cell, differentiation will not reduce the variance-to-mean-square ratio of image intensity and, hence, will not destroy the effectiveness of peak detection in estimating focus. If a large amount of noncoherent integration is performed, the spectral analysis performed by the differentiator can improve the focus estimation over simple detection in the same way that it does for the discontinuous distributed target.

We have described intuitively how a particular implementation of a closed-loop, automatic focusing system might operate on coherent imagery of various types. In the sections to follow, we will describe in detail the system design. In addition, a parametric analysis is presented that will enable us to establish general relationships between performance and parameters. Specific values can then be chosen for optimum performance with any particular radar or data.

3
OPTICAL SYSTEM

The detailed design description of an SAR optical processor will not be given in this dissertation but may be found in several references [6]. The particular configuration used in the course of the automatic focusing experiments was the tilted-plane, telescopic, optical processor shown in Fig. 12. The basic elements of the processor are the laser operating at 6330 Å, the beam expander and collimator, the tilted-signal-plane, liquid film gate, the spherical telescope used to perform the Fourier transform operation, the frequency plane filter placed at the Fourier transform plane of the spherical telescope, the cylindrical telescope used to shorten the focal length of the signal histories in the along-track direction and to bring the along-track focus into spatial coincidence with the range focus of the signals, the image plane aperture, and the image recording camera.

A detailed description of the tilted-plane processor will also be found in Ref. [7]. However, a summary of several of its characteristics that are important to automatic focusing is in order. First, the image plane of the processor is tilted, as shown in Fig. 12, with respect to the optical axis of the processor. Second, the image is geometrically undistorted. Third, the output image tracks the image film; hence, the image film is time-exposed. The exposure time is adjusted by the image plane aperture, and the field of view (in the along-track direction) as seen through that aperture is generally on the order of a few hundred resolution elements. Fourth, the range focus of the processor is adjusted by moving the image camera; then azimuth focus is adjusted separately by sliding the cylindrical telescope as a unit along the optical axis. Fifth, because of the telescopic lens system, focusing the image does not affect the geometric fidelity of the image; in other words, even large changes in the position of the cylindrical telescope do not affect the apparent position of particular

targets within the field of view, nor do they change the scale of the image in the along-track direction. The axis of the cone of rays that form the image of a target is parallel with the optical axis of the processor, regardless of the position of the target within the field of view.

In order to perform automatic focusing on this processor, two small modifications were made. First, a beam splitter was placed between the cylindrical telescope and the image plane aperture. Thus, a second replica image plane tilted with respect to the optical axis is formed. The second modification is the addition of a motor drive to allow electrical positioning of the cylindrical telescope.

A detailed drawing of the automatic focusing optical system is shown in Fig. 13. It consists of an image splitter to separate the single image produced by the processor into two images that are separated in both the along-track (y) direction, and in the focal (x) direction along the optical axis. The two images are not separated in the range (z) direction.

The two images are then passed into a mixed (consisting of spheres and cylinders) optical system. In the range (z) direction, one cylinder and the converging sphere form a demagnifying telescope. The purpose of this telescope is to reduce the size of the image (slightly) in the z-direction to fit the photocathode of the television system. Since the split image is tilted in this plane, the output image on the photocathode will also be tilted and will not fall exactly on the cathode. However, since the resolution of the television system is very low compared with the resolution of the image, the photocathode can be placed in an erect position, and the image will still remain within the depth of field of focus.

In the along-track (y) direction, a second cylindrical lens of much shorter focal length forms a second magnifying telescope with the aforementioned sphere. Since magnification is very high in this

direction, the along-track cylinder is tilted to be parallel with the split image. This procedure places the image in an erect position in relation to the along-track focus, so that a correctly focused image is formed on the photocathode. If we know the parameters of the image, we can calculate the required focal lengths and apertures of the various cylinders and spheres required in the telescope system. Let

ρ_o = the range and track resolution at the processor output

ρ_4, D_4 = the TV system resolution and field

M_{z04}, M_{y04} = magnification in range and track directions

$f_{z0, y0}$ = the image f/number at processor output

D, $F_{1, 2, 3}$ = the aperture focal length of the track cylinder, range cylinder, and sphere

$S_{01, 12, 23, 34}$ = lens spacings

From the telescope configuration

$$S_{34} = F_3,\ S_{01} = F_1,\ S_{02} = F_2,\ S_{13} = F_1 + F_3,\ S_{23} = F_2 + F_3 \quad (2)$$

where S_{13} is measured at the center of the aperture. In the experimental system, S_{23} was shortened to its practical minimum, giving

$$S_{13} = S_{23} + S_{12} = S_{02} - S_{01} = F_2 - F_1 \quad (3)$$

Thus, the optical system was shortened at the expense of introducing slight aberrations. The magnifications are

$$M_{z04} = \frac{D_4}{D_{z0}} = \frac{F_3}{F_2}$$

$$M_{y04} = \frac{\rho_4}{\rho_0} = \frac{F_3}{F_1} \tag{4}$$

The apertures of the first cylinder are

$$D_{z1} \cong D_{z0}$$

$$D_{y1} = 3D_{y0} + \frac{F_1}{f_{y0}} \tag{5}$$

where the image width D_{y0} is increased three times by the image splitter. The apertures of the second cylinder are

$$D_{z2} \cong D_{z0} \tag{6}$$

$$D_{y2} = 3D_{y0} \times \frac{S_{12}}{S_{01}} + \frac{F_1}{f_{y0}}$$

$$\cong 3D_{y0} \times \frac{F_2 - F_1}{F_1} \cong \frac{3D_{y0}F_2}{F_1} \tag{7}$$

The sphere aperture is

$$D_{z3} = D_{y3} \cong D_{z0} = D_3 \tag{8}$$

However, since $S_{23} \cong 0$, we must also have

$$D_{z0} = D_3 \geq D_{y2} = 3D_{y0} \frac{F_2}{F_1} \tag{9}$$

Then from (4)

$$\frac{3D_{y0}}{D_{z0}} \leq \frac{F_1}{F_2} = \frac{M_{z04}}{M_{y04}} = \frac{D_4 \rho_0}{D_{z0} \rho_4}$$

or

$$\frac{3D_{y0}}{\rho_0} \leq \frac{D_4}{\rho_4} \tag{10}$$

Thus, using all the TV resolution cells in the track direction corresponds to filling the lens aperture (of the larger lens 2 and 3), and the minimum aperture of these lenses is D_{z0}. Conversely, the TV system must satisfy Eq. (10).

A satisfactory procedure is to select F_3 so that the sphere has a comfortable f/number (f_c); then, the other parameters follow:

$$
\left.
\begin{aligned}
F_3 &= D_{z0} f_c \\
F_2 &= \frac{F_3 D_{z0}}{D_4} = \frac{D_{z0}^2 f_c}{D_4} \\
F_1 &= F_3 \frac{\rho_0}{\rho_4} = \frac{D_{z0} f_c \rho_0}{\rho_4} \\
D_3 &= D_2 = D_{z1} = D_{z0} \\
D_{y1} &= 3D_{y0} + \frac{F_1}{fy_0}
\end{aligned}
\right\} \qquad (11)
$$

The f/number of the first cylinder (f_1) is slightly less than the object f-number (f_{y0}) from Eq. (5):

$$f_1 \cong f_{y0} \qquad (12)$$

The amount of noncoherent integration obtained in range (N_z) is

$$N_z = \frac{\rho_4}{D_4} \times \frac{D_{z0}}{\rho_0} \qquad (13)$$

The image splitter may be designed as follows:

Let 2δ = the spacing of the two images in the x direction

Δ = the physical separation of the reflecting surfaces

θ = the angle between the x direction and the normal to the reflecting surfaces

Also, we will set up the splitter so that the processor output image of width D_{y0} produces two images of width D_{y0} separated by D_{0y}. Thus, the input to the telescope has a width of $3D_{y0}$. The center-to-center separation is $2D_{y0}$, and by ray tracing

$$B = \Delta/\cos\theta$$

$$C = B \sin 2\theta = \frac{\Delta \sin 2\theta}{\cos\theta}$$

$$A = B \cos 2\theta = \frac{\Delta \cos 2\theta}{\cos\theta} \tag{14}$$

where A, B, and C are the dimensions shown in Fig. 14, and

$$2D_{y0} = C = \frac{\Delta \sin 2\theta}{\cos\theta} \tag{15a}$$

$$2\delta = A + B = \frac{\Delta}{\cos\theta}(1 + \cos 2\theta)$$

Or the inverse,

$$D_{y0} = \frac{\delta \cos\theta \sin 2\theta}{(1 + \cos 2\theta)\cos\theta} = \delta \tan\theta$$

$$\theta = \tan^{-1}\frac{D_{y0}}{\delta} \tag{15b}$$

4
SERVO SYSTEM ANALYSIS

The automatic focus loop constitutes a nonlinear control system, primarily because of the S-shape transfer curve of the focus estimator, as shown in Fig. 7. However, because for small focus errors this transfer curve is linear and gain is maximum, we may perform a linear stability analysis to determine the upper limit of stable gain allowable, and the resulting minimum loop response time.

The loop configuration is shown in Fig. 15. The image passes through the movable cylindrical lens in the SAR processor, and the focus is estimated to give a voltage, E, that is a function of focus error, x, and the target field, T_0.

The parameter T_0, which will be explored in greater depth in the next section, includes the effects of the number and intensity of point targets, the extent and contrast of distributed targets, and the "gain" of the estimators. For the time being, however, T_0 will be taken as a simple multiplicative factor for small signals and $E(x, T_0)$ becomes

$$E(x, T_0) = T_0 x \tag{16}$$

The operation of the optical system can be obtained from the lens formula and Fig. 16. Let

$x_1 \triangleq dx_1'$ = the object virtual position, relative to its nominal position x_1'

$x_0 \triangleq dx_0'$ = the lens position relative to x_0'

$x \triangleq dx'$ = the image position relative to x'

F = the lens focal length

Then

$$\frac{1}{x_1' - x_0'} + \frac{1}{F} = \frac{1}{x' - x_0'} \tag{17}$$

and

$$dx' = \frac{\partial x'}{\partial x_0'} \, dx_0' + \frac{\partial x'}{\partial x_1'} \, dx_1' \tag{18}$$

The partial derivatives are easily evaluated.

From Eq. 17

$$F = \frac{(x' - x_0')(x_1' - x_0')}{(x_1' - x')} \tag{19}$$

Then

$$\frac{\partial x'}{\partial x_1'} = \frac{x_0' - x' + F}{x_1' - x_0' + F} = \frac{(x' - x_0')^2}{(x_1' - x_0')^2} \triangleq M^2 \tag{20}$$

$$\frac{\partial x'}{\partial x_0'} = \frac{x' - 2x_0' + x_1'}{x_1' - x_0' + F} = \frac{x' - x_0' + x_1' - x_0'}{x_1' - x_0' + F} \tag{21}$$

The first partial derivative (Eq. 20) is simply the square of the lateral magnification of the image. The second partial becomes unity when $x_1' - x_0'$ becomes large (and $x' - x_0' \rightarrow F$).

The focus error estimator E then drives an inner loop consisting of an amplifier, motor, and tachometer. Thus, the lens velocity, $\dot{x}_0$, becomes nominally proportional to E, closing the outer loop. Let

L = torque produced by the motor

$\mathcal{J}$ = inertia of the entire mechanical system

$\mathcal{F}$ = friction

μ = inner-loop amplifier and motor gain

ϵ = inner-loop error signal

The mechanical system differential equation is

$$L = \ddot{x}_0 \mathcal{J} + \dot{x}_0 \mathcal{F} \tag{22}$$

where

$$L = \mu\epsilon \tag{23}$$

and

$$x \cong x_0 + M^2 x_1 \tag{24}$$

from (18), (20), and (21). For the stability analysis, we set x_1 to zero; then, from (16) and (24)

$$x_0 = x = \frac{E}{T_0} \tag{25}$$

while

$$\epsilon = -E - \dot{x}_0 \tag{26}$$

combining

$$-\mu T_0 x_0 - \mu \dot{x}_0 = \mathcal{J}\ddot{x}_0 + \mathcal{F}\dot{x}_0 \tag{27}$$

or

$$\ddot{x}_0 + \frac{\mathcal{F} + \mu}{\mathcal{J}} \dot{x}_0 + \frac{\mu T_0}{\mathcal{J}} x_0 = 0 \tag{28}$$

Then the loop natural frequency and damping are

$$\omega_n = \sqrt{\frac{\mu T_0}{\mathcal{J}}}, \quad \xi = \frac{\mathcal{F} + \mu}{2\sqrt{\mu \mathcal{J} T_0}} \cong \frac{1}{2}\sqrt{\frac{\mu}{\mathcal{J} T_0}} \tag{29}$$

For critical damping

$$T_{0_{max}} \cong \frac{\mu_{max}}{4\mathcal{J}} \tag{30}$$

If the system is heavily damped, it acts like a first-order system with a time constant of

$$\tau = \frac{2\xi}{\omega_n} = \frac{1}{T_0} \tag{31}$$

Thus, we have shown that the minimum loop time constant is determined by the maximum achievable amplifier gain (μ_{max}). Of course, μ is not unlimited; it is determined by elements of the inner (tach) loop that are not modeled above. Therefore, in order to determine μ_{max}, we model the inner loop more exactly, including amplifier phase shift and motor resistance.

The motor model is shown in Fig. 17a. The armature current, i, is proportional to motor torque, while the induced armature EMF, e, is proportional to armature angular velocity; thus, the applied armature voltage μe gives, from the Kirchoff loop equation,

$$\mu\epsilon = G_v \dot{x}_0 + G_L RL \tag{32}$$

where G_v and G_L are the motor constants of proportionality.

The tachometer loop can then be modified to include the effect of amplifier frequency response (or any other equivalent low-pass effect within the tachometer loop), as shown in Fig. 17b. We have added to the ideal amplifier a simple low-pass filter with a time constant τ_0. Using the alternative differential equation notation, we may write

$$\tau_0 \dot{\epsilon} + \epsilon = \epsilon_0 \tag{33}$$

We must also replace Eq. (26) by

$$\epsilon_0 = E - \dot{x}_0 \tag{34}$$

Differentiating (32) and (22) gives

$$\mu\dot{\epsilon} = G_v \ddot{x}_0 + G_L R\dot{L} \tag{35}$$

$$\dot{L} = \mathcal{J}\dddot{x}_0 + \mathcal{F}\ddot{x}_0 \tag{36}$$

Finally, setting E to zero to obtain the stability of the inner loop only, and combining Eqs. (22) and (32) through (36), gives

$$-\dot{x}_0 = \epsilon + \tau_0\dot{\epsilon} = \frac{G_v\dot{x}_0}{\mu} + \frac{G_L R}{\mu}\left(\ddot{x}_0\mathcal{G} + \dot{x}_0\mathcal{F}\right)$$

$$+ \frac{\tau_0}{\mu}\left[G_v\ddot{x}_0 + G_L R(\mathcal{G}\dddot{x}_0 + \mathcal{F}\ddot{x}_0)\right] \qquad (37)$$

Now let

$$\dot{x}_0 \triangleq v,\ \ddot{x}_0 = \dot{v},\ \dddot{x}_0 = \ddot{v}$$

Then

$$\left(\frac{\tau_0 G_L R\mathcal{G}}{\mu}\right)\ddot{v} + \left(\frac{G_L R}{\mu} + \frac{\tau_0 G_v}{\mu} + \frac{\tau_0 G_L R\mathcal{F}}{\mu}\right)\dot{v}$$

$$+ \left(\frac{G_v}{\mu} + \frac{G_L R\mathcal{F}}{\mu} + 1\right)v = 0 \qquad (38)$$

or

$$\ddot{v} + \frac{G_L R\mathcal{G} + \tau_0 G_v + \tau_0 G_L R\mathcal{F}}{\tau_0 G_L R\mathcal{G}}\dot{v} + \frac{G_v + G_L R\mathcal{F} + \mu}{\tau_0 G_L R\mathcal{G}}v = 0 \qquad (39)$$

Then

$$\omega_n = \sqrt{\frac{\mu + G_v + G_L R\mathcal{F}}{\tau_0 G_L R\mathcal{G}}} \qquad (40)$$

And

$$\xi = \frac{G_L R \mathcal{J} + \tau_0 G_v + \tau_0 G_L R \mathcal{F}}{2\sqrt{\tau_0 G_L R \mathcal{J}}\sqrt{\mu + G_v + G_L R \mathcal{F}}} \tag{41}$$

Thus, we can see that the inner loop can always be made critically damped by reducing τ_0. (Of course, the quantity $G_L R^*$ can be reduced; however, most servo motors have large $G_L R$; consequently, reducing τ_0 is required). In order to get order-of-magnitude results, we might make some assumptions as follows: let

$$\mathcal{F} \cong 0$$

$$G_v \cong 0$$

allowing

$$G_L R \triangleq 1$$

Then, setting $\xi = 1$ gives from Eq. (41)

$$\mu_{max} \cong \frac{\mathcal{J}}{4\tau_0} \tag{42}$$

---

*The quantity $G_L R \mathcal{J}/G_v$ is the motor time constant (if $\mathcal{J}$ is caused by the motor armature). Allowing $G_v \to 0$ is equivalent to allowing the motor time constant to be much larger than τ_0.

We may now use this result to evaluate the outer-loop (through the focus estimator in Fig. 15) performance. From Eqs. (42) and (30)

$$T_{0_{max}} \cong \frac{1}{16\tau_0} \tag{43}$$

and from Eq. (31)

$$\tau_{min} \cong 16\tau_0 \tag{44}$$

Thus, the minimum outer-loop response time is roughly an order of magnitude slower than the amplifier time constant. The implied setup procedure is to adjust the amplifier gain, μ, for critical inner-loop damping (by applying a square wave instead of E, and observing the tachometer output signal). Then, the outer loop can be reconnected, and the gain (T_{max}) adjusted for reasonable stability.

The models used in this chapter are admittedly crude. The purpose, however, is to obtain simple formulas for further analysis. Indeed the objective of the design of the servo system is to obtain first order behavior of the loop so that the estimator output (E) will become simply proportional to lens velocity ($\dot{x}_o$).

5
POINT-IMAGE ANALYSIS

In order to obtain the first-order behavior of the automatic focusing system, we must obtain a model for the focus estimator. Since the most important image type is the isolated point (it plays the predominant role in determining the average behavior of the system), we will begin with the strong point image.

5.1. STRONG POINT IMAGE

Because the radar system is generally hard-limited (at RF), the signal history will have constant amplitude across the signal plane aperture. Consider, then, a uniformly illuminated optical aperture of length D, and an illumination wavelength λ, containing a cylindrical lens of focal length F.

Then the resolution (ρ_0) at the processor output plane, when it is correctly focused is, from physical optics

$$\rho_0 = \frac{\lambda F}{D} \quad \text{(half power)} \tag{45}$$

When the image is out of focus, the width of the image can be obtained from geometrical optics

$$\rho(x) \cong \left| \frac{xD}{F} \right| = \left| \frac{x\lambda}{\rho_0} \right| \tag{46}$$

when the focus error (x) is as defined previously. The complete expression can be shown to be [8]

$$\rho(x) = \sqrt{\left(\frac{xD}{F}\right)^2 + \left(\frac{\lambda F}{D}\right)^2} \tag{47}$$

or

$$\rho(x) = \sqrt{\left(\frac{x\lambda}{\rho_0}\right)^2 + \rho_0^2} \tag{48}$$

The intensity of the image, $\Psi(x)$, is related to the illumination intensity I by

$$\Psi(x) = \frac{ID}{\rho(x)} \tag{49}$$

since the image width in the y (or track) direction only is a function of x.

The image is now scanned by the TV system, which converts image intensity to voltage, and the electrical signal is differentiated and then peak-detected, resulting in

$$\frac{d}{dy}\left[\frac{ID}{\rho(x)}\left(\text{rect}\,\frac{y}{\rho(x)} * \text{sinc}\,\frac{y}{\rho_0}\right)\right]\Bigg|_{\max} = \frac{ID}{\rho(x)\rho_0} \tag{50}$$

The difference between the signals obtained from the two sides of the image splitter [positions $(x + \delta)$ and $(x - \delta)$] is taken and integrated over the field of view. The result of the integration will obviously depend on the number of points in the field, the number of available cells in the field, and the storage in the peak detector. However, since these effects affect only the magnitude of the estimator output and not its x dependence, we will ignore them here (they are

discussed in Section 6), and combine them with the constants I and D into the target field parameter T_1. Then the estimation output, E, is

$$E(x, T_1) = \frac{T_1}{\rho_0} \left[\frac{1}{\rho(x - \delta)} - \frac{1}{\rho(x + \delta)} \right] \tag{51}$$

In order to get a rough idea of the shape of E(x), we can use the simple expression for ρ in Eq. (46)

$$E(x, T) \cong \frac{T_1}{\lambda} \left(\frac{1}{|x - \delta)|} - \frac{1}{|x + \delta|} \right) \tag{52}$$

Then, for $|x| < \delta$

$$E(x) \cong -\frac{T_1}{\lambda} \left(\frac{1}{x - \delta} + \frac{1}{x + \delta} \right) = -\frac{T_1}{\lambda} \frac{2x}{x^2 - \delta^2} \tag{53}$$

For $|x| << \delta$

$$E(x) \cong \frac{2T_1}{\lambda} \frac{x}{\delta^2} \tag{54}$$

For $x > \delta$

$$E \cong \frac{T_1}{\lambda} \frac{2\delta}{x^2 - \delta^2} \tag{55}$$

And for $x < -\delta$

$$E = -\frac{T_1}{\lambda} \frac{2\delta}{x^2 - \delta^2} \tag{56}$$

Equations (53) through (56) are plotted in Fig. 18. Of course, the plot is not valid at $|x| \cong \delta$ because of the approximation of Eq. (46).

We can obtain exact expressions for E by using Eq. (47) instead of (46); however, this results in a rather unwieldly expression for further analysis. Instead, we will use an approximation that is physically realistic, but which results in relatively simple results. Thus, we will assume that the minimum resolution (for the in-focus image) is determined by the television system rather than by diffraction as in Eq. (46). This assumption produces (instead of Eq. 47) the simpler expression

$$\rho(x) = \left| \frac{\lambda}{\rho_0} x \right| + \rho_0 \tag{57}$$

We obtain

$$E = \frac{T_1}{\lambda} \left(\frac{1}{|x - \delta| + \frac{\rho_0^2}{\lambda}} - \frac{1}{|x + \delta| + \frac{\rho_0^2}{\lambda}} \right) \tag{58}$$

For $|x| \leq \delta$

$$E = -\frac{T_1}{\lambda}\left(\frac{1}{x - \delta - \frac{\rho_0^2}{\lambda}} + \frac{1}{x + \delta + \frac{\rho_0^2}{\lambda}}\right)$$

$$= -\frac{T_1}{\lambda}\,\frac{2x}{x^2 - \left(\delta + \frac{\rho_0^2}{\lambda}\right)^2} \tag{59}$$

For $x \geq \delta$

$$E = \frac{2T_1}{\lambda}\,\frac{\delta}{\left(x + \frac{\rho_0^2}{\lambda}\right)^2 - \delta^2} \tag{60}$$

For $x \leq \delta$

$$E = -\frac{2T_1}{\lambda}\,\frac{\delta}{\left(x - \frac{\rho_0^2}{\lambda}\right)^2 - \delta^2} \tag{61}$$

Since these expressions are valid at $|x| = \delta$, we may evaluate the loop performance. From Eq. (26), we see that to the first order ($\epsilon \cong 0$), we have simply

$$E = -\dot{x}_0 \tag{62}$$

We would now like to determine the response time of the outer loop to large signals (when the loop is nonlinear). As an example, let us examine the case when the focus of the image is suddenly (perhaps deliberately) changed by a large amount, introducing a large initial x_0 (and x). We would like to calculate the time required to refocus the image to within the depth of field of correct focus.

Thus, let

$$x_0(t = 0-) = X$$

$$x_1(t) \equiv 0 \tag{63}$$

and the depth of field

$$x_0(t = t_X) = \frac{\rho_0^2}{\lambda} \tag{64}$$

Then, from Eqs. (24) and (62)

$$E(x_0) = -\dot{x}_0 \tag{65}$$

or

$$\frac{dx_0}{-E(x_0)} = dt$$

or

$$\int_{X}^{\rho_0^2/\lambda} \frac{dx_0}{-E(x_0)} = t_X \tag{66}$$

Using Eqs. (59) and (60) for E, we obtain

$$t_X = -\int_{X}^{\delta} \frac{\lambda}{2T_1\delta} \left[\left(x_0 + \frac{\rho_0^2}{\lambda}\right)^2 - \delta\right] dx_0$$

$$+ \int_{\delta}^{\rho_0^2/\lambda} \frac{\lambda}{2T_1} \left[\frac{x_0^2 - \left(\delta + \frac{\rho_0^2}{\lambda}\right)^2}{x_0}\right] dx_0 \tag{67}$$

$$t_X = -\frac{\lambda}{2T_1\delta}\left[\frac{x_0^3}{3} + \frac{2\rho_0^2}{\lambda}\frac{x_0^2}{2} - \delta^2 x\right]_X^{\delta}$$

$$+ \frac{\lambda}{2T_1}\left[\frac{x_0^2}{2} - \left(\delta + \frac{\rho_0^2}{\lambda}\right)^2 \ln x_0\right]_{\delta}^{\rho_0^2/\lambda}$$

$$t_X = \frac{\lambda}{2T_1}\left[\frac{\delta^2}{6} - \frac{\rho_0^2}{\lambda}\delta + \frac{\rho_0^4}{2\lambda^2} - \left(\delta + \frac{\rho_0^2}{\lambda}\right)^2 \ell n \frac{\rho_0^2}{\lambda\delta} + \frac{X^3}{3\delta} + \frac{\rho_0^2}{\lambda\delta} X^2 + \delta X\right] \tag{68}$$

The result is somewhat simpler if we restrict X. Thus, if $X < \delta$

$$t_X = \frac{\lambda}{2T_1}\int_X^{\rho_0^2/\lambda}\left[x_0 - \frac{\left(\delta + \frac{\rho_0^2}{\lambda}\right)^2}{x_0}\right] dx_0 \tag{69}$$

$$t_X = \frac{\lambda}{2T_1}\left[\frac{\rho_0^4}{2\lambda^2} - \frac{X^2}{2} - \left(\delta + \frac{\rho_0^2}{\lambda}\right)^2 \ell n \frac{\rho_0^2}{\lambda X}\right] \tag{70}$$

Further, if $X << \delta$, the system becomes linear and

$$t_X = -\frac{\lambda}{2T_1}\left(\delta + \frac{\rho_0^2}{\lambda}\right)^2 \ell n \frac{\rho_0^2}{\lambda X} \tag{71}$$

Even in the case of small initial error, the resulting expression is rather unwieldly. In addition, a point must be very strong to dominate the radar limiter, and points of this strength are rare in modern, highly dispersed, high-resolution systems. For this reason, we will also discuss the weak, isolated point image.

Before proceeding, however, we can draw a few conclusions from the above analysis. First, we note from Eq. (50) that the inclusion of the

differentiation does not affect the estimation function for this target. Also, the differentiator/peak detector system gives the same results as a differentiator/rms detection system, but the rms detector requires the differentiator. Second, a comparison of Eqs. (71), (70), and (68) shows that for small X, t_X is proportional to $\ell n\ X$. As X approaches δ, t_X becomes proportional to $(\ell n\ X) - X^2$, and the curve of t_X versus X becomes even flatter. However, once X exceeds δ, t_X becomes proportional to X^3, and the penalty in t_X of small increases in X is severe. These results are consistent with the S-shaped curve of Fig. 20.

5.2. WEAK POINT IMAGE

Because the dominant image class, the weak, isolated point, does not capture the radar limiter, it results in a signal history that is weighted by the radar antenna.

The radar antenna itself is usually weighted so that the antenna beam is smooth and well shaped (free of sidelobes and irregularities). A reasonably good approximation to the antenna pattern is the cosine function; hence, Eq. (49) is replaced by

$$\Psi(x,\ y) = \frac{ID}{\rho(x)}\ \cos\frac{y}{\rho(x)} \tag{72}$$

for $-\pi/2 < y/[\rho(x)] < \pi/2$; otherwise

$$\Psi(x,\ y) = 0$$

Following the same procedure, the differentiated and peak-detected signal is

$$\frac{d}{dy}\left[\frac{ID}{\rho(x)}\cos\frac{y}{\rho(x)}\right]\Bigg|_{max} = \frac{ID}{[\rho(x)]^2} \tag{73}$$

Again, including the constants in T_2, evaluating Eq. (73) at the two focal planes, and taking the difference gives

$$E = T_2\left\{\frac{1}{[\rho(x-\delta)]^2} - \frac{1}{[\rho(x+\delta)]^2}\right\} \tag{74}$$

We now use the exact expression for ρ in Eq. (48):

$$E = T_2\left[\frac{1}{\frac{\lambda^2}{\rho_0^2}(x-\delta)^2+\rho_0^2} - \frac{1}{\frac{\lambda^2}{\rho_0^2}(x+\delta)^2+\rho_0^2}\right] \tag{75}$$

$$= T_2\left[\frac{1}{\frac{\lambda^2}{\rho_0^2}x^2+\frac{\lambda^2}{\rho_0^2}\delta^2+\rho_0^2-\frac{2\delta\lambda^2}{\rho_0^2}x} - \frac{1}{\frac{\lambda^2}{\rho_0^2}x^2+\frac{\lambda^2}{\rho_0^2}\delta^2+\rho_0^2+\frac{2\delta\lambda^2}{\rho_0^2}x}\right] \tag{76}$$

$$= \frac{4T_2\delta\lambda^2}{\rho_0^2}\left\{\frac{x}{\left[\frac{\lambda^2}{\rho_0^2}(x^2+\delta^2)+\rho_0^2\right]^2 - \left[\frac{2\delta\lambda^2}{\rho_0^2}x\right]^2}\right\} \tag{77}$$

In order to check Eq. (77), we may take

$$x \ll \delta \tag{78}$$

and the separation of the focal plane (2δ) to be much greater than the depth of the field; i.e.,

$$\delta >> \frac{\rho_0^2}{\lambda} \quad \text{or} \quad \frac{\lambda\delta}{\rho_0} >> \rho_0 \quad \text{or} \quad \left(\frac{\lambda\delta}{\rho_0}\right)^2 >> \rho_0^2 \tag{79}$$

Equation (77) reduces to

$$E \cong \frac{4\rho_0^2 T_2 x}{\lambda^2 \delta^3} \tag{80}$$

Or, if instead of using Eq. (78), we take

$$x >> \delta \tag{81}$$

then Eq. (77) becomes

$$E \cong \frac{4\rho_0^2 T_2 \delta}{\lambda^2 x^3} \tag{82}$$

We may now calculate the system response time to a step error x, using the same procedure as for the strong point target.

From Eqs. (77) and (66)

$$t_X = \int_X^{\rho_0^2/\lambda} \frac{dx_0}{-E(x_0)} = \frac{1}{T_2} \int_X^{\rho_0^2/\lambda} \frac{\left(\frac{2\delta\lambda^2}{\rho_0^2} x_0\right)^2}{\frac{4\delta\lambda^2}{\rho_0^2} x_0} dx_0$$

$$- \frac{1}{T_2} \int_X^{\rho_0^2/\lambda} \frac{\left[\frac{\lambda^2}{\rho_0^2} x_0^2 + \left(\frac{\lambda^2}{\rho_0^2}\delta^2 + \rho_0^2\right)\right]^2}{\frac{4\delta\lambda^2}{\rho_0^2} x_0} dx_0 \qquad (83)$$

$$t_X = \frac{\delta\lambda^2}{T_2\rho_0^2} \left(\frac{\frac{\rho_0^4}{\lambda^2} - X^2}{2}\right) - \frac{1}{T_2} \left[\frac{\lambda^2}{4\rho_0^2\delta} \frac{\left(\frac{\rho_0^8}{\lambda^4} - X^4\right)}{4}\right.$$

$$\left. + \frac{2\left(\frac{\lambda^2\delta^2}{\rho_0^2} + \rho_0^2\right)}{4\delta} \frac{\left(\frac{\rho_0^4}{\lambda^2} - X^2\right)}{2} + \frac{\left(\frac{\lambda^2\delta^2}{\rho_0^2} + \rho_0^2\right)^2}{\frac{4\delta\lambda^2}{\rho_0^2}} \ell n \frac{\rho_0^2}{\lambda X}\right] \qquad (84)$$

$$t_X = \frac{\lambda^2}{2T_2\rho_0^2}\left[\delta\left(\frac{\rho_0^4}{\lambda^2} - X^2\right) - \frac{\left(\frac{\rho_0^8}{\lambda^4} - X^4\right)}{8\delta}\right]$$

$$- \frac{\frac{\lambda^2}{2}\delta^2 + \rho_0^2}{\frac{\rho_0}{4\delta T_2}}\left(\frac{\rho_0^4}{\lambda^2} - X^2\right) - \frac{\left(\frac{\lambda^2}{2}\delta^2 + \rho_0^2\right)^2\rho_0^2}{4\delta T_2\lambda^2}\ln\frac{\rho_0^2}{\lambda X} \qquad (85)$$

Again, to check Eq. (85), we make assumptions (78) and (79) and repeat, using Eq. (80) instead of (77):

$$t_X \cong -\int_X^{\rho_0^2/\lambda} \frac{\lambda^2\delta^2}{4\rho_0^2 T_2}\frac{dx_0}{x_0} = \frac{\lambda^2\delta^3}{4\rho_0^2 T_2}\ln\frac{\lambda X}{\frac{2}{\rho_0}} \qquad X << \delta \qquad (86)$$

which is the last (third) quantity in Eq. (85).

Actually, assumption (79) is far less restrictive than it might seem. It will be shown in the next section that the optimum value of δ is on the order of the average error in focus, which is usually many times larger than the depth of field. Hence, we may simplify (85) with only a small loss of generality:

$$t_X \cong \frac{\lambda^2}{2T_2\rho_0^2}\left(\frac{X^4}{8\delta} - \delta X^2\right) + \frac{\lambda^2\delta^2}{4\rho_0^2\delta T_2}X^2 + \frac{\lambda^2\delta^3}{4\rho_0^2 T_2}\ln\frac{X\lambda}{\frac{2}{\rho_0}} \qquad (87)$$

or

$$t_X \cong \frac{\lambda^2}{4T_2\rho_0^2}\left(\frac{X^4}{4\delta} - \delta X^2 + \delta^3 \ln \frac{X\lambda}{\rho_0^2}\right) \tag{88}$$

Before proceeding, a few comments on the above discussion are in order. First, Eq. (73) shows that for the weak point, both the differentiator and the peak detector perform a valuable function. An rms detector (after averaging is performed across the field of view), would not respond at all to changes in focus (i.e., an increase in ρ). The use of a differentiator and rms detector would result in a $1/\rho$ relationship, as would a peak detector alone, while a combination of the two results in a $1/\rho^2$ relationship. Second, Eq. (88) shows that for small X, t_X varies with ℓn X (as before); however, for X larger than δ, t_X varies with X^4 (rather than with X^3 as before); hence, the system is not as responsive to large focus errors. Third, the quantity $\lambda\delta/\rho_0^2$ is the number of depths of field separating the image planes. Comparing Eq. (88) with Eq. (71) shows that the response time (for small X) is increased by this quantity. However, for $X \cong \delta$, the response time is improved if the number of depths of field is not too large (since the estimator E is more sensitive at $X \cong \delta$). Further comparison will be deferred to the next section.

6
PARAMETRIC DESIGN FOR DOMINANT IMAGE

With the background presented in the previous sections, we are now in a position, by specifying system performance, to determine the focal plane separation δ.

From Eq. (88), we can see that decreasing δ causes a much larger decrease in the system response time for small focus errors; hence, δ should be made as small as possible. On the other hand, when x approaches or exceeds δ, the response time increases with decreasing δ. Thus, δ should be decreased only to the extent that the probability of x exceeding δ remains small. Otherwise, the chances that loop lock will be lost becomes excessive.

The simplified loop configuration is shown in Fig. 19. The focus error of the virtual image (x_1) is corrected by moving the cylindrical lens a distance x_0, which causes the corrected image to appear a distance x from the image film. The distance x is sensed by the estimator discussed in the previous sections, resulting in the output E, a nonlinear function of x. This signal drives the inner (tachometer) loop, which is represented as an integrator. The objective is to choose the outer loop parameters to minimize x for a given x_1.

Thus far, x_1 has been considered to be the focus error of a single point. Actually (see the introductory discussion), the optical processor has a field of view (of dimension D_{x0} in track, D_{y0} in range) within which many points may be present at any given time. Then x_1 should be considered to be an average focus error of all points in the field.

In addition, each point image will have an individual focus error which is itself an average of the position error of the radar system over the synthetic aperture used to generate that image. (Image focus is the coefficient of the second-order term of the power series expansion of the radar system position error).

We might expect that the system position error would be normally distributed, but even if it is not, the double averaging will assure us that the focus error x_1 will be normally distributed. Hence, we will assume Gaussian statistics for x_1, and call the standard focus error (i.e., the standard deviation of x_1) σ. Also, the decorrelation time (ζ) will be on the order of the amount of time required for a single target to move through the field of view (as determined by the averaging process over the field) plus the aperture time. The bandwidth of x_1 is, then, roughly $1/\zeta$.

The function of the system is, of course, to reduce σ. Thus, it is reasonable to expect that the standard focus error of x is a small fraction of σ. Under these conditions, a reasonable approach is to assume that E(x) will be restricted to its linear range for average (σ) deviation of x_1. We may therefore write, from Eq. (80)

$$E(x) \cong \frac{4\rho_0^2}{\lambda^2} \frac{T_2}{\delta^3} x \tag{89}$$

Whereas from Fig. 21

$$E(x) = \dot{x}_0 \tag{90}$$

In order to perform a Fourier analysis, we let $x_o(t) = e^{j\omega t}$. Then

$$E(x) = j\omega x_0 \tag{91}$$

$$x_1 - x_0 = x \quad \text{or} \quad x_0 = x_1 - x \tag{92}$$

Combining (89), (91), and (92) gives

$$\frac{4\rho_0^2}{\lambda^2}\frac{T_2}{\delta^3}x = j\omega(x_1 - x)$$

Then the gain is

$$\frac{\dfrac{j\omega}{\dfrac{4\rho_0^2 T_2}{\lambda^2\delta^3} + j\omega}}{} x_1 = x \tag{93}$$

We will now specify that for input (x_1) errors of amplitude σ, the output (x) error must be reduced to remain within the depth of field of the image

$$x = \frac{\rho_0^2}{\lambda} \qquad \text{when } x_1 = \sigma \tag{94}$$

If the frequency of the disturbance is low

$$\omega << \frac{4\rho_0^2 T_2}{\lambda^2\delta^3} \tag{95}$$

whereas from the previous discussion

$$\omega = \frac{2\pi}{\zeta} \tag{96}$$

Then from (93, (94), (95), and (96)

$$\pi\lambda^2\delta^3\sigma = 2\rho_0^2 T_2 \frac{\rho_0^2}{\lambda} \tag{97}$$

or

$$T_2 = \frac{\pi\lambda^3\sigma\delta^3}{2\rho_0^2\zeta} \tag{98}$$

We wish now to replace T by the maximum stable loop gain $T_{0_{max}}$ calculated in Section 4. However, we must remember that the definition of T_0 included the gain of the estimator, whereas T_2 does not. Hence we set

$$T_{0_{max}} = \frac{4\rho_0^2 T_2}{\lambda^2\delta^3} \tag{99}$$

but from Eq. (43)

$$T_{0_{max}} \cong \frac{1}{16\tau_0} \tag{100}$$

Then, substituting into (98) gives

$$\frac{\pi\lambda^3\sigma\delta^3}{2\rho_0^4\zeta} = \frac{\lambda^2\delta^3 T_{0_{max}}}{4\rho_0^2} = \frac{\lambda^2\delta^3}{64\rho_0^2\tau_0} \tag{101}$$

or

$$\frac{\sigma\lambda}{\rho_0^2} = \frac{\zeta}{32\pi\tau_0} \tag{102}$$

The final step is to calculate δ. Since the primary effect of changes in δ is to change the distribution of x, one way to specify δ is to limit the spread (from normal) of the x distribution. A reasonable specification, then, might be

$$\text{when } x_1 = 3\sigma, \quad x = \frac{6\rho_0^2}{\lambda} \tag{103}$$

We note, however, that for large excursions, E is no longer a linear function of x. Furthermore, x_1 will reach 3σ only rarely. Hence, we will consider this set of circumstances as a transient set and use the nonlinear response time t_X developed in the previous section. From Eqs. (88) and (103), we have

$$\zeta \geq t_X = \frac{\lambda^2}{4T_2\rho_0^2} \left[\frac{(3\sigma)^4}{4\delta} + \delta^3 \ln \frac{3\sigma\lambda}{6\rho_0^2} \right] \tag{104}$$

Then, substituting (98)

$$\zeta \geq \frac{\lambda^2}{4\rho_0^2} \frac{2\rho_0^4\zeta}{\pi\lambda^3\sigma\delta^3} \left[\frac{(3\sigma)^4}{4\delta} + \delta^3 \ln \frac{3\sigma\lambda}{6\rho_0^2} \right] \tag{105}$$

$$1 \geq \frac{\rho_0^2}{2\pi\lambda\sigma\delta^3}\left[\frac{(3\sigma)^4}{4\delta} + \delta^3 \ln\frac{3\sigma\lambda}{6\rho_0^2}\right] \tag{106}$$

$$\delta^4 \geq \frac{20\sigma^4}{\frac{2\pi\sigma\lambda}{\rho_0^2} - \ln\frac{\sigma\lambda}{2\rho_0^2}} \tag{107}$$

Eq. (107) actually gives the minimum value of δ (larger values give less spread of x); however, the results of the next section show that the minimum should always be used.

In summary, Eq. (107) allows a calculation of δ, given the radar and processor parameters, and the standard focus error in the data. Then Eq. (98) can be employed to calculate the outer-loop gain. Meanwhile, Eq. (102) is used to calculate the required inner-loop time constant, τ_0, in order for the system to perform stably.

7
DISTRIBUTED IMAGES

In the preceding section, we have derived design equations based upon the average performance of the automatic focusing system on the average (point-target) field. In addition, however, it is necessary to insure that the focusing loop remains stably locked when the point-target field gives way to a distributed-target field. Distributed targets cover a wide range of image types from featureless desert terrain or open water to suburban areas with some open fields but a scattering of isolated trees, tree rows, fences, and roads. Since focus estimation is accomplished with varying difficulty depending on the distributed image type, it will be necessary for us to choose the particular type for which the automatic focusing system is to lock up marginally. The user of the system may wish to choose any of the foregoing distributed image types, but we will illustrate the design procedures with the farmland image. Thus, we will not assume that roads and other isolated targets are present; however, there will be reasonable variations in radar cross section in the farmland image because of differences in crops or moisture content of the soil. The justification for the use of this image type is that farmland is important to programs dealing with remote sensing of earth resources.

We will begin our discussion with some general statements about the nature of the radar image of a distributed object. Consider first, an area of infinite size and of constant radar backscatter coefficient (e.g., a large corn field). The usual radar scattering assumption is that the return corresponding to the image amplitude in any given resolution cell is composed of contributions from many scatterers located within that resolution cell (for example, the coherent sum of the returns from each corn stalk in the resolution cell). The further assumption is made that the phases of the components are uniformly distributed across all possible phase angles and that the amplitudes of the

contributions are distributed with a Rayleigh distribution. We first find the distribution of image intensity.* Let $\psi_0(y, z)$ = the image amplitude in resolution cell y, z. Then

$$\psi_0 = R_e \sum_1^n a_k e^{j\phi_k} \tag{108}$$

where n = number of independent scatterers in cell

a_k = amplitude of each scatterer

ϕ_k = phase of each scatterer

If the amplitudes are Rayleigh-distributed, the density is

$$p(a_k) = \frac{a_k}{u^2} e^{-a^2/2u^2} \qquad a_k \geq 0 \tag{109}$$

and ϕ_k is uniformly distributed and independent of a_k:

$$p(\phi_k) = \frac{1}{2\pi} \qquad 0 \leq \phi_k < 2\pi \tag{110}$$

while the joint density is

$$\begin{aligned} p(a_k, \phi_k) &= p(a_k)p(\phi_k) \\ &= \frac{1}{2\pi} \frac{a_k}{u^2} e^{-a_k^2/2u^2} \qquad \begin{matrix} a_k > 0 \\ 0 \leq \phi < 2\pi \end{matrix} \end{aligned} \tag{111}$$

*Solutions to the inverse problem can be found in the literature [9].

Now let

$$\psi_k = \mathcal{R}_e \left\{ a_k e^{j\phi_k} \right\} = a_k \cos \phi_k$$

$$\psi_k' = \mathcal{I}_m \left\{ a_k e^{j\phi_k} \right\} = a_k \sin \phi_k \qquad (112)$$

or

$$a_k = \sqrt{\psi_k^2 + \psi_k'^2}\,; \qquad \phi_k = \tan^{-1} \frac{\psi_k'}{\psi_k}$$

We can find the density function of ψ_k, using the Jacobian of the transformation (J):

$$p(\psi_k, \psi_k') = \frac{p_{a_k \phi_k}(\psi_k, \psi_k')}{\left| J(a_k, \phi_k) \right|} \qquad (113)$$

where J can be found from Eq. (112) to be

$$\left| J \right| = \left(\psi_k^2 + \psi_k'^2 \right)^{-1/2} \qquad (114)$$

Then

$$p(\psi_k, \psi_k') = \frac{1}{\sqrt{2\pi}\,u} e^{-\psi_k^2/2u^2} \frac{1}{\sqrt{2\pi}\,u} e^{-\psi_k'^2/2u^2} \qquad (115)$$

Therefore, ψ_k and ψ_k' are independent and Gaussian:

$$p(\psi_k) = \frac{1}{\sqrt{2\pi}\,u} e^{-\psi_k^2/2u^2} \tag{116}$$

By Eq. (108), ψ_0 is the sum of independent Gaussian components and is therefore Gaussian, regardless of n.

The assumption that a_k is Rayleigh is usually reasonable. However, if a_k has some other distribution, the central limit theorem can be used with Eq. (108) to show that for large n, ψ_0 will be Gaussian anyway, and the convergence will probably be rapid.

Because the image intensity Ψ_0 is proportional to the square of the amplitude

$$\Psi_0 = \psi_0^2 \tag{117}$$

the distribution of Ψ_0 may be found [10]:

$$\psi_0 = \Psi_0^{1/2}, \qquad \frac{d\psi_0}{d\Psi_0} = \frac{1}{2}\Psi_0^{-1/2}$$

$$p(\Psi_0) = \frac{1}{u\sqrt{2\pi\Psi_0}} e^{-\Psi_0/2u^2} \tag{118}$$

Hence, the distribution of Ψ_0 is chi-square.

The procedure we will use on distributed objects is noncoherent integration. This process has been described heuristically in Section 2, and is basically a resolution-spoiling procedure [11, 12, 13]. Normally, it is performed only in the focus estimation part of the loop, by deliberate setting of the resolution of the TV camera to be coarser than the coherent image formed by the optical processor and recorded on the image film.

Since large amounts of resolution spoiling can be performed in the range (z) direction without compromising the ability of the autofocus system to find an exact focus in azimuth (y), integration in range (N_z) is preferred. Some additional integration in azimuth (N_y) may also be performed if required. Expressions for N_z will be found in Section 3, Equation (13). The total noncoherent integration performed is N

$$N = N_y N_z \tag{119}$$

The image intensity in a given (coarse) resolution cell becomes the sum of N independent samples of the fine-resolution image:

$$\Psi_0 = \sum_{i=1}^{N} \Psi_{0i} \tag{120}$$

where the density function of Ψ_{0i} is given in Eq. (118). Thus, the density function for Ψ_0 can be found by determining the characteristic function for the Ψ_{0i}, raising to the N-th power, and finding the inverse. Since Ψ_{0i} is chi-square, the results may be obtained from the literature [11].

$$p(\Psi_0) = \frac{1}{\Gamma\left(\frac{N}{2}\right) 2^{N/2}} \Psi_0^{\left(\frac{N}{2}-1\right)} e^{-\Psi_0/2} \qquad (121)$$

$$\text{mean} = N, \qquad \text{standard deviation} = \sqrt{2N}$$

Thus, the distribution is again chi-square but with N degrees of freedom. The distribution for the first few values of N are shown in Fig. 20. The figure shows that after $N \cong 3$, the distribution has become bell-shaped and is approaching Gaussian, with a mean of N, and a standard deviation of $\sqrt{2N}$. Thus the "signal"-to-"noise" ratio, as shown in Fig. 9a, is improving with $\sqrt{N}$. The "signal" is defined as the mean value of the image. The "noise" is the coherent breakup and is measured by the standard deviation of the image intensity from the mean.

Treatment of noncoherent integration is complicated by the fact that the noise is not additive; i.e., if a different kind of terrain (with a different signal strength) is imaged, the noise will also have a different strength. In fact, the signal-to-noise ratio measured at any arbitrary point on an image of real terrain will be constant and independent of the signal strength at that point, and is always $\sqrt{N/2}$.

As an illustration of one potential procedure, consider the image shown in Fig. 21a. It consists of an area of distributed return of width W bounded by areas of little (or no) return. This image might represent the grass divider between airport runways or lanes of an expressway, or perhaps a grove of trees.

We can consider the image to be composed of signal and noise components (see Fig. 21b) of approximately equal energy. The abruptness of the focused image edge is equal to the resolution ρ_0.

Thus, the spectrum of the image has two components. The signal spectrum is the product of the spectrum of the rectangular pulse multiplied by the impulse response of the system (ρ_0). (The signal is the convolution of the rectangular pulse with the impulse response.) Thus, the signal spectrum is the sinc^2 function of bandwidth $1/W$, weighted by the system frequency response. If the power density at a frequency equal to $1/\rho_0$ only is of interest, the system frequency response at $1/\rho_0$ is $1/2$, and the spectrum of the signal at $1/\rho_0$ is

$$\frac{1}{2}\left(\frac{\rho_0}{W}\right)^2 \tag{122}$$

relative to its peak.

The noise component has a spectrum of bandwidth $1/\rho_0$. Since the energy in the image noise (for N = 1) is $\sqrt{2}$ times the signal energy, and two times the signal energy after the television transducer (recall that the TV output voltage is proportional to the image intensity), the noise level at frequency $1/\rho_0$ is

$$2 \times \frac{1}{2} \times \frac{\rho_0}{W} \tag{123}$$

Hence, the signal-to-noise ratio at $1/\rho_0$ is

$$\frac{\rho_0}{2W} \qquad \text{for N = 1} \tag{124}$$

When the noncoherent integration (in the z direction) is performed, the image of Fig. 21c is obtained. Similar reasoning leads to a signal-to-noise ratio at $1/\rho_0$ of

$$\frac{N\rho_0}{2W} \tag{125}$$

Defocusing of the image leads to a reduction of signal strength at frequency $1/\rho_0$, with no accompanying change in the noise. Hence, for the focus estimator to work at all, we must begin with a reasonably large signal-to-noise ratio from Eq. (125). Thus, if a bandpass filter/energy detector system were used, large amounts of noncoherent integration would be required, on the order of the ratio of the "average" distributed object width to resolution. Before proceeding further, however, we will refine the target model to determine the criteria to be used for selecting "average width."

The farmland image can be represented as a set of contiguous distributed areas, each with a constant, average, backscatter coefficient and signal strength over the area, but with varying signal strength between areas. Such an image is shown in Fig. 22. The signal strength can take on a wide range of values (e.g., smooth soil and trees can differ by 20 to 30 db in backscatter coefficient at X-band). We will therefore assume only that $\bar{\Psi}_0$ has some (unspecified) probability distribution $p(\bar{\Psi}_0)$.

Since the spectrum of the signal is the Fourier transform of the autocorrelation function ($\mathcal{R}$), by definition,

$$\mathcal{R}(y_1, y_2) = \mathcal{E}\left[\bar{\Psi}_0(y_1)\bar{\Psi}_0(y_2)\right] \tag{126}$$

where $\mathcal{E}$ is the expectation value.

Eq. (126) can be subdivided into two cases; for the first, there are no changes in Ψ_0 in the interval y_1, y_2, and for the second, there are transitions:

$$R(y_1, y_2) = \mathcal{E}\left\{\mathcal{E}\left[\bar{\Psi}_0(y_1)\bar{\Psi}_0(y_2)\right]\Big|_{\text{no transitions}} + \mathcal{E}\left[\bar{\Psi}_0(y_1)\bar{\Psi}_0(y_2)\Big|_{\text{transitions}}\right]\right\} \tag{127}$$

If the values of $\bar{\Psi}_0$ are uncorrelated across the transition, the second term of (127) is the mean square value of $\bar{\Psi}_0$ multiplied by the probability of one or more transition. The first term is the expectation value of $\bar{\Psi}_0^2$ multiplied by the probability of no transitions:

$$R(y_1, y_2) = (s^2 + m^2)\nu(y_1 - y_2) + m^2\left[1 - \nu(y_1 - y_2)\right]$$

$$= s^2\nu(y_1 - y_2) + m^2 \tag{128}$$

where $\nu(y_1 - y_2)$ = probability of no transition on $y_1 - y_2$
m = mean value of $\bar{\Psi}_0$
s^2 = variance of $\bar{\Psi}_0$

Since we are interested in the ac components of the spectrum (the transform of R) we can drop the m^2 term; the spectrum now depends only on the transition probability and the variance of $\bar{\Psi}_0$, not on its distribution function.

It is necessary to assume a particular function for ν. Since experimental data are not readily available, we will have to make two assumptions: (1) there are more small farms than large, but (2) the probability that farm size is zero is zero.

One function that meets these assumptions is the Poisson:

$$\nu(y_1 - y_2) = e^{-(y_1-y_2)/W} \tag{129}$$

We note that

$$\nu(y_1 - y_2) = 1 - P(y_1 - y_2)$$

and

$$\frac{d}{d(y_1 - y_2)} P(y_1 - y_2) = p(y_1 - y_2) \tag{130}$$

where $p(y_1 - y_2)$ = probability-density function of farm size $(y_1 - y_2)$
$P(y_1 - y_2)$ = distribution function
W = the average farm size

Using (128) and (129), we can determine the spectrum of the signal. If we ignore the dc component, the transform is well known

$$\frac{2s^2}{W\omega^2 + \frac{1}{W^2}} \tag{131}$$

Thus, we are led to the same result (Eq. 122) obtained from the single field for the power density at the frequency $1/\rho_0$

$$\frac{1}{2}\left(\frac{\rho_0}{W}\right)^2 \tag{132}$$

Also, we can use the same procedure with the noise component; the average noise power after noncoherent integration is obtained from the dc part of (128) and (121)

$$\frac{2m^2}{N} \tag{133}$$

and the power spectral density at $1/\rho_0$ is

$$\frac{\rho_0 m^2}{N} \tag{134}$$

The signal-to-noise ratio at $1/\rho_0$ is, from Eqs. (134) and (131)

$$\frac{2Ns^2\rho_0}{m^2W} \tag{135}$$

Equation (135) is the electrical signal-to-noise power ratio that would be obtained from an rms detector following a bandpass filter, with the image in correct focus. The system configuration actually in use consists of a differentiator, a lowpass filter (the effect of the TV system resolution), and a peak detector. The differentiator/lowpass filter has almost the same transfer function as a single-pole bandpass filter of low Q. However, for simple images (e.g., images described in Section 5), differentiation of the image is straightforward and gives reliable results, and evaluation of the peak detector output is also simple.

The farmland signal described in this section is somewhat unwieldly to analyze in the time domain by direct differentiation, and temporal treatment of the noise component is considerably more difficult; thus, we will use the frequency domain result of Eq. (135) with only minor modification.

Direct differentiation of the signal component of Fig. 24 can be performed quickly to verify the signal part of (135). The average

transition height is still s^2, and the differentiation produces a pulse of energy $s^2\rho_0$ for each transition. One transition is obtained in each interval of approximately W width; hence, the average signal power from an rms detector is $\frac{s^2\rho_0}{W}$. The average noise power was obtained in (133), and the ratio of the two is

$$\frac{s^2\rho_0 N}{W2m^2} \tag{136}$$

which is in qualitative agreement with Eq. (135).

Even though the treatment leading to (136) is not very accurate, we now have an obvious method for analyzing the peak detector. If we define the ratio of detector decay time constant (Fig. 12) to the pulsewidth obtained from a resolution cell (ρ_0) as the quantity η, the signal energy per transition is increased by the factor 1.4η over the output of the rms detector (for $\eta\rho_0 << W$). The response of the detector to the noise is also increased, since the detector tends to respond to the noise peaks, rather than to rms, but even in the limit ($\eta \to \infty$), the noise output power is increased by a factor of only four. However, for more typical values of η (e.g., 10), noise power is increased by only about 50%. Hence, the modification of (136) and (135) for a peak detector is accomplished by multiplying by η:

$$\frac{2\eta N s^2\rho_0}{m^2 W} \tag{137}$$

Further integration (after the detector) does not affect (137), since signal and noise are attenuated equally.

We now must determine the required signal-to-noise ratio for stable loop operation. The difference between the two detector outputs (corresponding to the two focal planes) are found, as described in Section 5, to form an error function E. As far as the signal component of (137) is concerned, the development pursued in Section 5, "Weak Point Image," applies directly; hence, the shape of the signal component of the error function is the same as Eqs. (77), (80) and (82). The noise component is, of course, unaffected by defocusing (x), and taking the difference of two independent random variables causes an increase (rms addition) of the noise level. Thus, the smooth error function of Eq. (77) is added to the noise, resulting in an error function similar to that shown in Fig. 23.

An indicator of loop performance is the step response time constant. The response time for recovery to within the depth of field has been derived in Eq. (66) for an arbitrary initial focus error, X:

$$t_X = \int_X^{\rho_0^2/\lambda} \frac{dx}{-E(x)} \tag{138}$$

Also, the rate of recovery, $\dot{x}$, is proportional to E, as in Eq. (62). Thus, if E is allowed to approach zero, Eq. (138) blows up, and the loop stalls. As long as the signal component of E remains large compared to the noise (as, for example, near $x = \pm\delta$ in Fig. 23), the average value of $\dot{x}$ will be almost independent of noise, but when the signal-to-noise ratio approaches unity, a drastic change in loop behavior occurs.

The noise component of E is a function of both focus and time:

$$E = E(x, t)$$

Thus, if the image is held stationary (i.e., the signal film is stationary), E becomes a function of focus alone, with a decorrelation distance equal to the depth of field; if focus is fixed instead, E(t) has similar statistics, but has a decorrelation time equal to the time that the field of view is approximately constant. Hence, the loop will never stall completely, even for very small signal-to-noise ratios, but the noise will "dither" the focus, the average value of which will approach zero slowly, as the scene changes. In practice, small bias errors in the equipment will easily negate the weak tendency of the loop to settle in regions where E crosses zero. These biases will invariably cause the loop to run away if an attempt is made to operate in the large-focus-error regions where E crosses zero.

We will specify that sufficient noncoherent integration be performed so that the region around $x = 0$, over which E will be allowed to cross zero, will be equal to K times the depth of field (ρ_0^2/λ). This specification is rather stringent when $K = 1$, since the result is that the autofocus system performs almost as well for farmland as it does for point objects, and since it insures that the farmland image focus is held within the depth of field.

We will reference the noise level of Eq. (137) to unity; then Eq. (137) becomes the signal level before differencing at $\rho(x) = \rho_0$. We can now combine with Eq. (74) to recalculate T_2:

$$\sqrt{\frac{2\eta N s^2 \rho_0}{m^2 W}} = \frac{T_2}{(\rho_0)^2} \tag{139}$$

or

$$T_2^2 = \frac{2\eta N s^2 \rho_0^5}{m^2 W} \tag{140}$$

Then, from Eq. (80), the normalized E after differencing is

$$E = \frac{4s\rho_0^{9/2}}{m\lambda^2\delta^3} \sqrt{\frac{2\eta N}{W}}\, x \tag{141}$$

After differencing, the noise is increased to 1.4 units. Setting E to 1.4 and x to $K\rho_0^2/\lambda$ allows us to solve for the required N:

$$N = \frac{1}{16\eta K^2} \frac{W}{\rho_0} \frac{m^2}{s^2} \left(\frac{\lambda\delta}{\rho_0^2}\right)^6 \tag{142}$$

The strong dependence of N on the ratio of δ to the depth of field justifies the statements made at the end of Section 6; δ must be kept to the absolute minimum.

8
INTERMEDIATE IMAGE TYPES

In the previous two sections, we have concentrated on the extremes of potential target types. In Sections 5 and 6, the single isolated point scatterer was used as a basis to determine the dominant loop behavior. In Section 7, the discontinuous distributed image was used to determine the loop behavior under marginal conditions. Loss of focus lock would be avoided only through large amounts of noncoherent integration. In between these two extremes, however, lie a range of target types which are still fairly common. The purpose of this section, then, is to discuss these target types in order to verify that the behavior of the loop will not be radically altered by their presence in the image. Also, in the course of the discussion, it will be shown that the particular combination of estimators chosen for the automatic focusing system is at least reasonably efficient for each of the intermediate classes of targets. In particular, the target classes to be discussed in this section are the very weak point targets in Gaussian clutter, the two-point targets, the infinite periodic array of point targets, and the non-Gaussian distributed target.

We will begin the discussion with a consideration of the point targets immersed in a distributed target background. We will assume that the point target is only slightly stronger than the background. As stated in the discussion in Section 7, the basic distribution of the image intensity for the distributed background is chi-square. When a modest amount of noncoherent integration is performed, however, the distribution tends to become symmetrical with a mean equal to N times the average value of the original distribution and with a variance which diminishes relative to the mean as the noncoherent integration is increased. In fact, as the integration is increased, the distribution converges to the normal distribution. The differentiation also has a property of making the distribution symmetrical and for a uniform, average-intensity,

distributed target background, of reducing the mean to zero. Therefore, it will be assumed for this discussion that the output of the differentiator in the presence of the distributed target background is normally distributed with zero mean.

The behavior of the point target was described in Section 5 where it was shown that the output of the differentiator diminishes in peak amplitude inversely with the square of the width of the target. Hence, the energy at the output of the differentiator diminishes rapidly as the width of the point target increases, i.e., as the point target is defocused. However, for the distributed target field, the energy at the output of the differentiator is independent of focus. We will now define a very weak point target in a distributed background as follows: a target field composed of very weak point targets is one in which the total electrical energy of the point targets (after the TV transducer) is equal to or less than the total energy of the distributed background field.

With this definition, a focus estimator derived purely on the basis of the output energy from the differentiator will be useless, since even when the field is in correct focus, the output energy from the differentiator will be approximately that caused by the distributed target background only, which does not change with focus. Thus, the behavior of the automatic focusing system will depend strongly on the peak detector time constant (see Fig. 11). The average power output from the peak detector is shown in Fig. 24 as a function of image focus. The ratio of maximum to minimum power is equal to approximately the product of the ratio of the energy in the point targets to the distributed target background and the number of resolution cells stored in the peak detector. This approximation will hold true as long as the peak intensity of the point targets is somewhat greater than the peak intensity of the distributed target background.

The width of the curve in Fig. 24 is determined by the attenuation of the point targets by the differentiator. If, for example, it had been

possible to use no differentiator (peak detection only), the ratio of X_{max} to the depth of field would be equal to the ratio of the minimum to maximum power of Fig. 24. Since the differentiator is needed to deal with discontinued distributed targets described in Section 7, the useful width of the detector output power function of Fig. 27 is reduced to

$$\frac{X_{max}}{X_0} = \sqrt{\frac{P_{max}}{P_{min}}} = \sqrt{\eta Q} \tag{143}$$

where η is the peak detector storage, Q is the ratio of point target to distributed target (electrical) energy, and X_0 is the depth of field of the image. Thus, the differentiator causes a deterioration in performance over the pure peak detector by limiting the amount of focus error that can be accommodated. On the other hand, as long as the focus error is kept within these limits, the presence of the differentiator will increase the amount of error signal (E) appearing at the output of the estimator and thus will result in a tighter feedback loop.

We now turn our attention to the more complex target situation, the category called groups. Although some general statements may be made about the performance of the system in the presence of groups of targets, considerable insight may be gained by examining a few simple specific examples of groups of targets.

We will therefore begin by considering the case of two isolated point targets. The target pair has been described briefly in the introduction (Section 1), and the appearance and the spectrum of the image were shown in Fig. 5. We will now examine in a little greater detail how the coherent addition of the two defocused signals shown in Fig. 5 influences the output of the focus estimator.

In Fig. 25, we have shown the geometrical optics approximation for a pair of equal amplitude targets separated by the distance 2w. When the two images are sufficiently out of focus, the images will overlap and interfere coherently to produce the beat pattern shown in Fig. 5. In Fig. 26b, we have drawn in somewhat greater detail, the appearance of the image for the two domains of interest; that is, for the overlapping and nonoverlapping situations. The beat frequency is greatest when the two targets begin to overlap, and the frequency at this point is equal to the bandwidth of the correctly focused point target as determined from physical optics. In the nonoverlapping domain, the bandwidth of the point target decreases inversely with x (the distance of the image plane from the true focal point); likewise, in the second domain, the frequency of the beat decreases inversely with x.

In the first (nonoverlapping) domain, the peak detector output has been shown to be (Eq. 73)

$$\frac{ID}{[\rho(x)]^2} \qquad \rho(x) < 2w \tag{144}$$

In the second domain, the beat frequency is

$$\frac{2\pi}{\lambda}\frac{w}{x} \tag{145}$$

and, therefore, the peak detector output is

$$\frac{ID}{\rho(x)}\frac{2\pi}{\lambda}\frac{w}{x} \qquad \rho(x) > 2w \tag{146}$$

In both cases, $\rho(x)$ is the width of each target in the pair, where (as in Eq. 46), from geometrical optics

$$\rho(x) = \left| \frac{x\lambda}{\rho_0} \right| \tag{147}$$

Thus, in both cases, the detector output is inversely proportional to x^2. The ratio between (144) and (146) is

$$\frac{2\pi w}{\rho_0} \tag{148}$$

The curves are sketched in Fig. 26. The doubling back at the transition between the domains may be undesirable because it may result in a false lock point in the loop (if δ is small).

In order to gain further understanding of how the system responds to more complicated groups of targets, we might consider target configurations of three or four targets of equal or varying amplitudes. However, we expect these target configurations to result in detector output curves which have multiple peaks of various amplitudes and spacings from the main peak. We will establish the limit by giving as an example the infinite array of equal-amplitude, equally spaced point targets.

The target field is illustrated in Fig. 28. Fortunately, this target field bears close resemblance to a grating, which is a well studied object in the field of coherent optics. In fact, the image of the point-target array in the vicinity of focus has been demonstrated to repeat at regularly spaced intervals along the optic axis (detailed discussion of

the image of a repeating structure will be found in Ref. 15). Thus, as the image is slowly defocused, the point-target array will appear to blur and, with further defocusing, will begin to sharpen again; this process will repeat through many cycles. The resulting detector output signal as a function of focus is shown in Fig. 29; this curve will be recognized as the extreme example of the doubling back that is observed in Figs. 26 and 27. Of course, since the image repeats, there is no scheme that will distinguish the true focal position from the ambiguous ones. Furthermore, noncoherent integration similar to that described in Section 7 will have no effect on this problem.

By now it should be apparent that the intermediate group of targets described in this section actually cover a wide range of performance. We would hope to find some way of studying the average intermediate target type without being forced to resort to specific examples that represent the extreme in either one direction or the other. We will, therefore, conclude this section with a discussion of the non-Gaussian target group distribution.

Given an arbitrary image in correct focus, we may find the defocused image by application of the Rayleigh Sommerfeld diffraction formula [16]

$$\psi(x,\ y) = \frac{1}{j\lambda} \int_{\psi_0} \frac{\exp\left(j \frac{2\pi}{\lambda} h\right)}{h} \psi_0(0,\ y_0)\, dy_0 \qquad (149)$$

where ψ_0 = the infocus image at x = 0

ψ = the defocused image at position x

$h = \sqrt{x^2 + (y - y_0)^2}$

Let us now consider the case in which the image ψ_0 is not known explicitly but is a random function with a known but non-Gaussian,

amplitude distribution function. In this case, the image intensity of the defocused image ψ, evaluated at a particular position, X and Y, is given in Eq. (149) as the summation of contributions across the image ψ_0, with each phase shifted by an amount equal to the distance between the contributing element in the focused image and the point in the unfocused image receiving the contribution. Thus, the amplitude at each point on the defocused image may be considered to be the sum of a number of independent samples of the in-focus image distribution ψ_0. It can be seen from geometrical optics (Fig. 30) that the number of elements in the sum will increase as the image is defocused.

We may now apply the equal moments case of the central limit theorem and conclude that if the defocusing is made large enough, the amplitude distribution of the defocused image will approach the normal distribution. Of course, the convergence will depend upon the distribution of the in-focus image and for certain images (for example, the infinite array of point targets described in the previous section), the convergence may be very slow indeed. However, in most cases, the target distribution will be a few point targets in a cluster surrounded by more or less Gaussian clutter, and the convergence will be quite rapid.

To proceed beyond this point requires that the statistics of the derivative of the distribution of ψ be determined. Since the distribution of the function and the distribution of its derivative are generally independent, some knowledge of the function ψ_0 is probably required, and the previous examples given in this section will have to suffice. However, if the differentiator were not present, and the image distribution were highly dispersed, the peak detector output signal would be a reasonable estimator of focus of the image, since the dispersion of the distribution has been shown to decrease as the image is defocused.

9
SUMMARY AND EXPERIMENTAL RESULTS

In the previous sections, we have developed design equations to allow selection of critical system parameters. Given the standard focus error (σ) and the processor depth of field (ρ_0^2/λ), the image separation was shown to be

$$\delta^4 = \frac{20\sigma^4}{\frac{2\pi\sigma\lambda}{\rho_0^2} - \ell n \frac{\sigma\lambda}{2\rho_0^2}} \tag{107}$$

where the minimum value should be used.

Given the processor field-of-view exposure time (ζ), the required servo motor amplifier time constant was

$$\tau_0 = \frac{\zeta}{32\pi} \frac{\rho_0^2}{\sigma\lambda} \tag{102}$$

The estimator gain (T_2), with a field dominated by point targets, can also be set

$$T_2 = \frac{\pi\lambda^3\sigma\delta^3}{2\rho_0^4\zeta} \tag{98}$$

If sufficient noncoherent integration can be performed, the autofocus loop will remain in lock on distributed targets. As an example, if it is desirable for the system to hold focus within K depths of field on a farmland image, the required integration (N) for a peak-detector-normalized decay of η resolution cells is

$$N = \frac{1}{16\eta K^2} \frac{W}{\rho_0} \frac{m^2}{s^2} \left(\frac{\lambda\delta}{\rho_0^2} \right)^6 \tag{142}$$

where W/ρ_0 is the average farm size (in resolution cells), and m^2/s^2 is the mean-square-to-variance ratio of farmland radar cross section.

The optical system can now be designed from the equations developed in Section 3. In most cases, the optical processor and the TV system field of view and resolution will be set in advance, and the autofocus optical system must be designed to match. Thus, we are given D_{y0}, D_{z0}, D_4, ρ_0, and ρ_4. In addition, we are free to choose one more parameter, usually a comfortable f/number for the autofocus sphere (f_c). Then, the sphere focal length (F_3) and aperture (D_3) are

$$F_3 = D_{z0} f_c \tag{11}$$

$$D_3 = D_{z0}$$

The range cylinder is

$$F_2 = \frac{D_{z0}^2 f_c}{D_4}$$

$$D_2 = D_{z0}$$

The azimuth cylinder focal length and apertures are

$$F_1 = \frac{D_{z0} f_c \rho_0}{\rho_4}$$

$$D_{z_1} = D_{z0} \tag{11}$$

$$D_{y_1} = 3D_{y0} + \frac{F_1}{f_{y0}}$$

where f_{y0} is the f/number of the optical processor.

Thus, the amount of noncoherent integration obtained in range is

$$N_z = \frac{\rho_4}{\rho_0} \quad \frac{D_{z0}}{D_4} \tag{13}$$

If this amount does not equal N calculated from (142), η should be adjusted (or the TV resolution should be reduced by defocusing the TV camera).

The image splitter angle (θ) and the separation (Δ) can be obtained from

$$\theta = \tan^{-1} \frac{D_{y0}}{\delta} \tag{15b}$$

$$\Delta = \frac{2D_{y0} \cos \theta}{\sin 2\theta} \tag{15a}$$

An experimental system has been set up; the design parameters for the system are described below.

The standard focus error of the data was measured to be about five depths of field

$$\frac{\sigma\lambda}{\rho_0^2} = 5$$

The optical processor field of view was

$$D_{z0} = 70 \text{ mm}$$

$$D_{y0} = 1 \text{ mm}$$

The output image f/number and depth of field were

$$f_{y0} = 30$$

$$\lambda = 6320 \text{ Å}$$

$$\lambda f_{y0}^2 = \frac{\rho_0^2}{\lambda} = 0.5 \text{ mm}$$

$$\rho_0 = 0.018 \text{ mm}$$

Using Eqs. (107), (15), and (16) we can calculate

$$\delta = 2.5 \text{ mm}, \quad \theta = 22^\circ, \quad \Delta = 2.6 \text{ mm}$$

The TV camera had a photosensitive surface 25 mm in diameter and 0.2-mm working resolution

$$D_4 = 25 \text{ mm}$$

$$\rho_4 = 0.2 \text{ mm}$$

The largest sphere that was easily obtainable was f/2.5; hence, from Eq. (11)

$$F_3 = 135 \text{ mm} \qquad D_3 = 70 \text{ mm}$$

$$F_2 = 490 \text{ mm} \qquad D_2 = 70 \text{ mm}$$

$$F_1 = 15 \text{ mm} \qquad D_{z1} = 70 \text{ mm}$$

$$D_{y1} = 3.5 \text{ mm}$$

Then from Eq. (13)

$$N_z = 31$$

An additional factor of four could be obtained from the radar data in azimuth over the design resolution

$$N_y = 4$$

$$N = N_y N_z = 124$$

In order to perform effective proximity weighting, the peak detector storage was set to about half the azimuth field of view

$$\eta = 28$$

There are very few experimental data about the radar cross section of terrain. However, Ref. [17] indicates that the high-resolution probability-density function is log-normal with a ratio

between the mean cross section and the standard deviation of about 5 to 6 db. Thus

$$\left(\frac{s}{m}\right)^2 = (4)^2 = 16$$

The average width of the farmland which was frequently encountered locally was measured at about 200 resolution cells

$$\frac{W}{\rho_0} = 200$$

Inserting these values in Eq. (142) and solving for K gives

$$K^2 = 3.3 \qquad K = 1.8$$

Thus, focus will hold within two depths of field for farmland.

The experimental equipment block diagram is shown in Figs. 10, 11, and 15. The optical portions of the equipment are detailed in Figs. 13 and 14.

The mechanical design of the structure supporting the optics emphasized optical stability without sacrificing convenience in installing and removing the autofocus equipment from the SAR optical processors. This was done because a large part of the processing performed on the WRL equipment is of small areas over which focus is generally constant and autofocus is not required; however, when processing of large quantities of data is required, the prealigned autofocus can be quickly installed. In addition, the design was constrained to fit in the few inches of space available between the final glass surface of the moving cylindrical telescope and the processor camera.

Figure 31 is a photograph of the autofocus system, including the processor camera, but with the motor driven telescope removed from the processor. The insert of Fig. 31 shows the autofocus optics more clearly by removing the camera. In actual operation, the arm holding the pellicle beam splitter, image splitter and tilted cylinder fits snugly between the telescope and the camera. These optical elements are mounted to have mechanical adjustment in all significant directions. All these adjustments are performed with setscrews except for tilt of the autofocus azimuth cylinder. The tilt adjustment is sometimes required when a new signal film is processed (it is equal to the camera tilt and is made by a control knob).

The autofocus sphere and range cylinder are mounted directly on the television camera, which, together with the aforementioned optics mounting arm, is permanently fastened to a portable optical rail. Thus the entire autofocus system can be rolled away from the SAR processor rail. The television camera control unit (which includes the focus estimation circuitry), the television monitor and the servo motor amplifier are located in the electronics rack.

The initial adjustment of the optical system involves element alignment to produce two identical (except for focus) images of the same field of view observed by the camera. Each image must be uniformly focused across the field, and geometrical distortion must be small so that all targets that appear in one image also appear in the other. Obtaining adequate image quality and fidelity was in fact the major practical problem to be solved during the course of the experiments. Final selection of the image field is made by positioning the electronic horizontal and vertical gates generated by a timing and control module. The gates are displayed on the television monitor (by slightly increasing the picture brightness).

The focus estimator circuitry was constructed on a printed circuit card which was inserted in a spare socket in the TV camera control unit. (The timing and control card is inserted in a second spare). The video is obtained from the camera video amplifier, passed through a LC single pole bandpass filter, amplified, detected, gated and monitored as shown in Figs. 10 and 11. These functions are implemented using commercially available integrated circuit components. The servo components shown in Figs. 10 and 15 (the adder and motor amplifier) are constructed on a separate chassis not visible in Fig. 31. The moving cylindrical telescope slides on precision ball bearing rails, and is driven by a 24 V, 3 amp DC servo motor/tachometer with a built-in planetary gear reduction head. The reduction unit drives a leadscrew knife edge system that moves the lens. Limit switches prevent mechanical jamming by reversing the motor armature polarity.

During the course of the experiments several samples of SAR signal film were processed using the autofocus equipment. One (fairly typical) image that was used to evaluate performance contains all the major target and terrain types; a large lake, open countryside, a builtup area (including some moving objects), and is bounded on one side by open water (no signals). Two image films were produced; one manually (fixed) focused to some "best" average, and one automatically focused. Figure 32 shows an extreme enlargement of an area of particularly poor focus in the manual image, and the same area in the automatic image. The resolution is obviously greatly improved in the latter.

The most significant achievement, however, is that the automatic system was able to maintain focus lock over the entire image. In fact, if the system was prefocused to the "best" average manual focus, the processing could be started anywhere along the image (including in the no signal area in the water), and the focusing system quickly obtained

focus lock. In contrast, the previous experimental efforts were able to maintain lock only over the central (cultural) part of the image, where there are many point targets; however, the point targets did provide an excellent estimation of focus and results similar to Fig. 30 were obtained previously.

Figure 31 shows the resolution improvement obtained from the automatic system (in the cultural part of the image only). It also illustrates the difficulty of obtaining quantitative measurements of resolution from an image of an unknown target field.

The data reduction procedure was as follows: First, the image was divided into vertical strips, each the width of the camera (image plane) slit. Since the autofocus system averages the focus across the slit, it is expected that there will be little change in processor focus across each strip. Second, from each strip, a set of "point" targets is chosen. Of course there is no assurance that the chosen targets are actually smaller than the radar resolution, and, in fact, as will be seen from the data, many of the "points" were actually substantially distributed. Next the null to null widths of the individual targets were measured on the automatically focused and manually focused images. These widths are plotted in the lower half of Fig. 31. Finally, the width of each automatically focused target is subtracted from the width of its manually focused mate. The average difference and spread of differences for each strip is plotted in the upper half of Fig. 31, along with the distribution of differences for the entire data set. The difference is taken because some of the targets are distributed, and width ratios would therefore vary from target to target. However, width differences should be constant, and consistency of the differences within each strip is an indication of the accuracy of the width measurements and the adequacy of the chosen target.

Several conclusions can be drawn from the data of Fig. 33:

1) The average minimum width of any of the chosen targets in either image was about 0.2 unit null to null; thus 0.1 unit can be considered the practical 3 db resolution capability of the SAR system.

2) The average width difference is positive for all but one strip, and all the differences were positive in 75% of the strips; thus, the automatic system generally improves focus.

3) In one strip the automatic system degraded average focus by about 3 resolution cells. This was probably because this strip happened to be in correct focus in the fixed focus image. Further, the accuracy of measurement in the strip was poor, probably because of the absence of strong points.

4) The greatest improvement measured was 1 1/2 units or 15 resolution cells.

5) The accuracy of measurement is generally rather poor; hence, some misinterpretation of the statistical results of Fig. 31 is probably unavoidable. Specifically, the attempt to generate very accurate statistics by measuring large numbers of points is thwarted when the extra points are not real targets. We conclude that resolution measurements outside the cultural area would be meaningless.

As stated previously, the data shown in Figs. 32 and 33 contained all the major target and terrain types, and the fact that focus lock was maintained over the entire strip implies that some sort of an error signal was obtainable from all these targets. However, in order to separate the effects of the various targets so that independent evaluation of the performance of the system to each type could be made, additional experimental data was obtained.

The experimental procedure was as follows. First, an area of terrain containing one particular target type was located, and the film was held stationary with the target of interest centered in the field of view of the autofocus system. When possible an area was chosen that was adjacent to isolated point targets, and these were used as a control for the experiment. However, in those cases the point target image was not allowed to enter the autofocus equipment, but was blocked off either optically, or electronically, by adjusting the durations of the gate signals that demultiplex the data. Then (without moving the data film) the optical processor cylindrical lens was manually defocussed with the autofocus servo loop open. The autofocus system was then connected and the smoothed estimator error voltage (which is also the drive voltage for the autofocus motor) was observed as the lens was allowed to move toward the correct focus position. The position of the lens was marked when the estimator error (and motor drive) voltage reached zero, and photographs were taken of both the image and the estimator error voltage.

Next, with the loop open again, the lens was manually positioned to obtain several degrees of defocus to both sides of the estimated (zero error) correct focal position. For each of these positions the estimator error voltage was again photographed. This procedure was continued to trace out the estimator transfer curve. Observation was continued until the estimator voltage dropped below the threshold of the autofocus system, in order to make sure that no spurious zero

crossings occurred within the S-shaped portion of the transfer curve. Finally, the processor lens was manually positioned to each of the two points corresponding to which the estimator error voltage absolute value was maximum. For each point, a photograph of the image was taken. These images are labeled respectively positive and negative limit.

Now, it will be noted, that in the absence of any other targets in the field of view, the autofocus system will actually pull in from any point on the transfer curve for which the absolute value of the error signal is correct. In other words, if no other signals interfere, as long as the estimator error voltage is positive, the lens will move in a negative direction and as long as it is negative, the lens will move in the positive direction to eventually obtain correct focus. However, when other signals are present, it is not reasonable to expect the autofocus system to actually pull in to focus from those regions beyond the peaks of the S-shaped transfer curve if the estimator output is weak. Hence, for practical (operational) purposes, the peaks of the transfer curve represent the limits of strong error signals and are the practical pull-in limits of the autofocus system for the more difficult targets.

In Fig. 34, we have illustrated the image of a complex group of targets. This particular area was selected because a strong point target was located in such a position that it would (if desired) enter the field of view of the autofocus system simultaneous with the group. The first step was to mask off the point target so that only the group was allowed to enter the autofocus, and to record the image corresponding to zero estimator error voltage. Then with the autofocus loop open (so that the lens remained in position) the autofocus field of view was expanded to include the point target and the photograph was made of the error voltage from the estimator.

The point at which the error signal was measured was the output of the summer shown in Fig. 10 (which is also the input to the motor

drive amplifier). It will be noted that the signal at this point has been demultiplexed by the two gates and averaged by the integrator system. The signal is shown in Fig. 35. In order to understand the wave shapes shown in the figure, we must realize that the integrators shown in Fig. 10 have a discharge time constant which is long compared to the fast horizontal sweep of the TV system but short compared to the slow vertical sweep of the TV system. Hence, the function of the integrator is only to smooth the signals sufficiently that at the end of each horizontal scan of the TV system the output of the summer will represent the estimated focus error. The averaging of the focus error in the range direction (from top to bottom in the photographs of the image) is performed by the motor, which cannot respond significantly to varying signals in the 18 millisecond period of the slow vertical sweep of the TV camera. However, because the integrator discharge time constant is relatively fast, compared with the vertical scan, we are able to separate the contributions to the total error signal from the point target and the group. Thus, in the photographs shown in Fig. 35, the pulse appearing to the left corresponds to the error signal from the point target alone. The pulse appearing to the right corresponds to the error signal from the group alone.

As stated previously, this procedure was repeated for various positions of the processor lens and the photographs of Fig. 35 correspond to the error signal for each of the positions of the lens chosen. As can be seen from the figure, the error signal was monitored over the major portion of the S-shaped transfer curve. In Fig. 36 we have plotted the average values of the estimator error voltage corresponding independently to the point target and the group. As can be seen from the figure, the two curves are not identical. Neither one is smooth and they do not cross the zero error voltage line at the same lens position. The amplitudes of the two curves, however, are approximately the same. We can therefore draw several conclusions.

First, the group would contribute as much to the overall error estimation as the point target would. Second, the focus estimation obtained from the group is somewhat different from the estimation obtained from the point target.

Which estimation then is more nearly correct? Careful examination of Fig. 34 shows that whereas the point target is clearly in better focus in the picture corresponding to the zero error signal from the group, the point target still appears to be somewhat out of focus. This is consistent with the zero crossing discrepancy of Fig. 36. Further examination of Fig. 34, however, will disclose a number of well isolated point scatterers located at the bottom of the image just outside of the autofocus field of view. These point scatterers are obviously quite accurately in focus in the center picture in spite of the fact that the large target which was at first thought to be a point is not in focus. Thus, we might say that even the point target is somewhat distributed and that the large group of complex targets actually gives a more accurate estimation of the focus than the so-called point. A possible explanation for this seemingly strange occurrence is that the large group of targets at the bottom of the figure actually contains a few very large dominating point scatterers, and that the peak detector is responding primarily to these scatterers.

Now that we have obtained the comparison of the point target and the group, we proceed to examine in greater depth the most difficult target types as far as autofocus is concerned. First, we examine the water land boundary.

Figure 37 illustrates a second area of terrain that was chosen for analysis. The figure shows a portion of the boundary of a large body of water. This particular area was chosen because the signal-to-noise ratio and image contrast of the original data was good and because the area was relatively clear of point targets and other complex target types. The field of view of the autofocus system is indicated

in the figure and includes both the near and far shore. The image appears as though one of the two boundaries is heavily wooded and the other is an open field. Thus, both a tree/water and grass/water boundary is contained. Unfortunately, in order to find an area that was relatively clear of other target types, it was necessary to go to an area which did not contain a point target for reference. However, as before, the appearance of the image was recorded for the point of zero error and for the point of maximum positive and maximum negative estimated error. The corresponding error signals are shown in Fig. 38.

We can conclude from Fig. 37 that the autofocus system seeks a better focus than that corresponding to either of the two pull-in limits. From Fig. 38 we can conclude that the error signal is indeed strong when the image is out of focus and is just as great as the error signal that was obtained from the point target or the group. Of course, the strength of the error signal for the land water boundary depends strongly not only on the nature of the target but also the contrast across the boundary, the orientation of the boundary, and the length of the boundary contained within the autofocus field of view.

Because the author was not sure that the uncontrolled land water boundary experiment presented in Figs. 37 and 38 was conclusive, an effort was made to set up an artificial experiment to simulate a land water boundary, upon which more conclusive data would be obtained. In order to do this, an area of imagery was located which contained an isolated point target in a relatively large expanse of uniform background. Again the image was positioned with the point target near the edge of the field of view of the autofocus system but this time a straight edge was set up in the optical processor to block off part of the uniformly distributed target image. An attempt was made to place the straight edge at a focal plane which corresponded to the focal plane of the point target, but which was located prior (in the

optical system) to the moving cylindrical lens that finally adjusts the focus of the processor. Then the autofocus field of view was adjusted to exclude the point target but include a large portion of the boundary.

The results of this test are illustrated in Figs. 39 and 40. Again, it is apparent that the zero error signal image is in much better focus than either image corresponding to the maximum absolute value of the error signal. However, we find we are again faced with a problem; careful examination of the in-focus picture in Fig. 39 reveals that the boundary is in better focus than the point target. The explanation for this is probably that the straight edge was not positioned in exactly the same location as the focal plane of the point target and since the autofocus system saw only the edge it came to a correct focus on the signal that it saw.

As a final experiment, data corresponding to the farmland image was collected and this data is presented in Figs. 41 and 42. Again, an area of terrain was selected on the basis of strong contrast in the boundary and the particular farm that was chosen was apparently surrounded by forest. Hence, the boundary that we consider here is the tree/field boundary. Once again the autofocus field of view was closed down to include only the farm indicated in Fig. 41. The in-focus image in Fig. 41 corresponds to the point at which the error signal was zero. The out of focus image corresponds to focal position of maximum positive error signal. Figure 42 shows the error signals corresponding to the in-focus image and the out-of-focus image shown in Fig. 41, and in addition, shows the error signal corresponding to the opposite polarity out-of-focus image which is not shown in Fig. 41. Again, the error signals are strong and the defocus is severe at the pull-in limits.

Conclusions

The data shown in Figs. 34 through 42 demonstrate that if the autofocus system is not presented with an error greater than the separation between the two focal planes in the autofocus equipment, an error signal will be developed that will tend to pull the system into focus. The question of whether the system will achieve focus in the time available during the exposure of the image (and in fact will remain in-lock over a continuous strip of imagery) will depend on how strong the error signal is. This, in turn, will depend on the extent of the boundary, or the strength of the group of targets, as well as the nature of the terrain. If, however, the focus error does not exceed the extremes of the pull-in limits, the system will stay in lock over the entire image. As described on page 85, the system is designed for a standard focus error of 5 depths of field, or 1/10 inch. The pull in limits for the distributed targets are about 1/4 inch or 2σ. If more serious focus errors are encountered in the data, the autofocus system may still remain in lock depending upon how smoothly the focus varies and how strong the error signals are from the terrain. However, the best way to obtain an estimate of the system performance in total is to perform the experiment described in Figs. 32 and 33. Since that experiment was also successful over just as wide a variety of terrain as was measured in detail in the later figures, we can be assured that the system will operate properly for all but the most extreme samples of combined severe focus errors and the lack of focusable targets.

During the course of the experimental efforts, certain practical and theoretical problems were encountered which were set aside as being tangential to the main issues involved, and it would be valuable if at some time in the future these issues were examined. The first and most significant of these was the previously unappreciated fact that as the focus of the image changes the tilt of the image plane (as far as a synthetic aperture radar processor is concerned) also changes.

The rotation of the image plane is in fact small. However, in the course of the experimental effort, several occasions were encountered in which the tilt was noticeable and could be seen in the estimator output signal. Specifically, several times it was noted that near range targets seemed to be giving a different focus estimate from far range targets at one place in the image, and at a different place in the image the reverse indication was obtained. This did not prevent the automatic system from maintaining focus lock on the average focus across the scene but did result in a less than optimally focused image. This problem could have been corrected quite simply by mechanically coupling the synthetic aperture radar camera that records the final image to the moving cylindrical lens. Thus, as the cylindrical lens moves to correct focus, the camera would be rotated to correct tilt.

A second difficulty that was encountered was the signal-to-noise ratio of the TV system. In fact, it was found that when the TV system was adjusted to properly respond to very bright point targets, the thermal noise output from the TV camera was much larger than desirable compared with the signals that were being obtained from the distributed and boundary type targets. A possible solution to this problem is the incorporation of an AGC in the TV system to adjust the beam voltage to correspond with the instantaneous appearance on the image. Thus, when strong point targets appear, the beam voltage would be high resulting in a poor signal-to-noise ratio; however, the estimator output would also be large corresponding to the domination of the point targets. In areas of terrain where there were no strong point targets, the beam voltage in the TV camera could be reduced and this would allow for less deterioration of performance in the more difficult target areas by the thermal noise originating in the TV system.

In summary, however, we can state that the autofocus concept presented in this dissertation was highly successful, since it could

hold focus lock across a wide variety of terrain.

In addition, in areas where focus could be measured quantitatively, resolution was improved by up to 15 resolution cells, but the accuracy of measurement is poor. However, the real value of the automatic system lies in the subjective opinion of the radar photo interpreters, who feel that image sharpness is improved significantly in all terrain types, and who are relieved from the tedious task of trying to manually track image focus over long strips of data.

APPENDIX — FIGURES

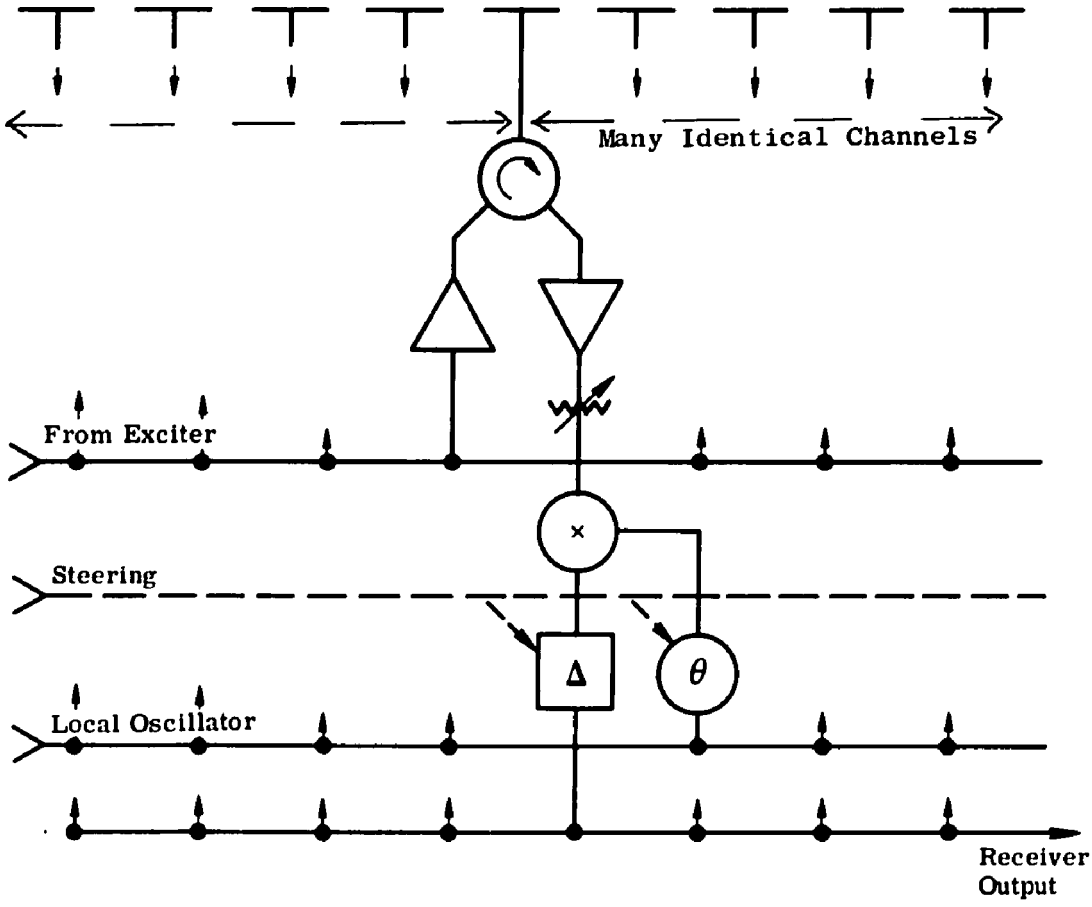
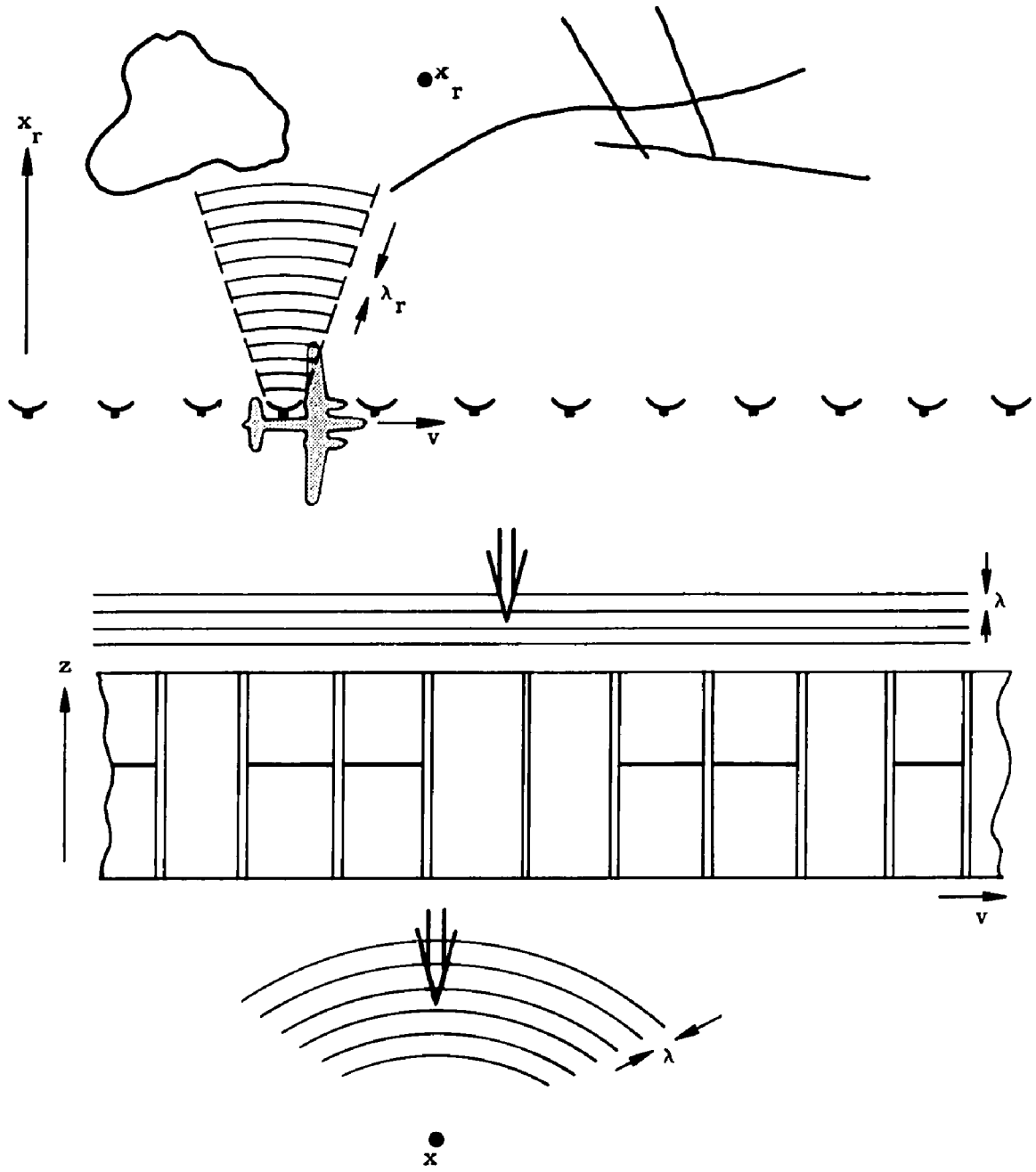


FIGURE 1. PHASED ARRAY



$$x = x_r \times \left(\frac{v}{v_r}\right)^2 \times \frac{\lambda_r}{\lambda} \times \frac{1}{2}$$

FIGURE 2. SYNTHETIC-ARRAY RADAR

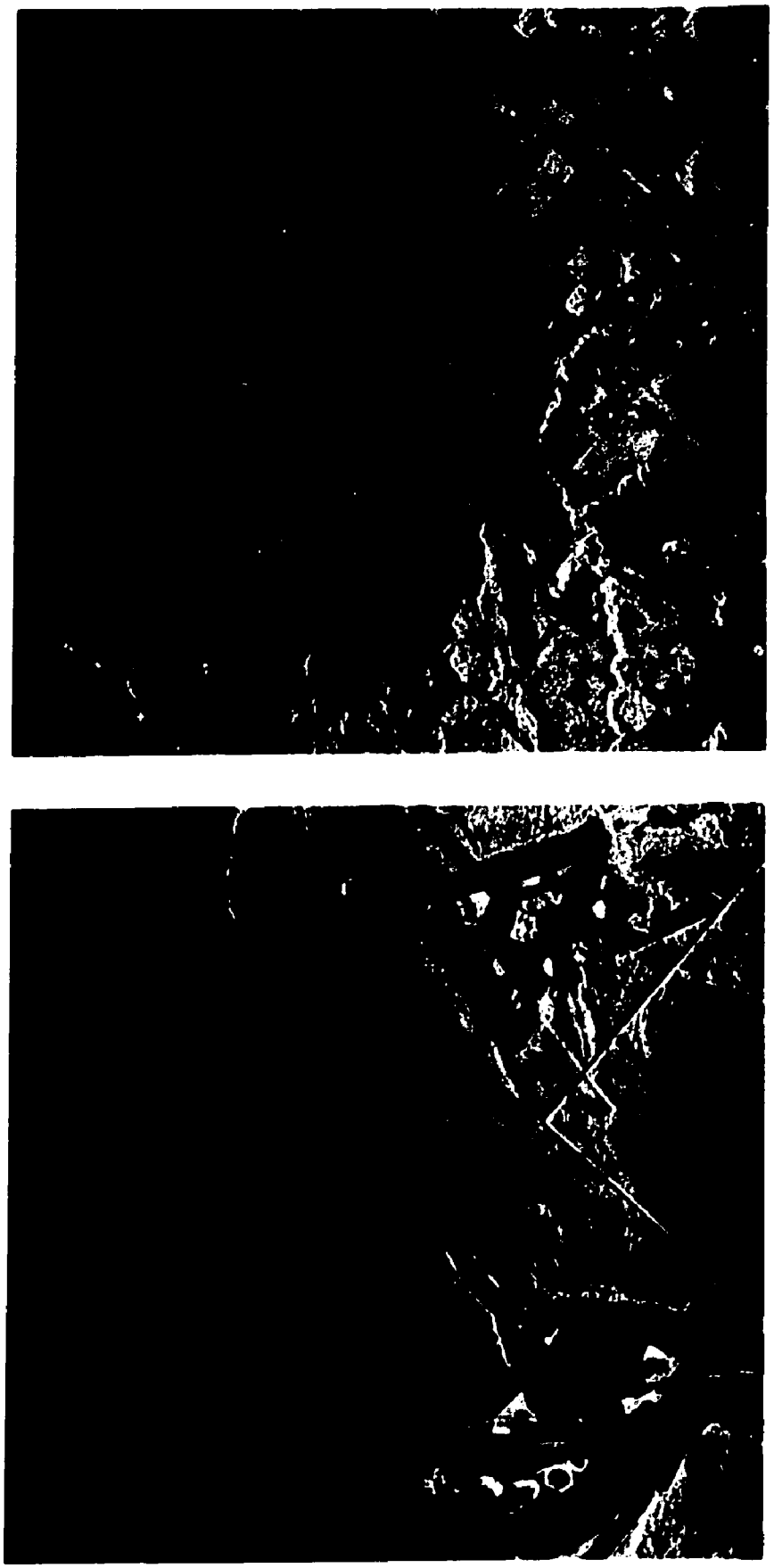


FIGURE 3. TYPICAL SAR IMAGERY

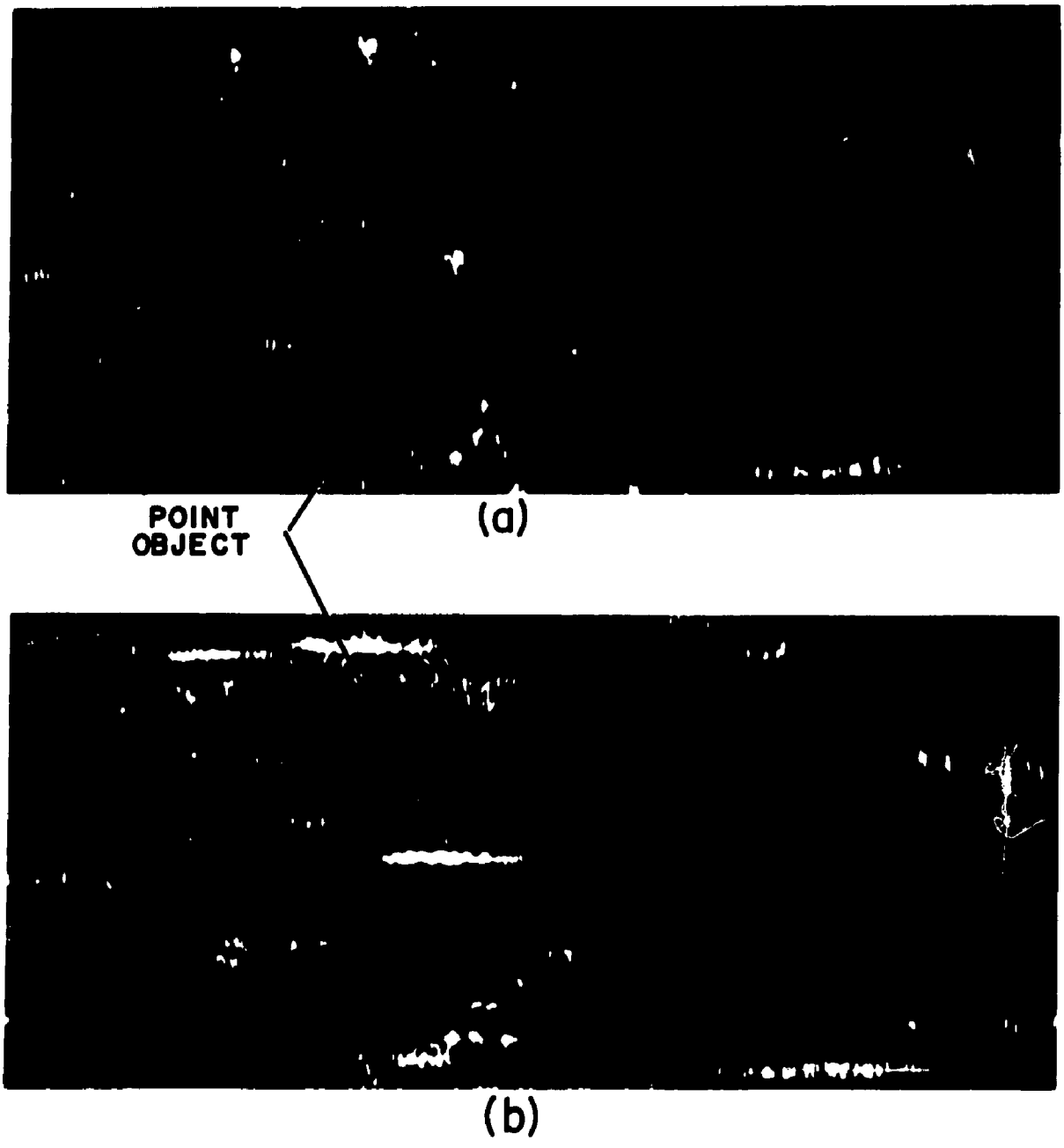


FIGURE 4. COHERENT IMAGERY ENLARGEMENTS

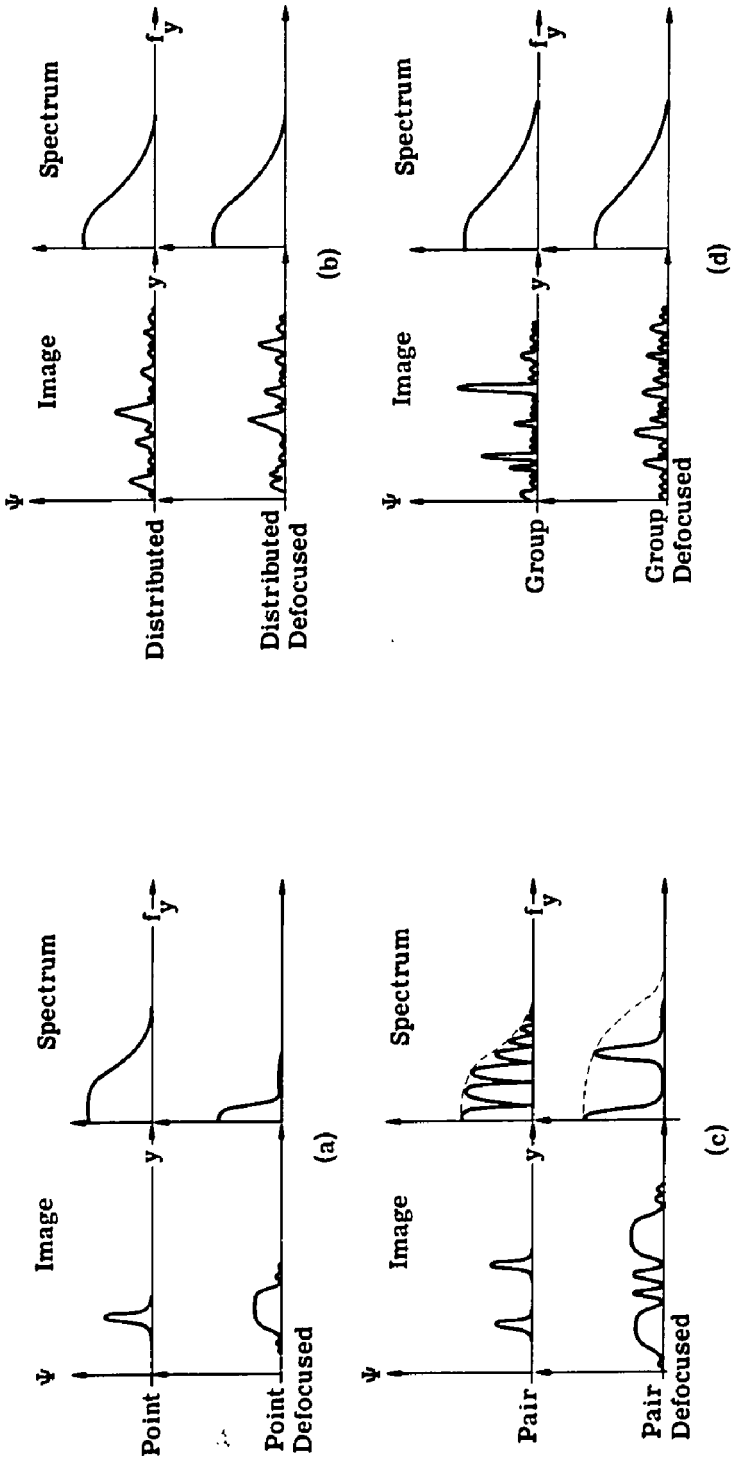


FIGURE 5. COHERENT IMAGE TYPES AND SPECTRA

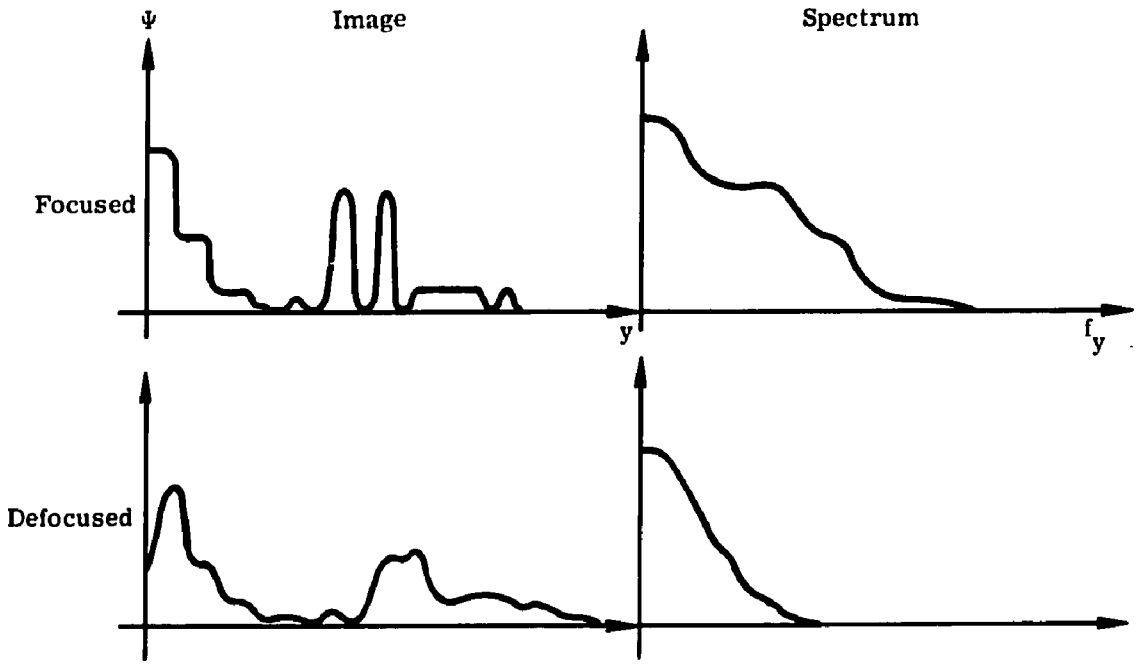


FIGURE 6. NONCOHERENT IMAGE AND SPECTRA

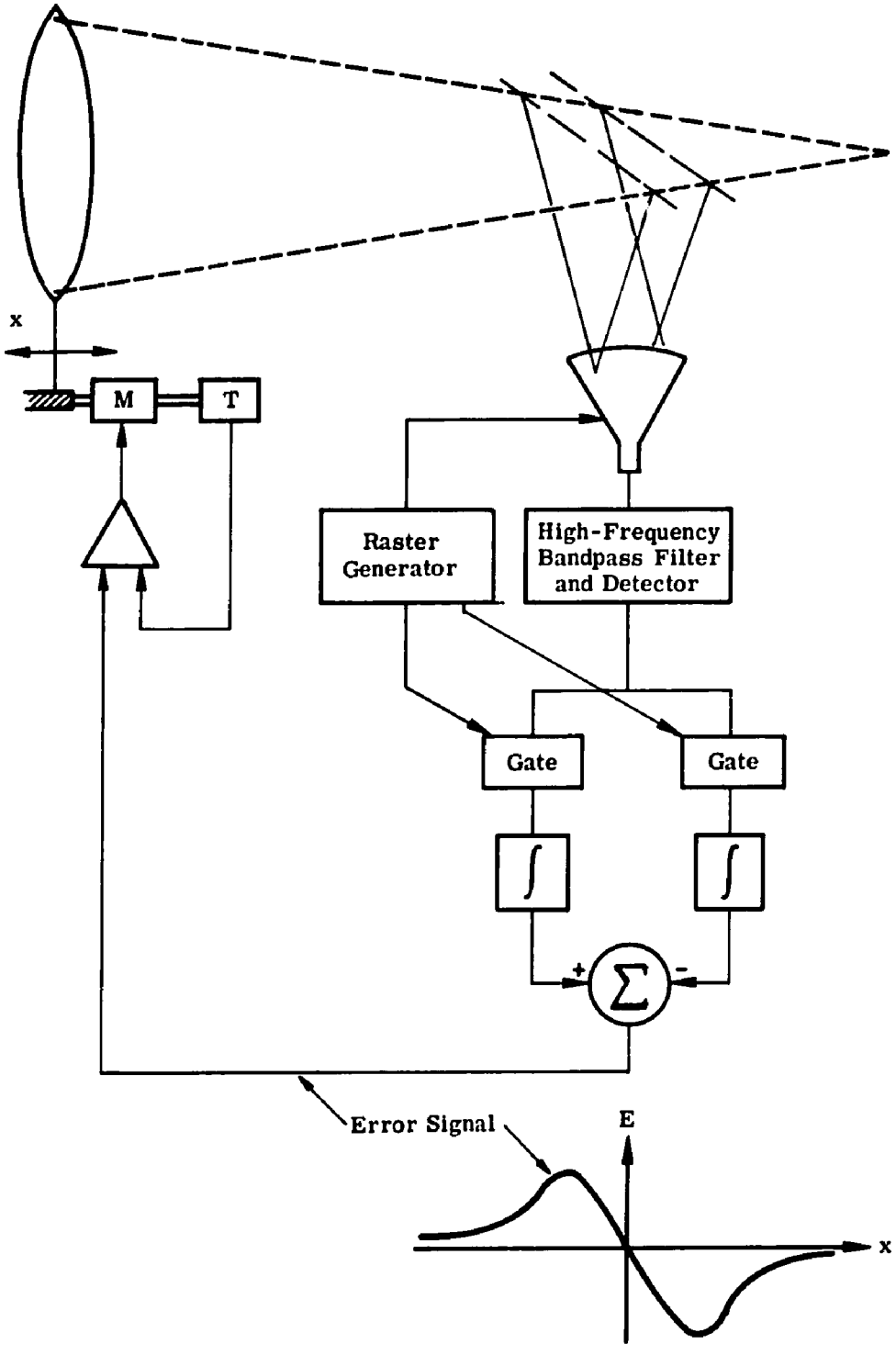


FIGURE 7. NONCOHERENT AUTOFOCUS BLOCK DIAGRAM

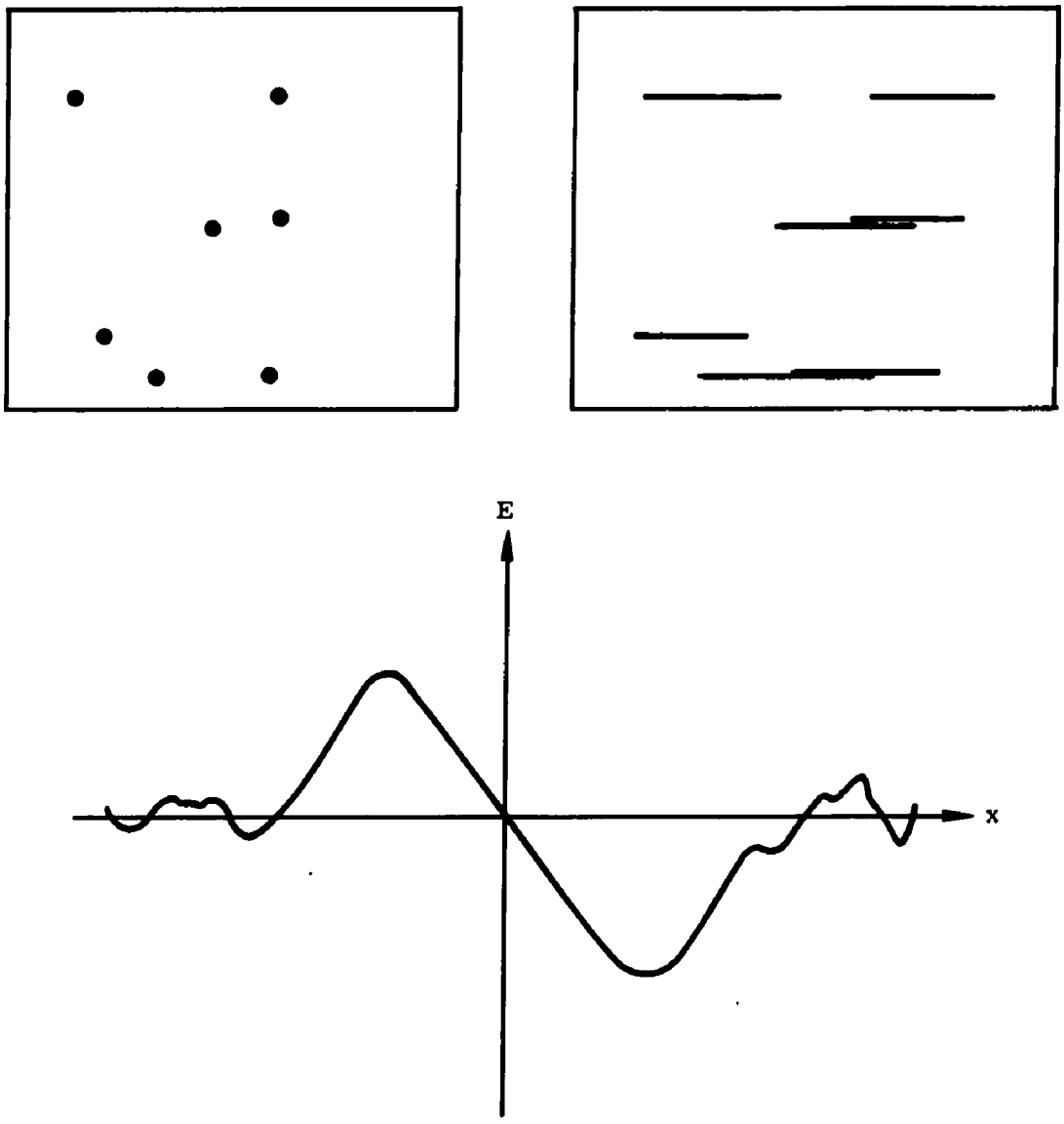


FIGURE 8. POINT-IMAGE FIELD AND FOCUS ESTIMATOR

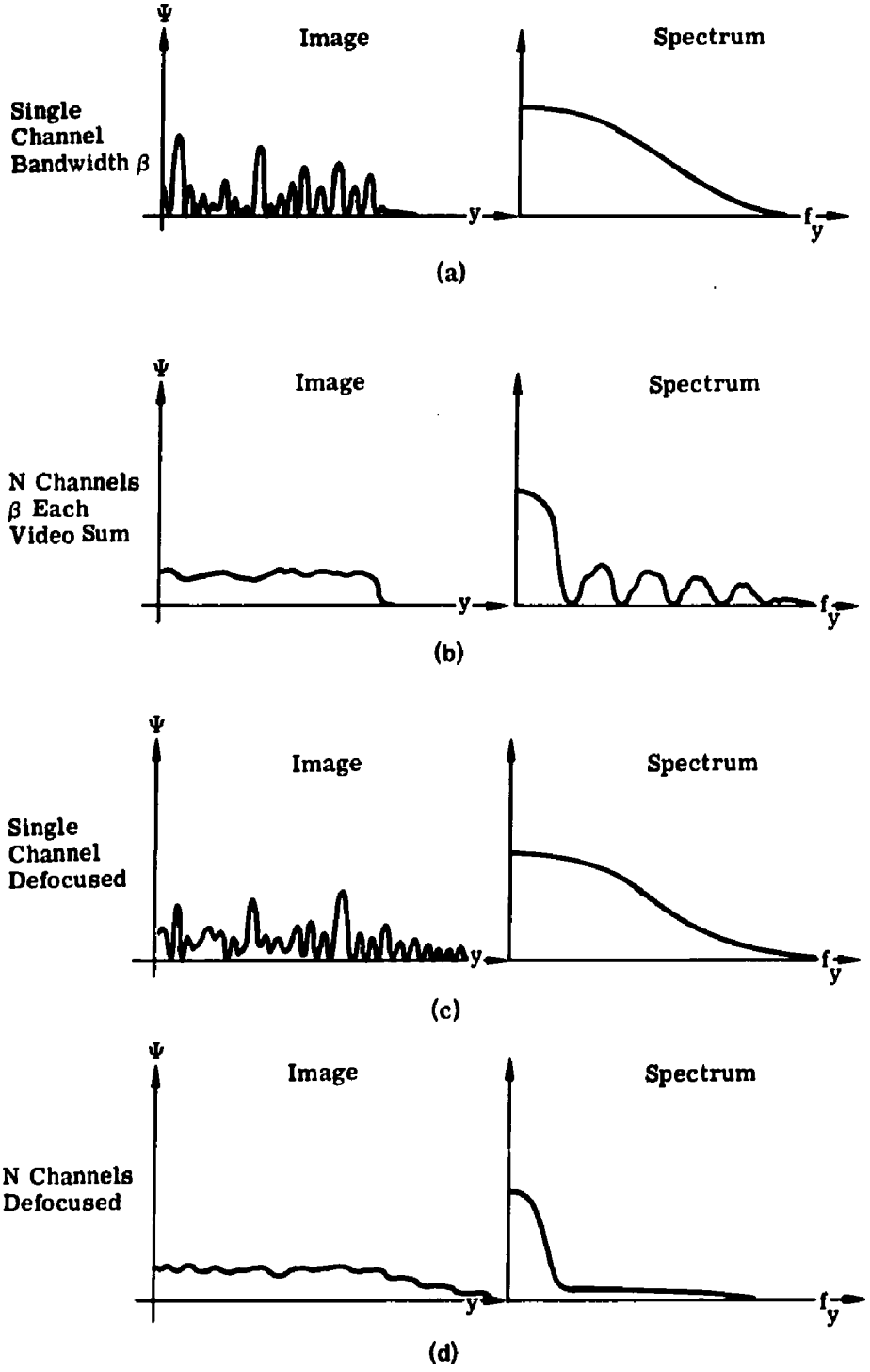


FIGURE 9. COHERENT IMAGE OF DISCONTINUOUS OBJECT WITH INTEGRATION

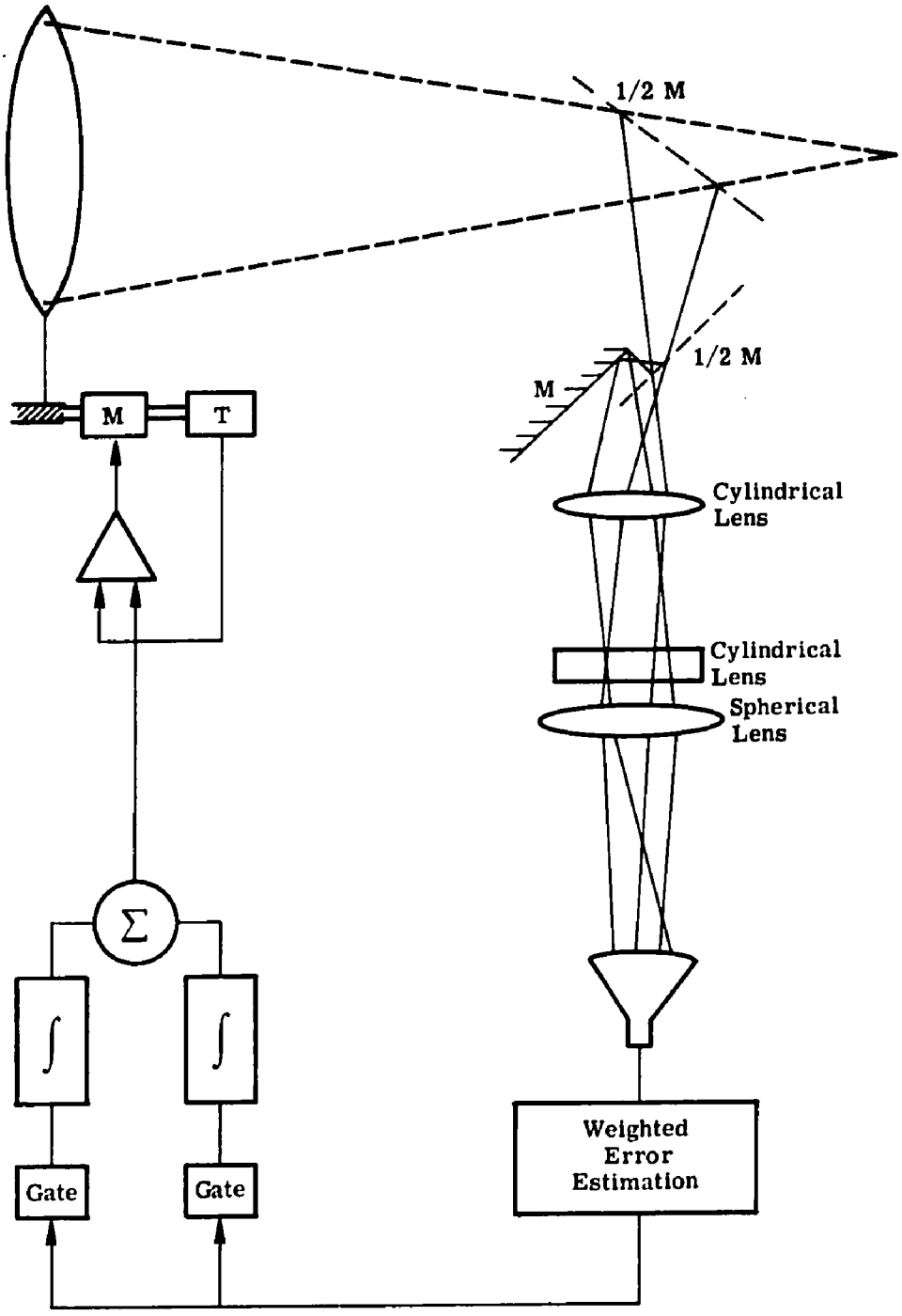


FIGURE 10. COHERENT AUTOFOCUS BLOCK DIAGRAM

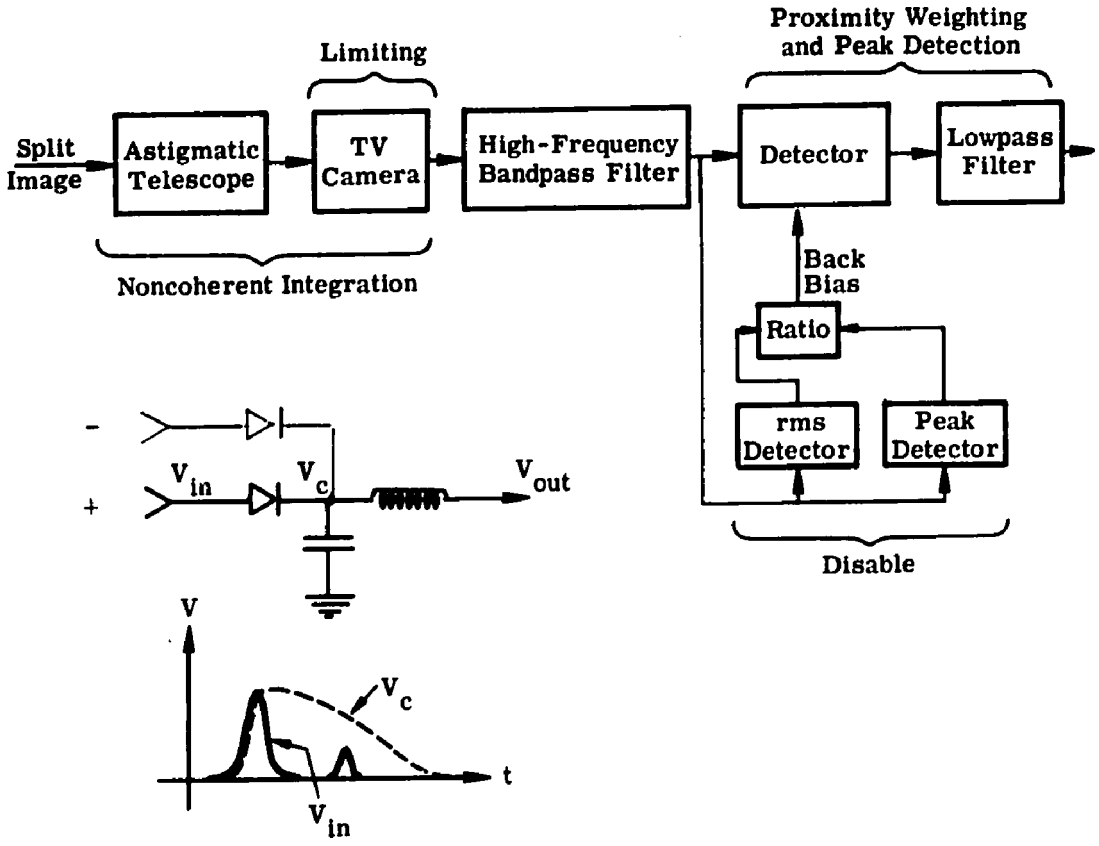


FIGURE 11. ERROR ESTIMATOR BLOCK DIAGRAM

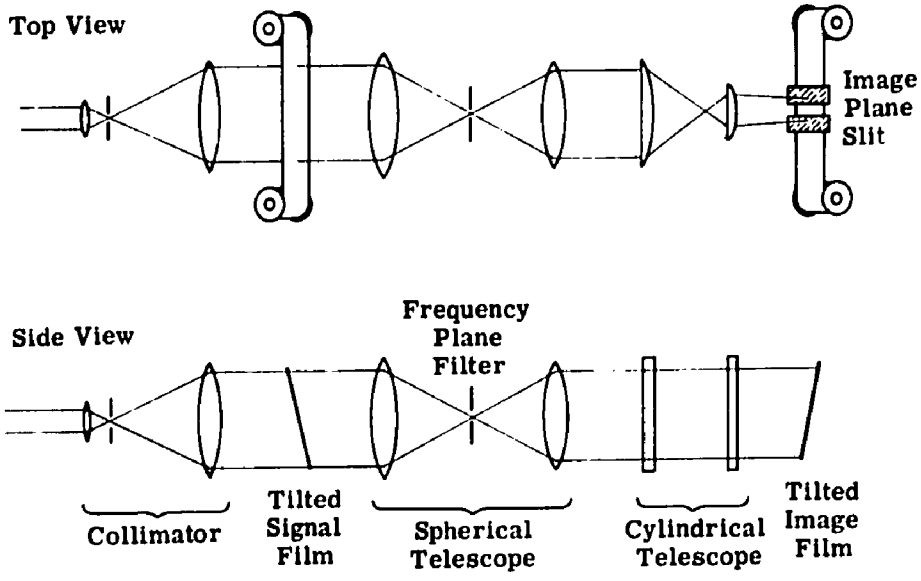


FIGURE 12. TILTED PLANE PROCESSOR

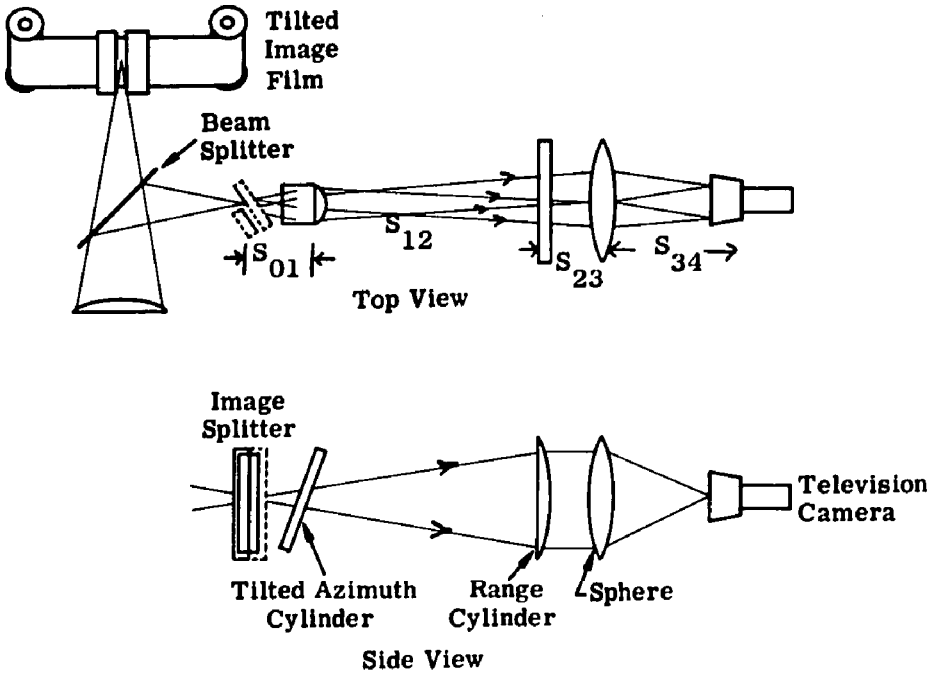


FIGURE 13. AUTOFOCUS OPTICAL SYSTEM

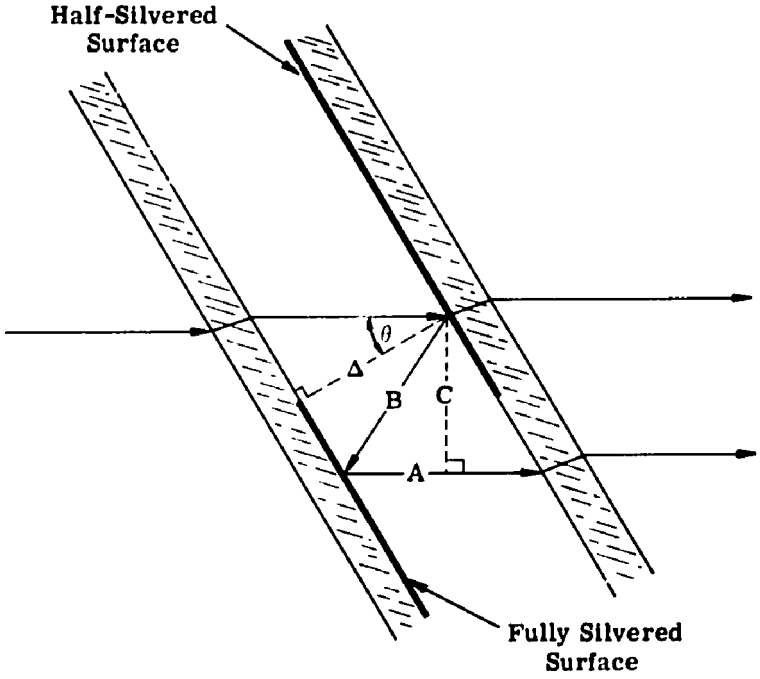


FIGURE 14. IMAGE SPLITTER

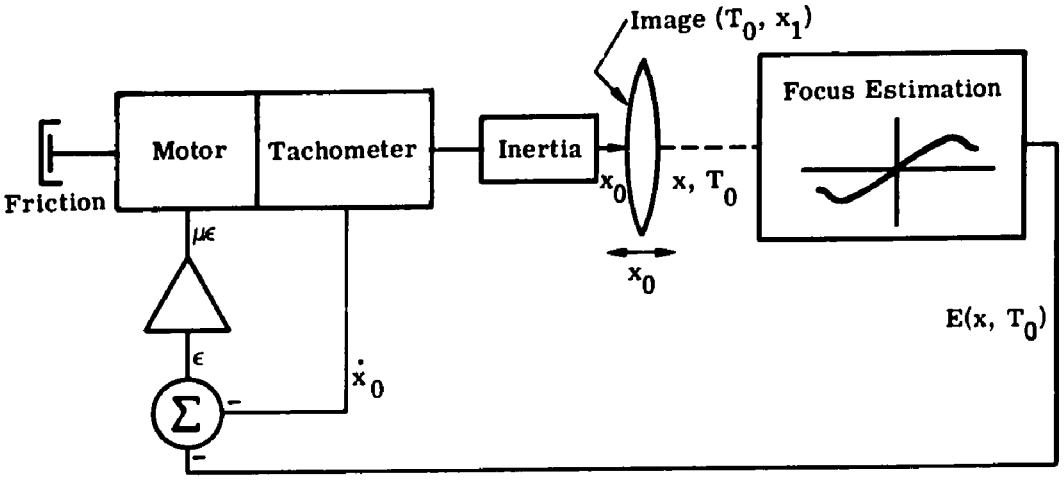


FIGURE 15. SERVO SYSTEM BLOCK DIAGRAM

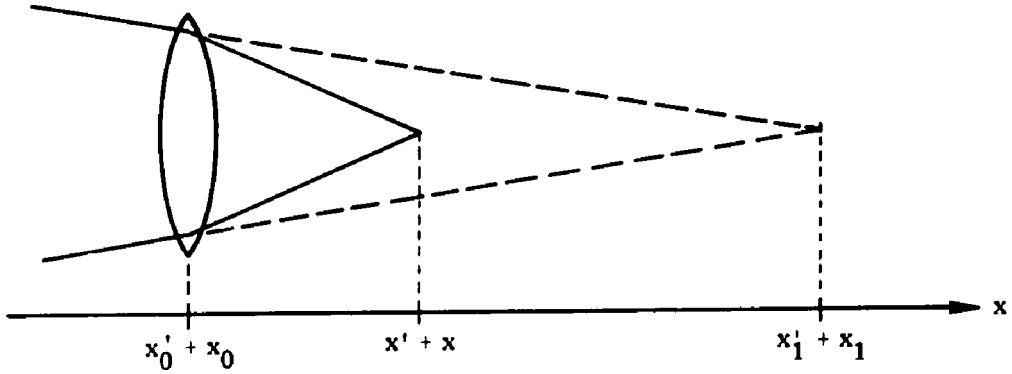
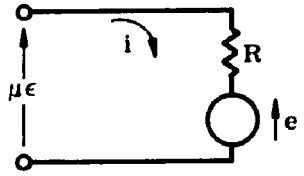
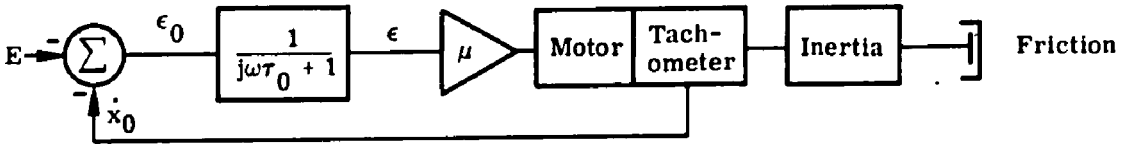


FIGURE 16. FOCUS COORDINATE SYSTEM



(a) Motor



(b) Tachometer Loop

FIGURE 17. SERVO SYSTEM TACHOMETER LOOP

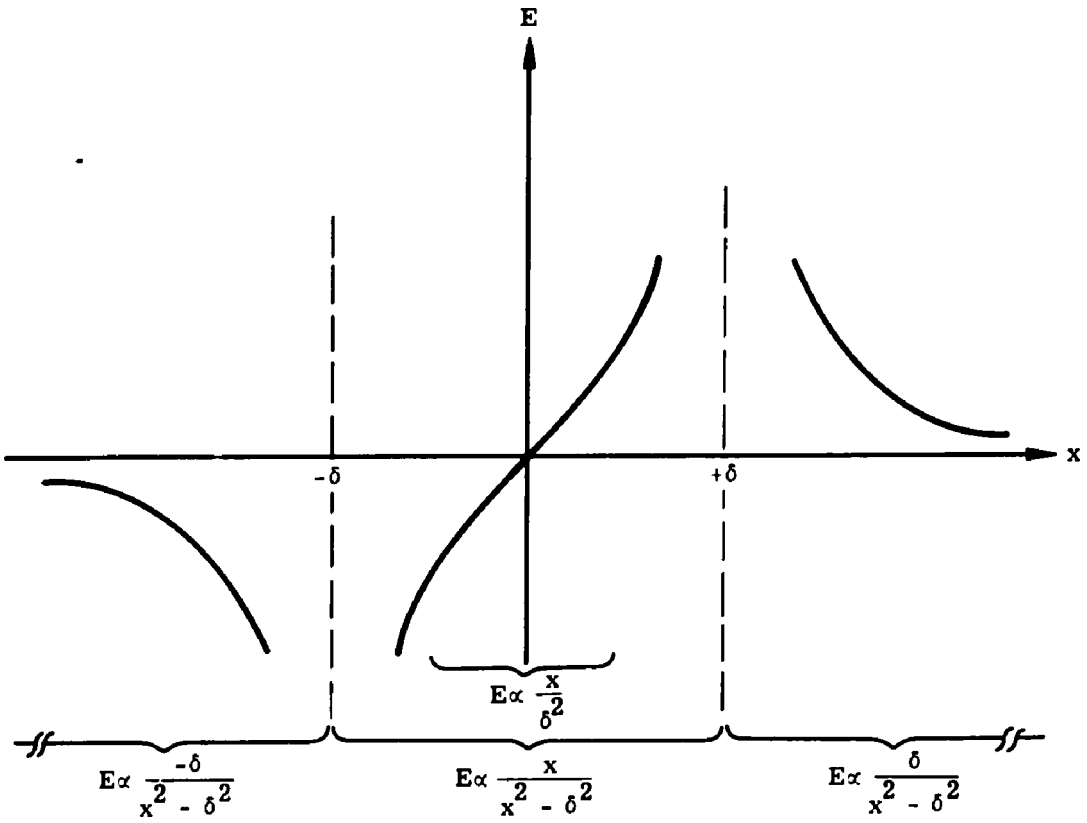


FIGURE 18. ESTIMATOR TRANSFER FUNCTION

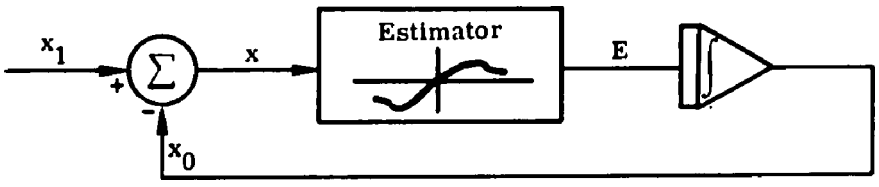


FIGURE 19. SIMPLIFIED AUTOFOCUS LOOP

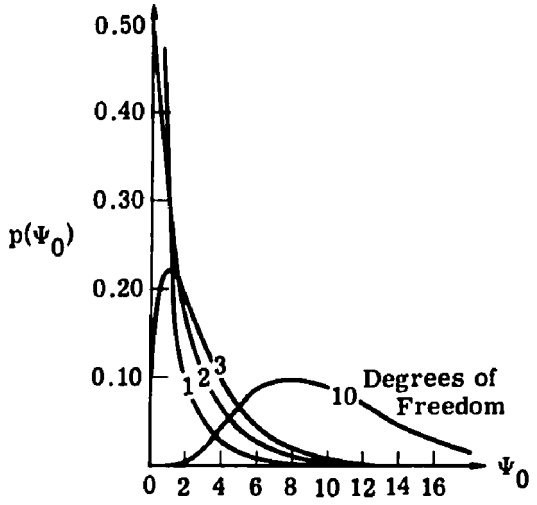


FIGURE 20. CHI-SQUARE DENSITY FUNCTIONS

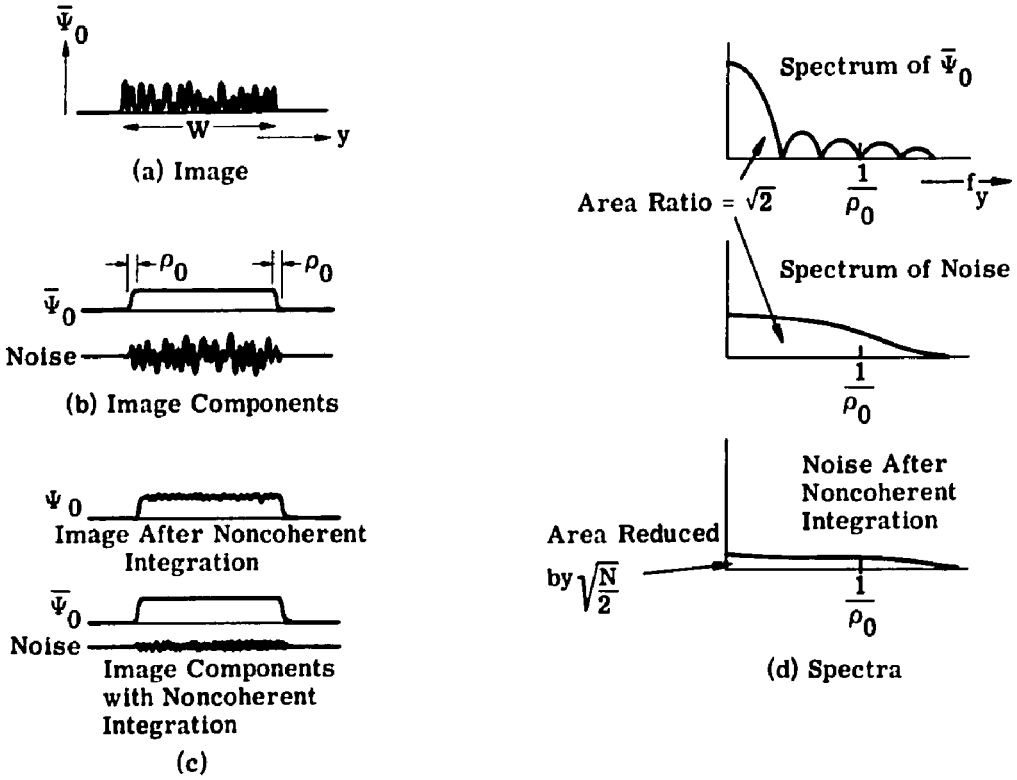


FIGURE 21. FINITE DISTRIBUTED IMAGE

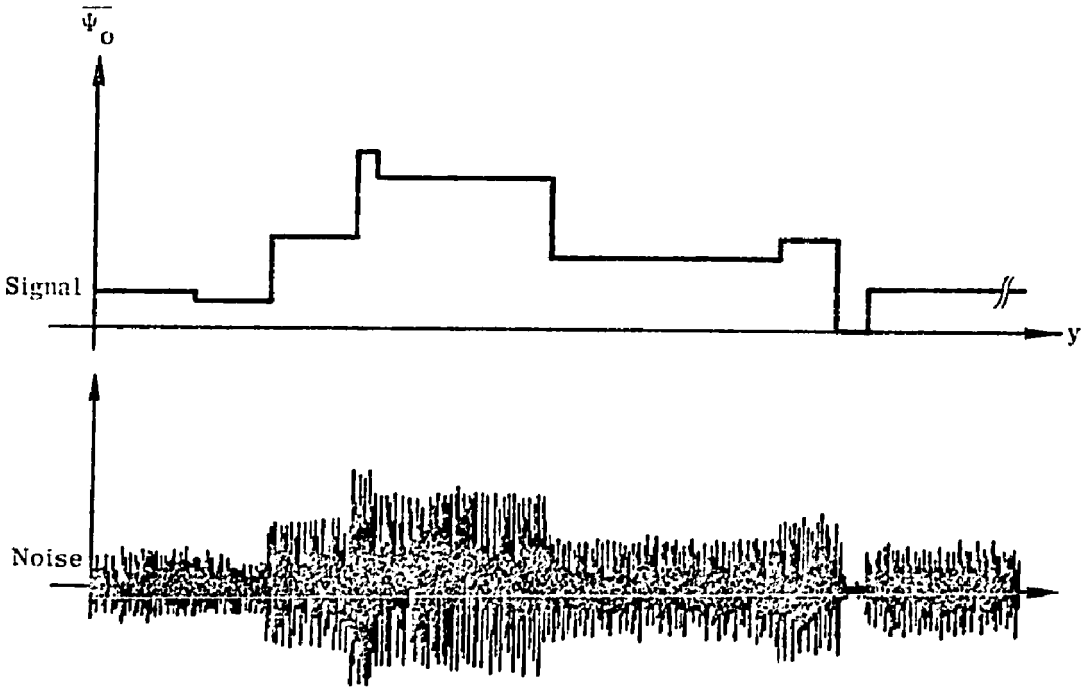


FIGURE 22. FARMLAND IMAGE

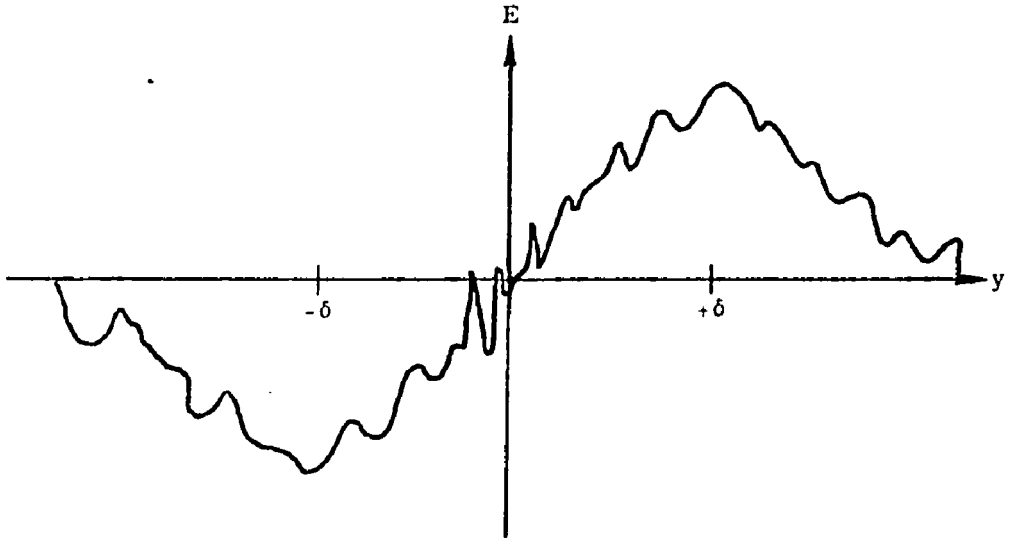


FIGURE 23. FARMLAND ERROR FUNCTION

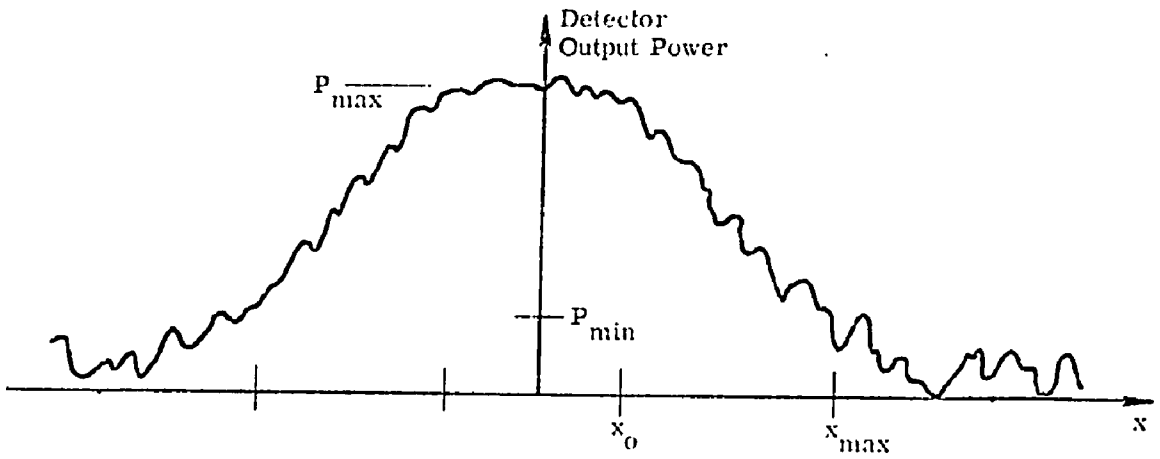


FIGURE 24. PEAK DETECTOR OUTPUT --VERY WEAK POINT IMAGE

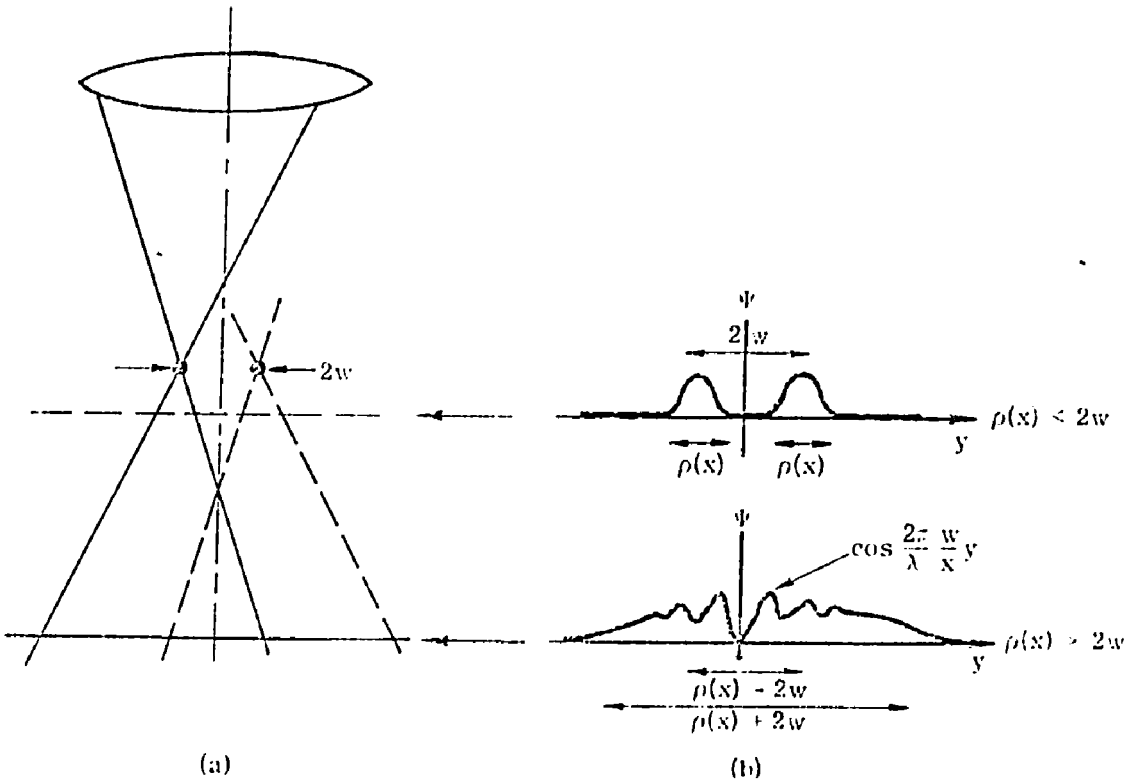


FIGURE 25. POINT PAIR

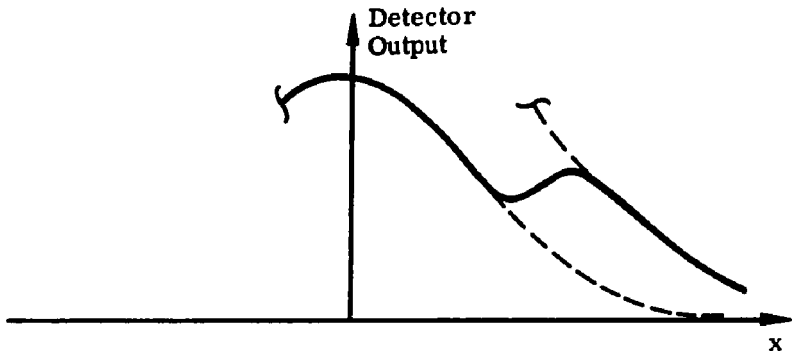


FIGURE 26. DIFFERENTIATOR/PEAK DETECTOR OUTPUT — PAIR

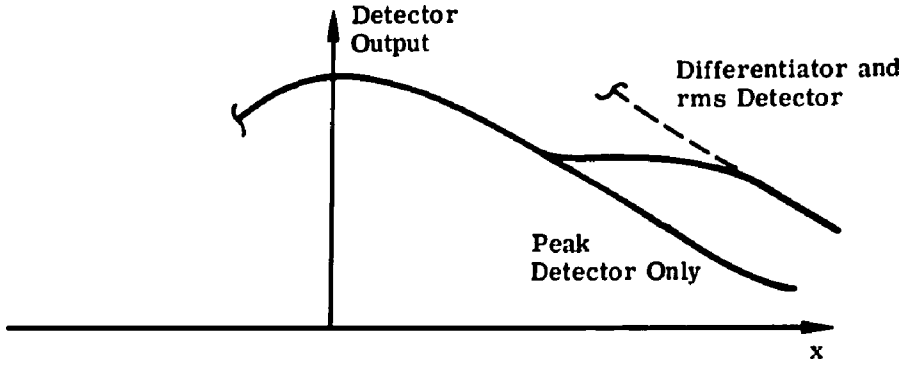


FIGURE 27. DIFFERENTIATOR/rms DETECTOR OUTPUT — PAIR

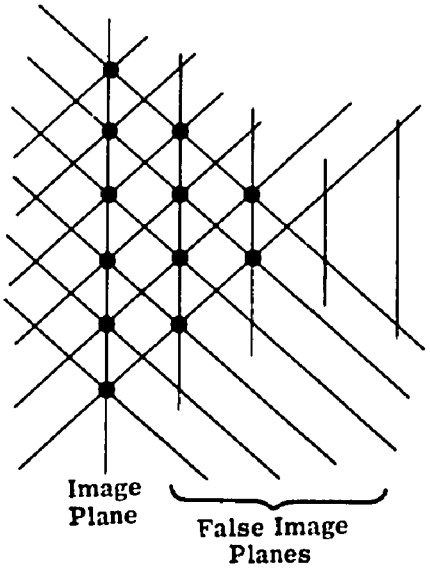


FIGURE 28. INFINITE ARRAY OF POINTS

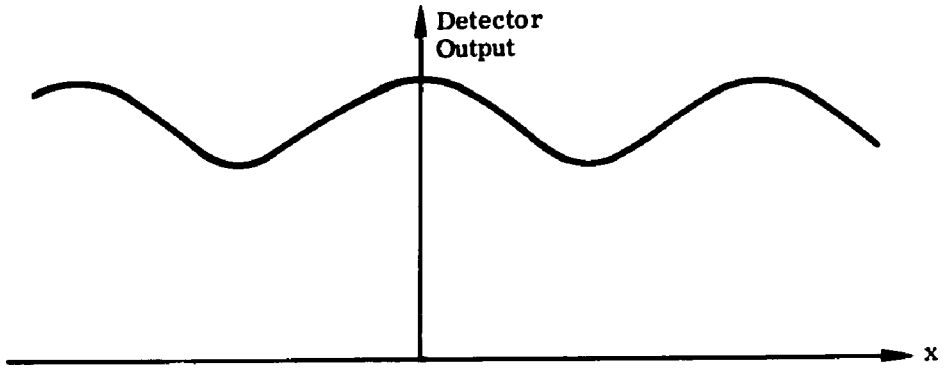


FIGURE 29. DETECTOR OUTPUT; INFINITE ARRAY

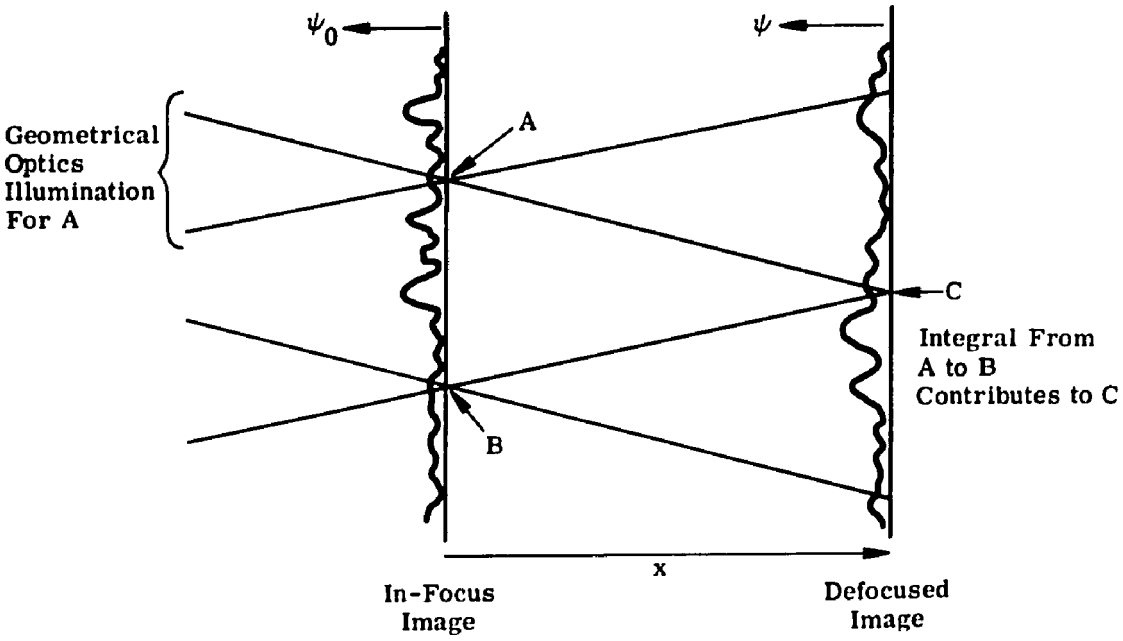


FIGURE 30. NONGAUSSIAN DISTRIBUTED IMAGE

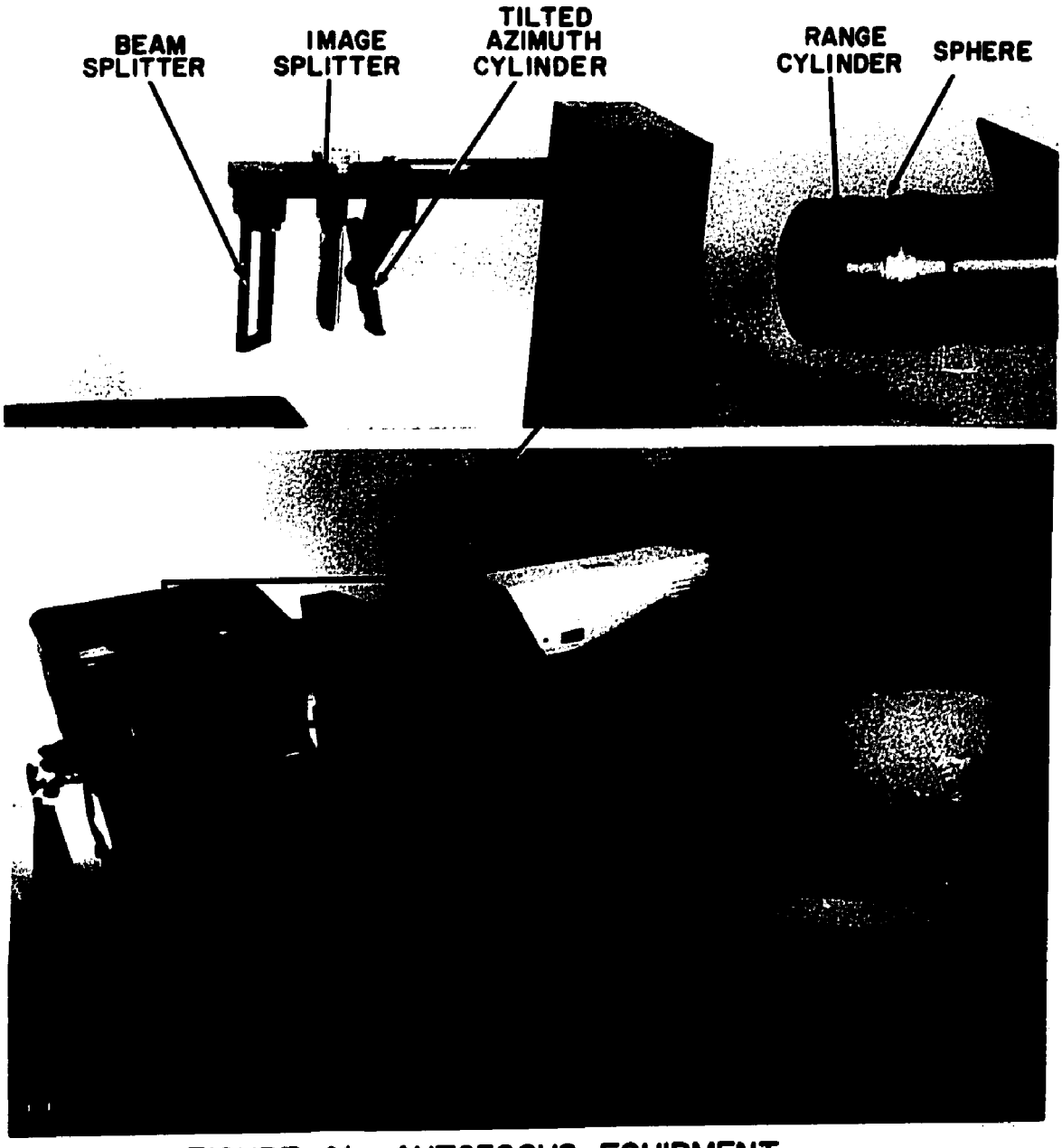


FIGURE 31 AUTOFOCUS EQUIPMENT

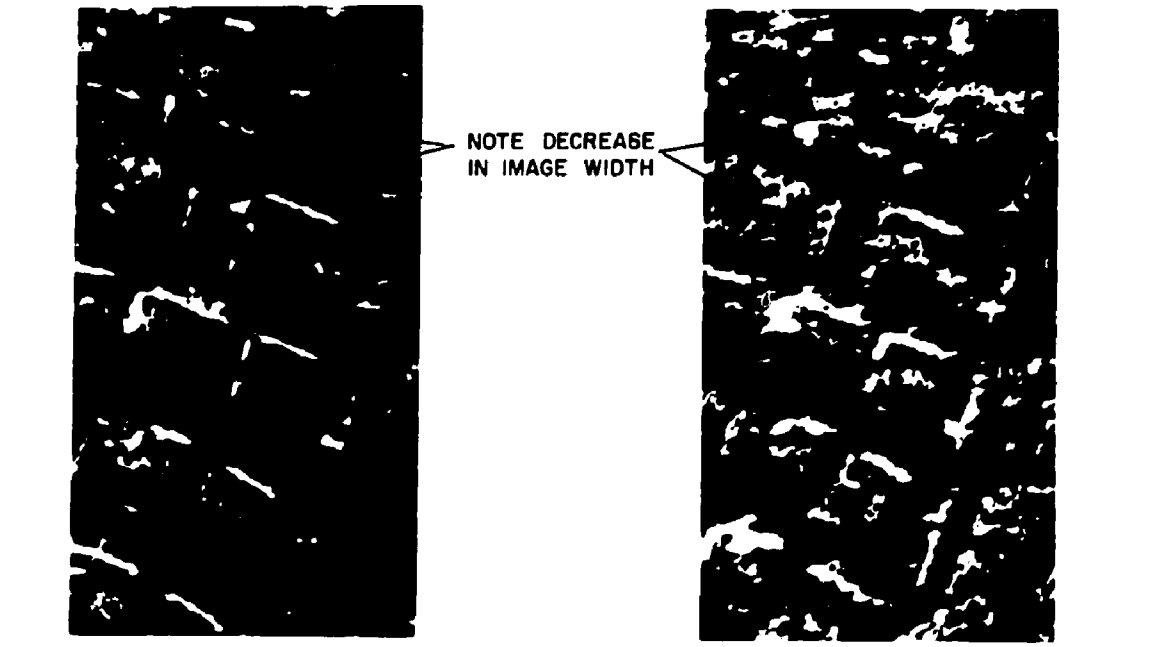


FIGURE 32 EXPERIMENTAL RESULTS

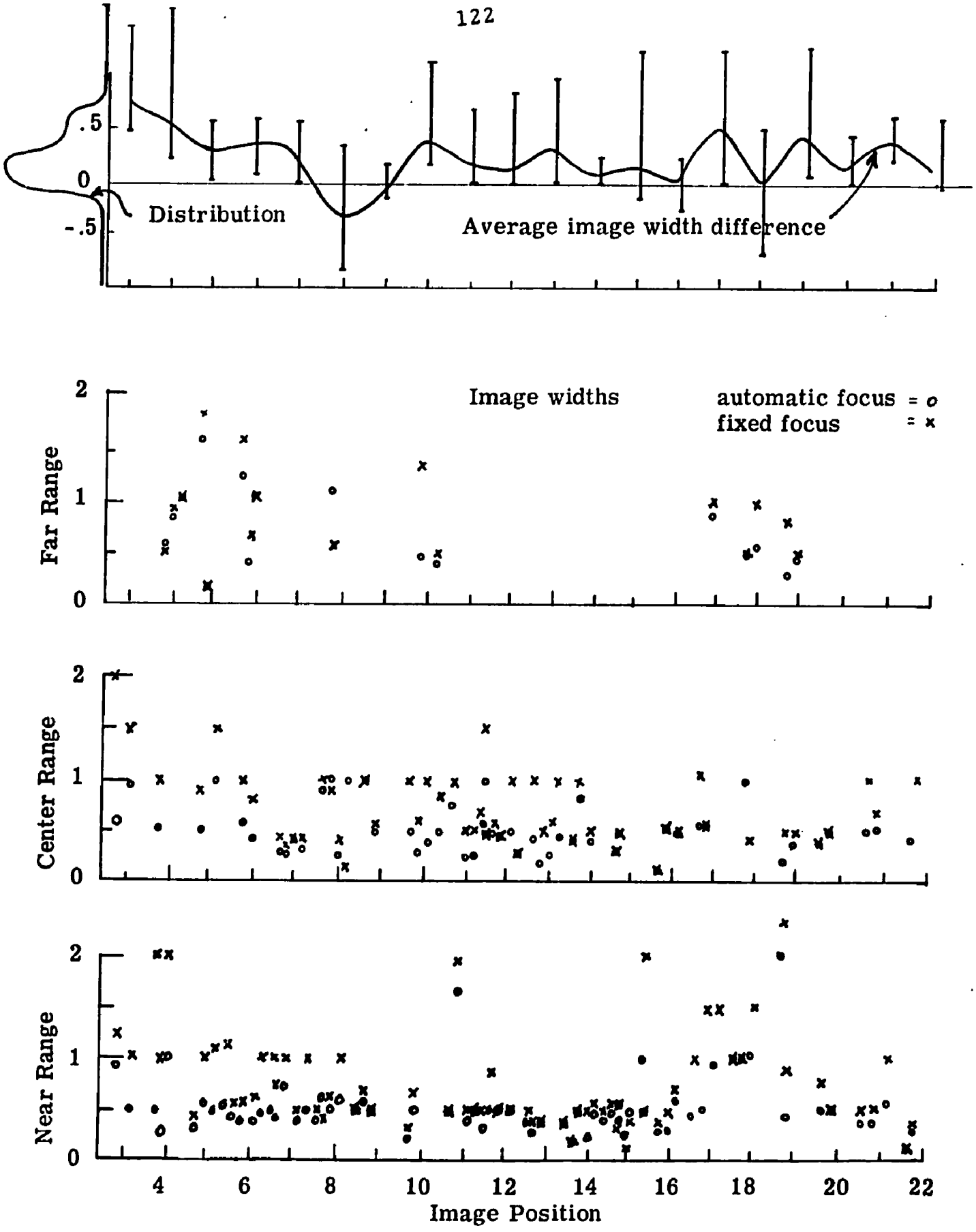


FIGURE 33. RADAR IMAGE WIDTH MEASUREMENTS

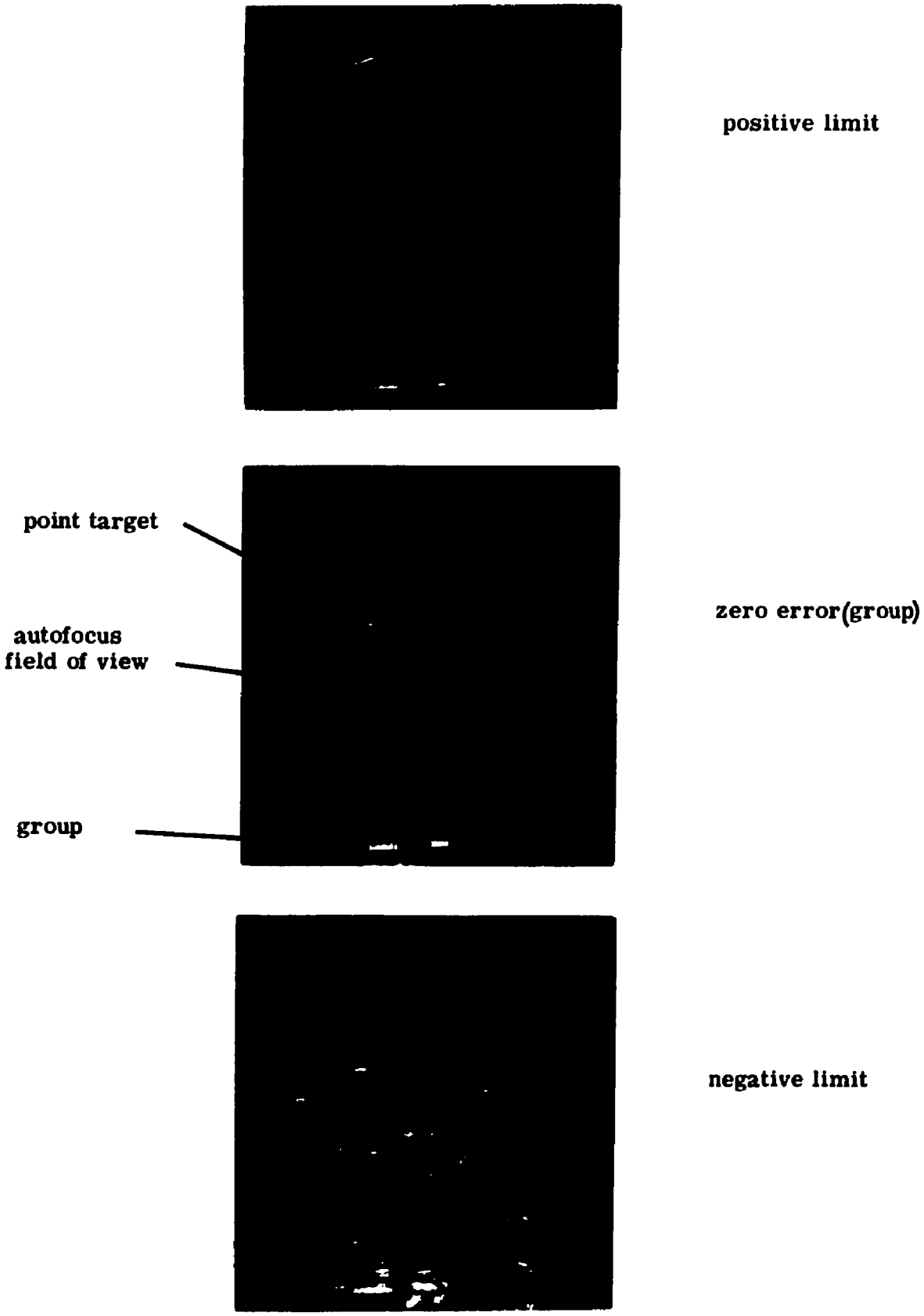
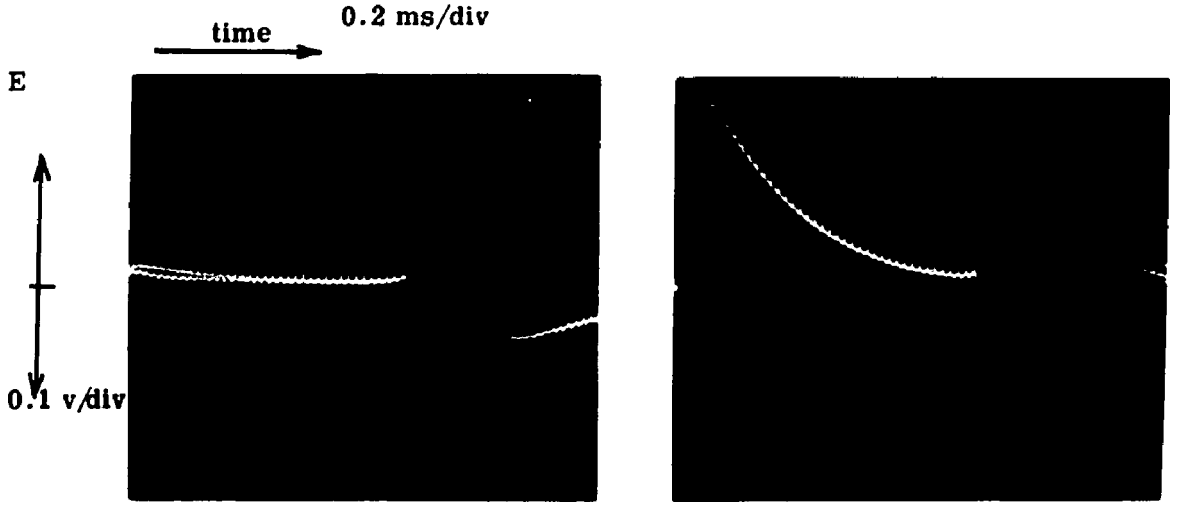
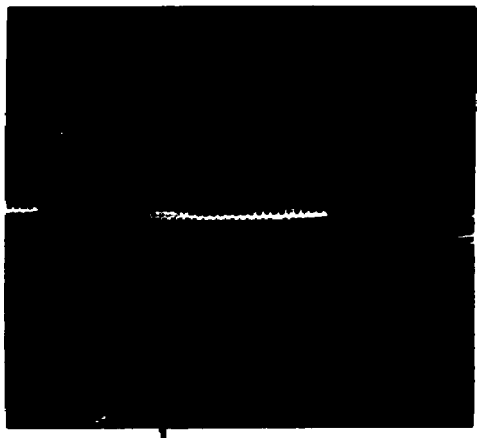


FIGURE 34. POINT TARGET AND COMPLEX GROUP IMAGES

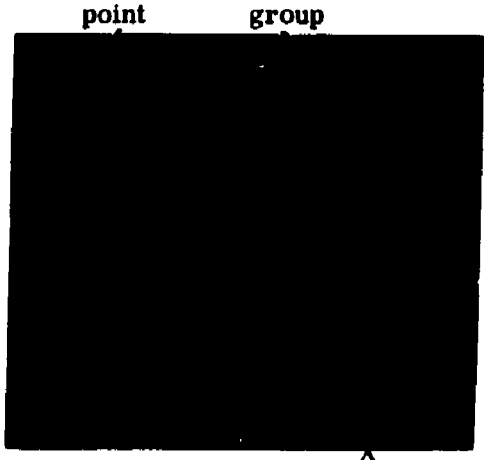


a) positive limit focus $+\frac{3}{8}$ in.

b) focus $+\frac{1}{4}$ in.



c) focus $+\frac{1}{8}$ in.



d) zero error group focus $\triangleq 0$



e) focus $-\frac{1}{8}$ in.



f) negative limit focus $-\frac{1}{4}$ in.

FIGURE 35. POINT TARGET AND COMPLEX GROUP ESTIMATOR OUTPUT

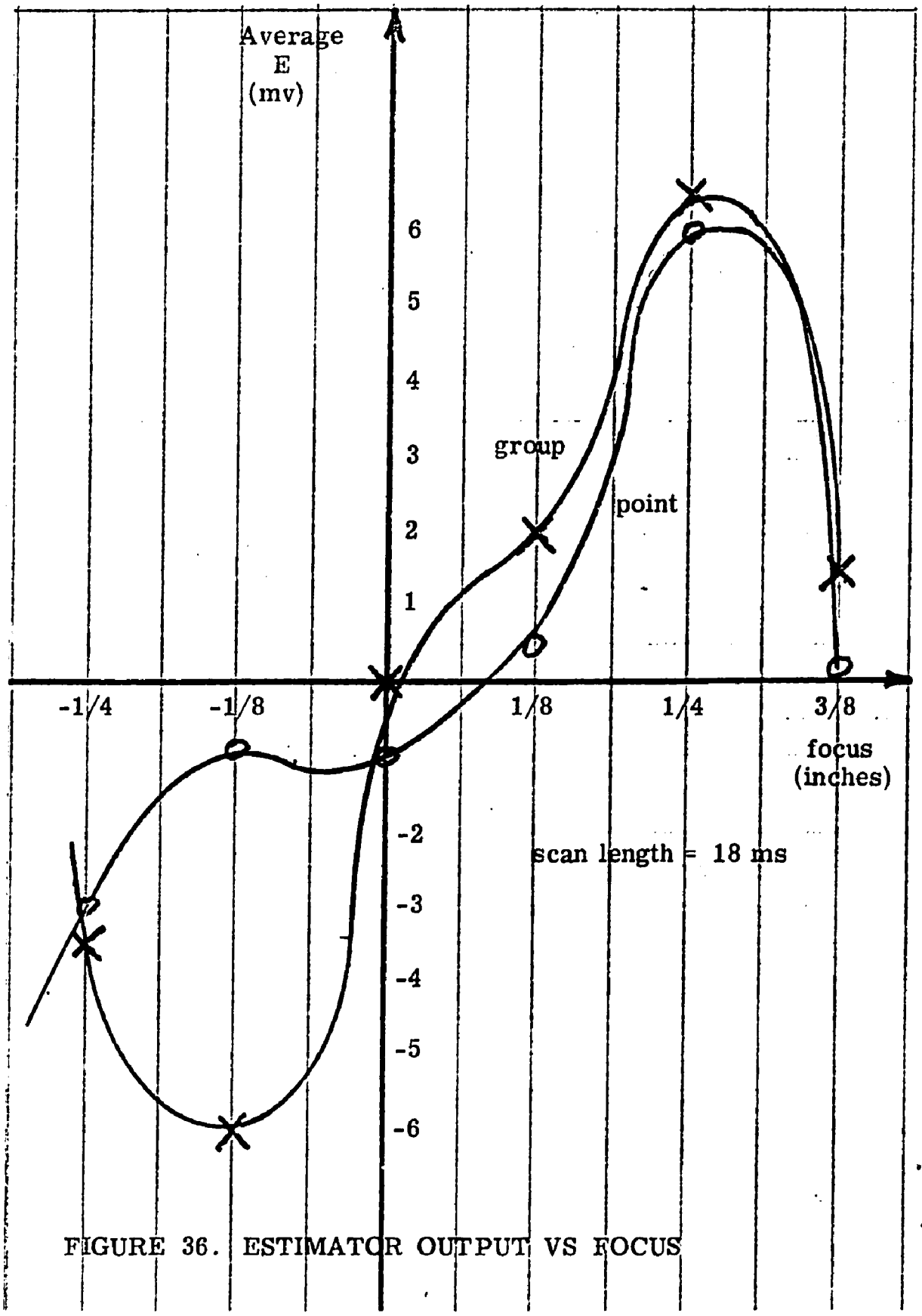


FIGURE 36. ESTIMATOR OUTPUT VS FOCUS

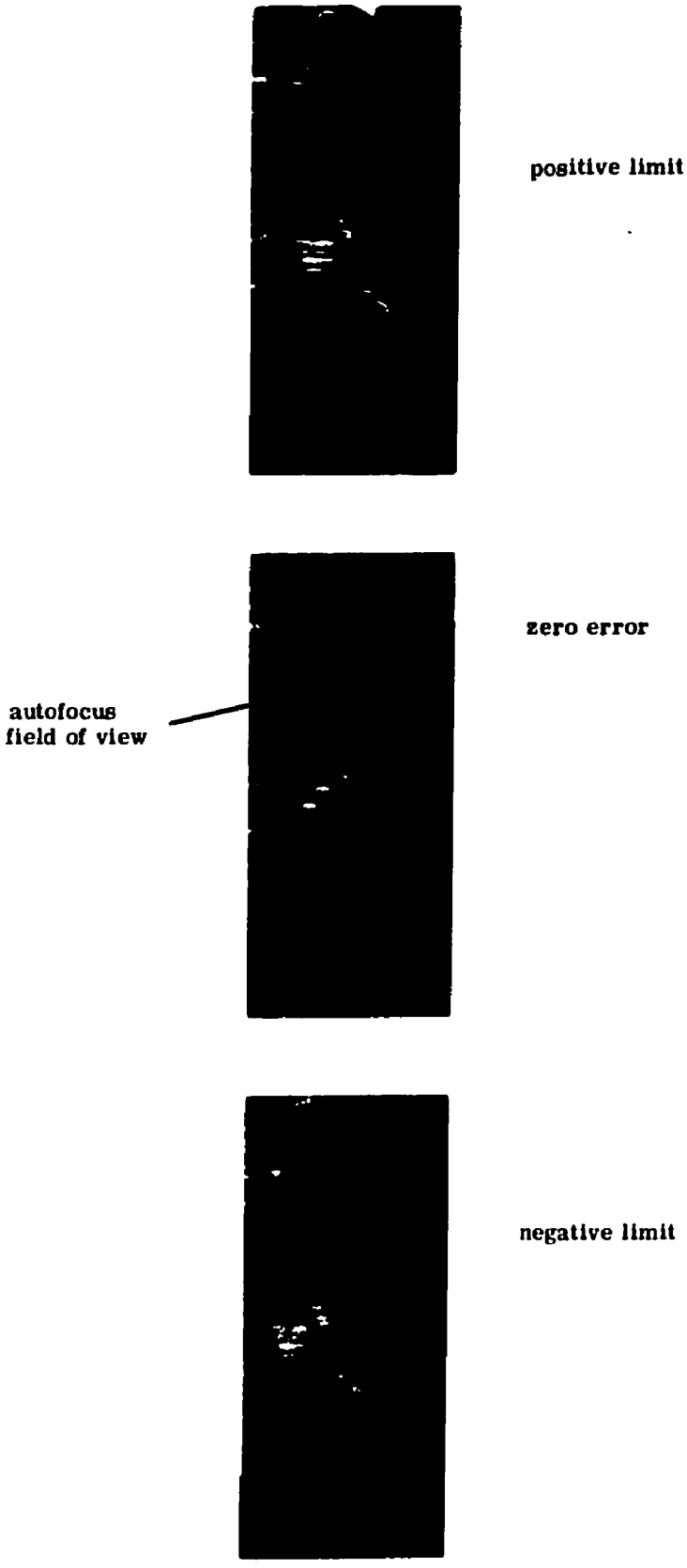


FIGURE 37. LAND WATER BOUNDARY IMAGES

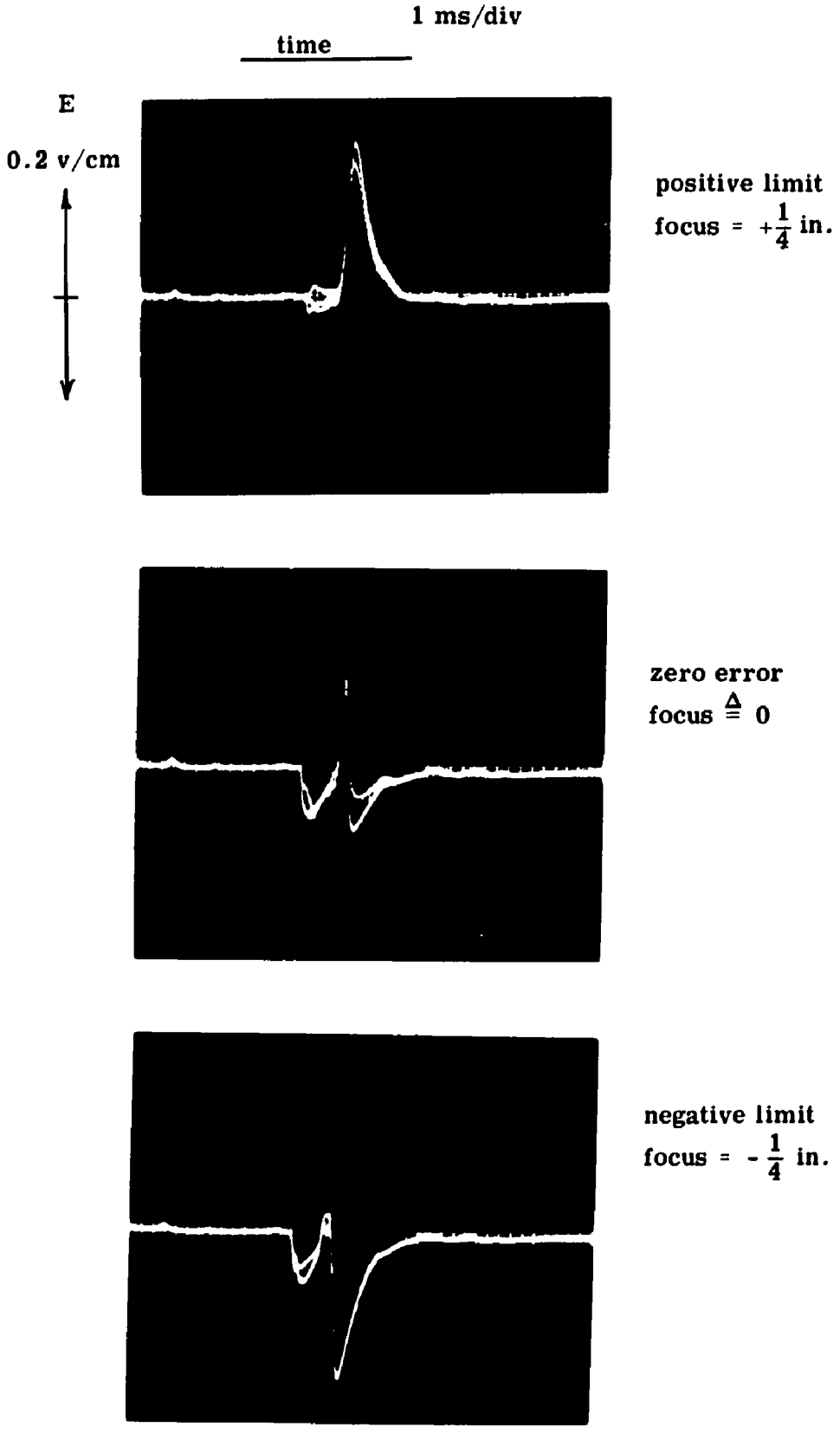
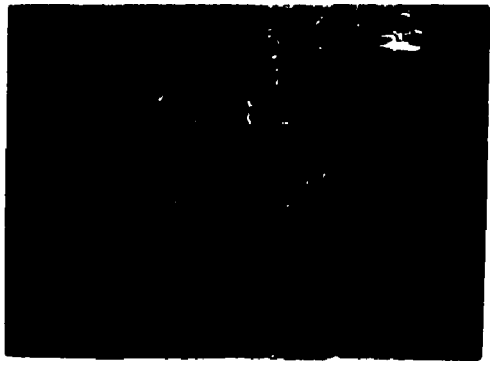
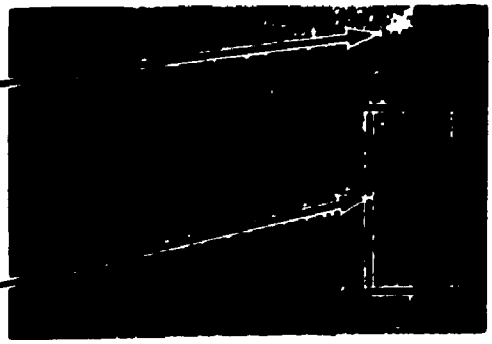


FIGURE 38. LAND WATER BOUNDARY ESTIMATOR OUTPUT



positive limit
focus = $+\frac{1}{4}$ in.

point target



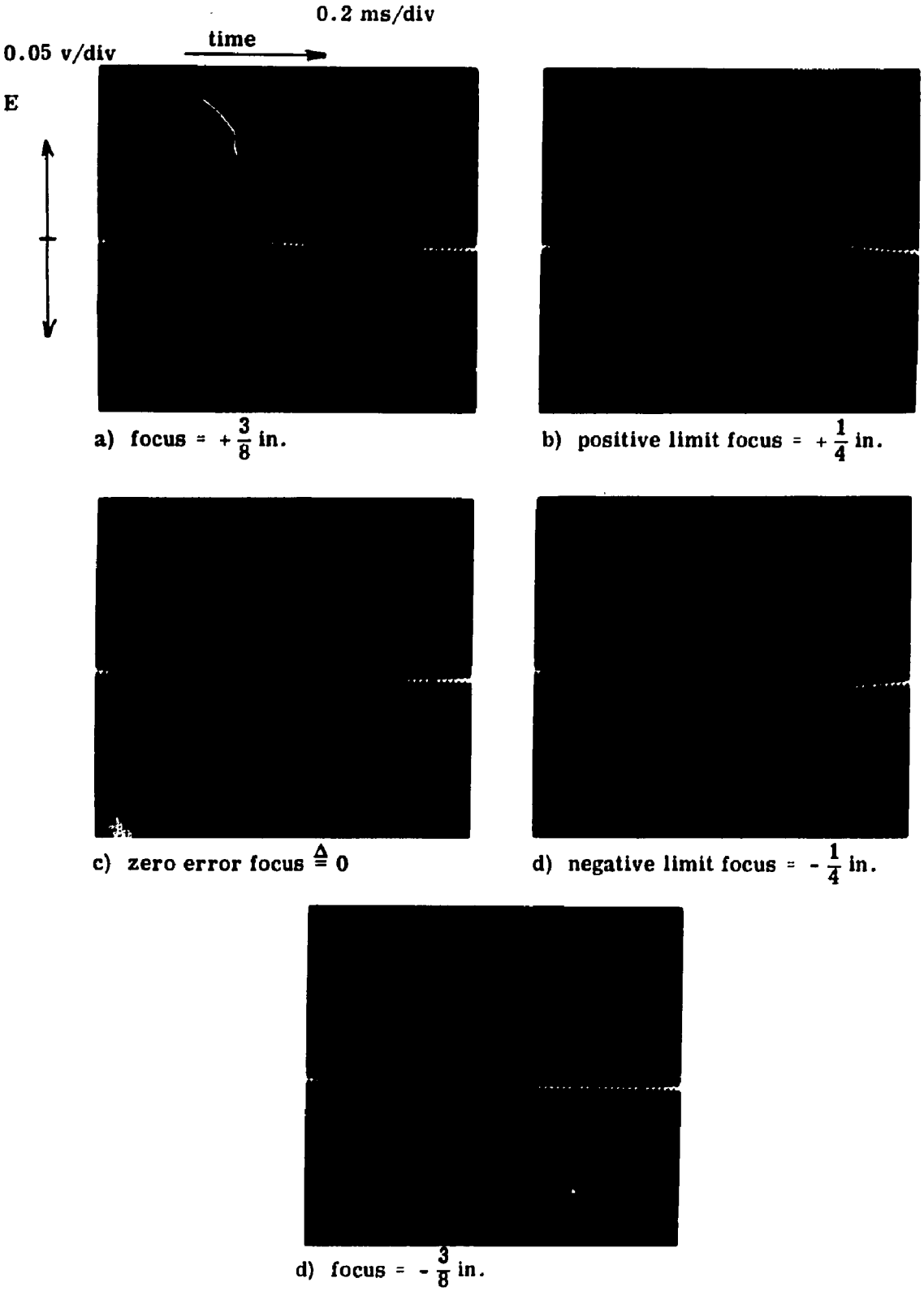
autofocus
field of view

zero error
focus $\triangleq$ 0



negative limit
focus = $-\frac{1}{4}$ in.

FIGURE 39. ARTIFICIAL LAND WATER BOUNDARY IMAGES



a) focus = $+\frac{3}{8}$ in.

b) positive limit focus = $+\frac{1}{4}$ in.

c) zero error focus $\triangleq$ 0

d) negative limit focus = $-\frac{1}{4}$ in.

d) focus = $-\frac{3}{8}$ in.

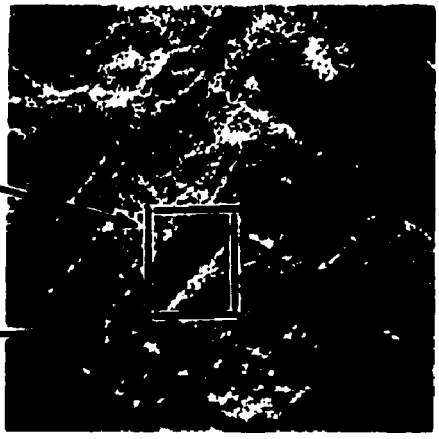
FIGURE 40. ARTIFICIAL LAND WATER BOUNDARY ESTIMATOR OUTPUT



positive limit
focus = $+\frac{1}{4}$ in.

autofocus
field of view

farm



zero error
focus $\triangleq$ 0

FIGURE 41. FARMLAND BOUNDARY IMAGE

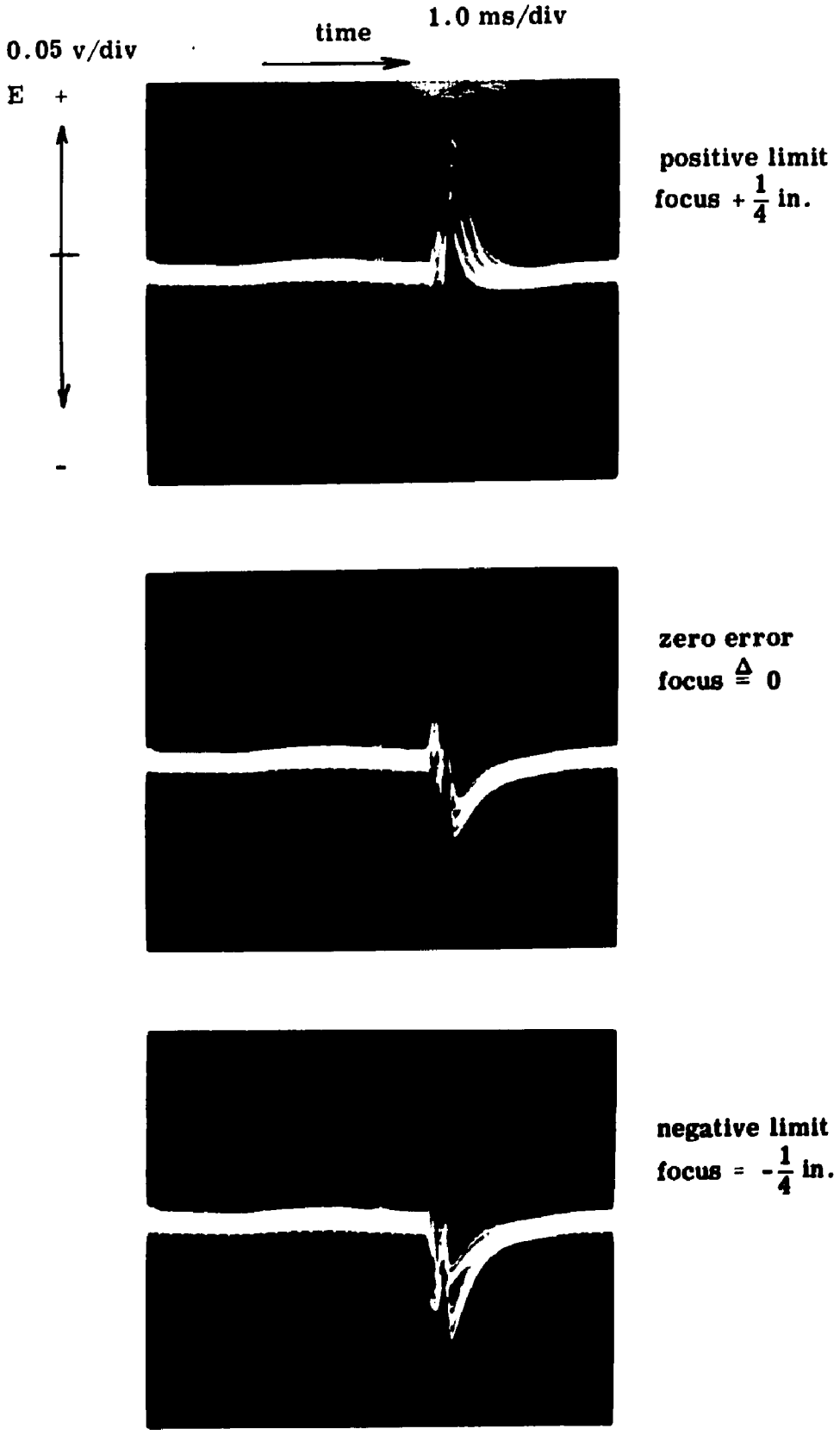


FIGURE 42. FARMLAND BOUNDARY ESTIMATOR OUTPUT

REFERENCES

1. Beckers, "A Photoelectric Focus and Seeing Monitor for Solar Telescopes," Applied Optics, Vol. 5, No. 2, February 1966, p. 301.

2. Cutrona, et al, "A High-Resolution-Radar Combat Surveillance System," IRE Trans. on Military Electronics, Vol. MIL-5, April 1961, pp. 127—131. See also several articles in Vol. MIL-6, April 1962.

3. Porter and Bilal, Optimum Characteristics of Some Motion-Compensation Systems (U), Report No. 2900-371-T(1), Willow Run Laboratories of the Institute of Science and Technology, The University of Michigan, Ann Arbor, March 1963.

4. Zelenka, Optimization of a Frequency Tracker, Report No. 7000-20-T, Willow Run Laboratories of the Institute of Science and Technology, The University of Michigan, Ann Arbor, May 1967.

5. Harger, Statistically Optimum Optical Data Processing with Automatic Focus Estimation, Report No. 7000-50-T, Willow Run Laboratories of the Institute of Science and Technology, The University of Michigan, Ann Arbor, November 1966.

6. Cutrona, Leith, Porcello and Vivian, "On the Application of Coherent Optical Processing Techniques to Synthetic-Aperture Radar," Proc. of the IEEE, Vol. 54, No. 8, August 1966, p. 1026.

7. Kozma, Leith and Massey, "The Tilted Plane Optical Processor," Applied Optics, Vol. 11, 1972.

8. Born and Wolf, Principles of Optics, 1964, Macmillan, New York, pp. 443 and 444 gives a general discussion. For a derivation of the expression used see: Zelenka, The Point Image Revisited, Memorandum to File, Willow Run Laboratories of the Institute of Science and Technology, The University of Michigan, Ann Arbor, November 19, 1971, p. 8.

9. Davenport and Root, An Introduction to the Theory of Random Signals and Noise, McGraw-Hill, New York, 1958, p. 34.

10. Davenport and Root, An Introduction to the Theory of Random Signals and Noise, McGraw-Hill, New York, 1958, p. 253.

11. Porcello, Massey, Innes and Marks, Diversity and Mixed-Integration Processing in Synthetic-Aperture Radar (U), (Secret Paper), Fourteenth Annual Tri-Service Radar Symposium, Willow Run Laboratories of the Institute of Science and Technology, The University of Michigan, Ann Arbor, 1968, AD 394 090 (SECRET).

12. Lewis, Mixed Integration Processing of Synthetic Aperture Radar Data, Report No. AFAL-TR-72-215, Willow Run Laboratories of the Institute of Science and Technology, The University of Michigan, Ann Arbor, August 1972.

13. Johansen, et al, Rotating Target Imagery (U), Report No. 37000-51-T, Willow Run Laboratories of the Institute of Science and Technology, The University of Michigan, Ann Arbor, 1972 (CONFIDENTIAL).

14. Hogg and Craig, Introduction to Mathematical Statistics, Macmillan, 1965, pp. 139-141.

15. Montgomery, Self-Imaging Objects of Infinite Aperture, Journal of the Optical Society of America, Vol. 57, No. 6, June 1967, p. 772.

16. Goodman, Introduction to Fourier Optics, McGraw-Hill, New York, 1968, p. 45.

17. "An Experimental Investigation of the Amplitude Distribution of Radar Terrain Return," 6th Conf. Sweden National Comm. Sci. Radio, Research Institute of National Defense, Stockholm, March 13, 1963.

BIBLIOGRAPHY

1. Fisher, Compensation of Aircraft Acceleration for Airborne Synthetic Array Radars (U), (Confidential Paper), Tenth Annual Radar Symposium, Willow Run Laboratories of the Institute of Science and Technology, The University of Michigan, Ann Arbor, 1964, AD 324 712 (SECRET). Listed as a supplement to Ref. [3] .

2. DeMarais and Jacobson, A Prototype Automatic-Focusing System for a Coherent Optical Radar Data Processor (U), (Secret Paper), Thirteenth Annual Tri-Service Radar Symposium, Willow Run Laboratories of the Institute of Science and Technology, The University of Michigan, Ann Arbor, 1967, AD 384 825L (SECRET). Listed as a supplement to Ref. [5] .

3. Hildebrand, An Automatic Focusing System for Optical Correlators (U), (Confidential Paper), Tenth Annual Radar Symposium, Willow Run Laboratories of the Institute of Science and Technology, The University of Michigan, Ann Arbor, 1967, AD 352 159 (SECRET). Listed as a supplement to Ref. [5] .